Hierarchically Porous Carbon Supports Enable Efficient Syngas Production in Electrified Reactive Capture

Hengzhou Liu[1†], Heejong Shin[1†], Xiao-Yan Li[1†], Guangcan Su[1,2†], Pengfei Ou[1], Yong Wang[1], Lihaokun Chen[3], Jiaqi Yu[1], Yuanjun Chen[1], Rong Xia[1], Geonhui Lee[4], Kug-Seung Lee[5], Christine Yu[1], Peiying Wang[1], Deokjae Choi[1], Daojin Zhou[1], Cong Tian[1], Issam Gereige[6], Ammar Alahmed[6], Aqil Jamal[6], Omar K. Farha[1], Shannon W. Boettcher[3,7], Jennifer B. Dunn[2], Ke Xie[1,*], Edward H. Sargent[1,8,*]

[1]Department of Chemistry, Northwestern University, 2145 Sheridan Road, Evanston, IL 60208, United States

[2]Department of Chemical and Biological Engineering, Northwestern University, 2145 Sheridan Road, Evanston, IL 60208, United States

[3]Department of Chemistry and the Oregon Center for Electrochemistry, University of Oregon, Eugene, OR 97403, United States

[4]Department of Electrical and Computer Engineering, University of Toronto, 10 King's College Rd, Toronto, ON M5S 3G4, Canada

[5]Pohang Accelerator Laboratory (PAL), Pohang University of Science and Technology (POSTECH), Pohang 37673, Republic of Korea

[6]Research and Development Center, Saudi Aramco, Dhahran 31311, Saudi Arabia

[7]Department of Chemical & Biomolecular Engineering and Department of Chemistry, University of California, Berkeley, California 94720, United State

[8]Department of Electrical and Computer Engineering, Northwestern University, 2145 Sheridan Rd, Evanston, IL 60208, United States

[†]These authors contributed equally.

*Corresponding email: ted.sargent@northwestern.edu
ke-xie@northwestern.edu

Table of Contents

Supplementary Note 1. Comparison of carbonate and bicarbonate reactive capture systems

For KOH-based direct air capture (DAC), we primarily obtain a K_2CO_3-rich solution for subsequent electrolysis. In contrast, the K_2CO_3-based DAC yields a $KHCO_3$-rich solution. Currently, the most cost-effective and scalable DAC system uses an alkali hydroxide (e.g., KOH) solution to convert CO_2 into carbonate.[1]

(1) Thermodynamic analysis of KOH-based capture and K_2CO_3-based capture

(A) KOH as the capture liquid to produce K_2CO_3-rich post-capture liquid

$$CO_{2(g)} + 2KOH_{(aq)} \rightarrow K_2CO_{3\,(aq)} + H_2O_{(l)}$$

$$\Delta H_{rxn} = -\,191.73\frac{kJ}{mol}$$

This reaction is highly favorable because KOH dissociates completely in water, making it very effective at capturing CO_2.

(B) K_2CO_3 as the capture liquid to produce $KHCO_3$-rich post-capture liquid

$$CO_{2(g)} + K_2CO_{3(aq)} + H_2O_{(l)} \rightarrow 2KHCO_{3(aq)}$$

$$\Delta H_{rxn} = -\,96.07\frac{kJ}{mol}$$

K_2CO_3, on the other hand, is a weaker base compared to KOH. K_2CO_3 reacts with CO_2 to form $KHCO_3$, but this reaction is slower and less efficient. This means that K_2CO_3 doesn't have strong affinity for CO_2, making it more difficult to use for CO_2 capture.

(2) Kinetics analysis of KOH-based capture and K_2CO_3-based capture

For the kinetics and capital efficiency of the contactor to provide practical DAC, interaction of the KOH with CO_2 down to K_2CO_3, pH ~12, is realistic; whereas contacting all the way down to $KHCO_3$ (pH ~8) is not.[2] This is primarily because the concentration of CO_2 in air is very low (~400 ppm), and the capture kinetics are significantly slowed when the pH of the solution decreases from >14 in the KOH solution to ~12 in the K_2CO_3 solution. Our lab-scale experimental demonstration of DAC shown in **Supplementary Note 11** also supported the above claims.

In practical applications, converting K_2CO_3 to $KHCO_3$ requires up to 14 times more contactors than converting KOH to K_2CO_3 to maintain the same CO_2 capture rate. Since air contactor capital expenditures (CAPEX) account for roughly 20% of the total DAC cost, using a post-capture solution primarily composed of $KHCO_3$ is less practical in the near term unless air contactor costs decrease substantially.

(3) Energy analysis for syngas production

The pH mismatch between the DAC process and the bicarbonate electrolysis process requires additional external pH adjustment steps to align the pH levels of the two processes. Specifically, after DAC with

KOH absorbent yields a K_2CO_3-rich solution, a pH downshift step is necessary to convert this solution into a $KHCO_3$-rich solution for the subsequent bicarbonate electrolysis.

According to the literature, the most commonly used pH downshift unit is bipolar membrane electrodialysis (BPMED). The best-reported modeling showed the minimum energy consumption for BPMED is 23 GJ per tonne of CO_2.[3] This corresponds to 23/44*28 GJ per tonne of CO. Given the 2:1 H_2:CO molar ratio, 1 tonne of syngas contains 0.875 tonnes of CO, which adds up to 12.8 GJ for the production of 1 tonne of syngas.

We also experimentally demonstrated BPMED for pH downshift from a 1.5 M K_2CO_3 solution to a bicarbonate-rich solution (**Supplementary Fig. 1**). The experiments were conducted in two-chamber slim flow cells, a setup similar to what has been reported in the literature.[4] We used $Fe(CN)_6^{3-}/Fe(CN)_6^{4-}$ redox couples for the cathodic and anodic redox reactions. Both the cathode and anode were Pt/C electrodes with a loading of ~0.5 mg/cm² Pt. We used 0.4 M $K_3/K_4[Fe(CN)_6]$ at a flow rate of 10 ml/min for the catholyte and anolyte. Two pieces of cation exchange membranes (CEM, Nafion 212) were used for K^+ transport, and one piece of BPM (Fumasep) was used for water dissociation to produce H^+ and OH^-. 1.5 M K_2CO_3 and 1 M KOH were circulated in the middle two chambers. The H^+ from the BPM is coupled with K_2CO_3 in the middle chamber for pH downshift.

The results showed an average cell voltage of 2.1 V and an average charge efficiency of 50% for the pH downshift from carbonate to bicarbonate. The charge efficiency is defined as:

$$\text{Charge efficiency} = \frac{total\ charge\ used\ for\ downshift\ pH}{total\ passed\ charge} \times 100\%$$

The charge efficiency being ~50% suggests that the remaining charges were used for CO_2 gas release instead of converting carbonate to bicarbonate. This occurs because, at lower pH and with increased bicarbonate concentration, bicarbonate can react directly with H^+ to release CO_2, which leads to reduced charge efficiency. Based on our experimental results, the energy consumption for this BPMED pH downshift unit is 12.7 GJ per tonne of syngas, which is close to the predicted value reported in the literature.[3]

Based on these results, we incorporated the pH downshifter's energy consumption into the overall energy demand for state-of-the-art bicarbonate electrolysis systems. Assuming a FE_{CO} of 80% and a cell voltage of 3.5 V for bicarbonate electrolysis,[5,6] the energy consumption for bicarbonate electrolysis amounts to 47.3 GJ per tonne of syngas, with a total energy of 60 GJ/tonne syngas.

Fig. 4d compared the state-of-the-art bicarbonate electrolysis energy consumption and carbonate electrolysis in this work. Our work reported a total energy of 44 GJ/tonne syngas is much lower than the air-to-bicarbonate-to-syngas process.

(4) Local environment differences between carbonate and bicarbonate electrolysis

Supplementary Table 1. Comparison between carbonate and bicarbonate reactive systems.

Reactive capture system	bulk pH	local pH during electrolysis at the catalyst layer [a]	H^+ needed for one *i*-CO_2	*i*-CO_2 utilization (%)[b]
Bicarbonate	8.5	9-11	1	40-60
Carbonate	~12	13-14	2	>99

a. The local pH information is obtained from the literatures.[7-9]

b. *i*-CO_2 utilization is defined as follows:

$$i\text{ - CO2 utilization } = 1 - \frac{CO_2 \text{ gas detected at the outlet}}{\text{theroretical } i\text{ - }CO_2 \text{ generated at the membrane interface}}$$

Comparison of *i*-CO_2 generation:

For carbonate or bicarbonate electrolysis, the liquid form of CO_3^{2-} or HCO_3^- ions should be first converted into *in situ* CO_2 (g) and CO_2 (aq) for their continuous reduction into carbon products.

In the BPM-based carbonate electrolyzer, the *i*-CO_2 generation is based on the following equation:

$$CO_3^{2-} + 2H^+ \rightarrow CO_2 + H_2O$$

In comparison, in the bicarbonate electrolyzer, the *i*-CO_2 generation is based on the following equation:

$$HCO_3^- + H^+ \rightarrow CO_2 + H_2O$$

At 100 mA/cm^2 for electrolysis, the flow rate of CO_2 in carbonate system is calculated as follows:

$$\text{Flow rate}_{CO2} = \frac{0.1\,A\,cm^{-2} * 22.4\,L\,mol^{-1}}{96485\ \ C\,mol^{-1} * 2} * 1000 = \frac{0.1\,A\,cm^{-2} * 22.4\,L\,mol^{-1}}{96485\ \ A\,s\,mol^{-1} * 2} * 1000 = 0.01$$
$$\cdot\, cm^{-2} = 0.69\,mL \cdot min^{-1} \cdot cm^{-2}$$

The flow rate of CO_2 in bicarbonate electrolyzer is 0.69 × 2 = 1.38 $mL \cdot min^{-1} \cdot cm^{-2}$.

As a result, *i*-CO_2 generation in carbonate systems requires twice the stoichiometric amount of H^+, leading to half the *i*-CO_2 evolution compared to bicarbonate electrolyzers. Consequently, the theoretical local supply rate of *i*-CO_2 in carbonate system is half of that in bicarbonate system.

Comparison of *i*-CO_2 loss

During electrolysis, *i*-CO_2 loss are due to the following reactions:

$$CO_2(g) + OH^-(aq) \rightleftharpoons HCO_3^-(aq)$$

$$CO_2(g) + CO_3^{2-}(aq) + H_2O(l) \rightleftharpoons 2HCO_3^-(aq)$$

$CO_2(g) + 2OH^-(aq) \rightleftharpoons CO^{2-}_3(aq) + H_2O(l)$

In the bicarbonate system, the local pH at the cathode layer is significantly lower than in the carbonate system (pH 9-11 vs. 13-14), making the carbonate system more prone to *i*-CO_2 loss. In the bicarbonate system, locally formed CO_3^{2-} and HCO_3^- act as a buffer, helping to maintain a moderately alkaline pH. In contrast, the carbonate electrolyzer lacks buffering capacity in its CO_3^{2-}/OH^- mixture, making it difficult to stabilize the local pH, resulting a great *i*-CO_2 loss because of the acid-base neutralization reaction.

This necessitates the design of catalysts in carbonate system that are not only stable under alkaline conditions but also capable of maximizing local *i*-CO_2 utilization and conversion into the desired product (CO).

Comparison of *i*-CO_2 utilization

The carbonate system demonstrated exceptionally high *i*-CO_2 utilization (>99%) compared to the bicarbonate electrolyzer (40-60%). The lower *i*-CO_2 utilization in bicarbonate system is due to (1) the spontaneous decomposition of HCO_3^-; (2) a doubled *i*-CO_2 supply rate in bicarbonate system; (3) A much lower bulk pH (~8.5) and local pH (9-11) for bicarbonate system.

The high *i*-CO_2 utilization in carbonate system allows for the production of pure syngas at the outlet, eliminating the need for *i*-CO_2 separation and significantly reducing overall costs.

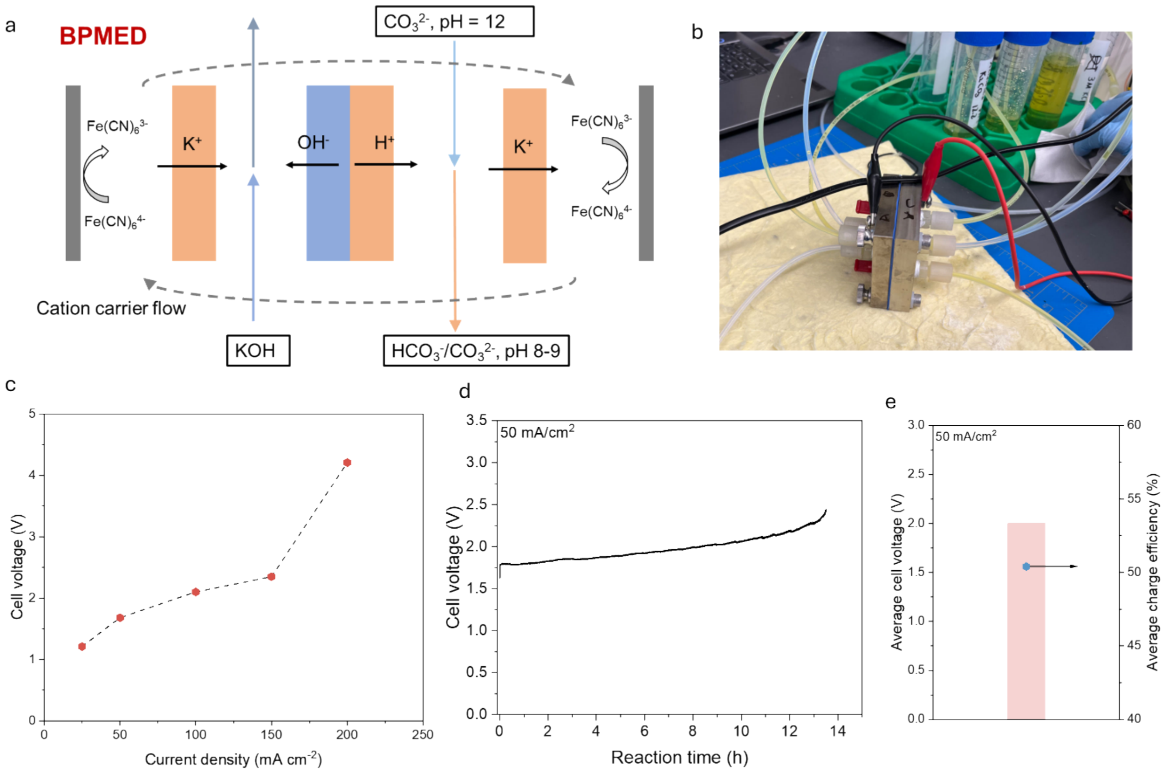

Supplementary Figure 1. (a) Schematic illustration of the set-up of BPMED system to downshift pH. (b) Photo of pH downshift set-up in the slim flow cell. (c) Cell voltage-current density profile at different current densities. This cell voltage is recorded at the initial 5 minutes during the electrolysis. (d) Cell voltage-time profile for downshift carbonate solution to a bicarbonate-rich solution at 50 mA cm^{-2}. (e) Average cell voltage and charge efficiency during the 13.5-hour operation at 50 mA cm^{-2} for pH downshift from a carbonate solution to a bicarbonate-rich solution. The anolyte consisted of 1.5 M K_2CO_3, while the catholyte contained 1 M KOH. During electrolysis, anolyte pH decreased and catholyte pH increased. The gradual rise in cell voltage may be attributed to an increase in Nernst loss, driven by the growing pH difference between the cathode and anode, as described by the equation: Nernst loss = 0.059 × ΔpH. Charge efficiency is defined as the percentage of charge utilized for converting carbonate to bicarbonate, rather than for CO_2 release from the carbonate/bicarbonate solution.

Supplementary Note 2. Comparison of CEM and BPM systems for carbonate electrolysis

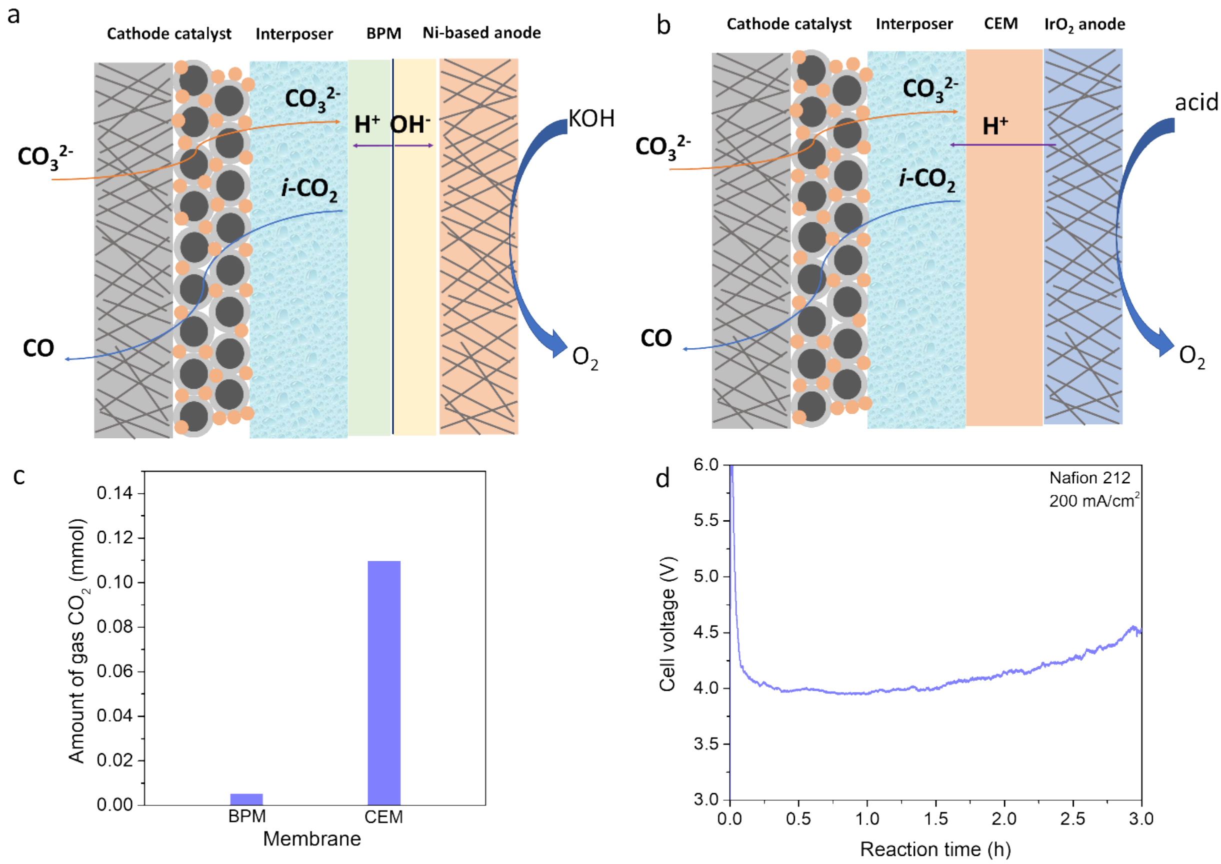

Supplementary Figure 2. Experimental comparison of CEM and BPM systems for carbonate electrolysis. Schematic illustration of the comparison between (a) BPM and (b) CEM-based systems for carbonate reduction. (c) The amount of CO_2 gas at the outlet of electrolyzers with BPM and CEM was measured during electrolysis at 200 mA cm^{-2} using the CoPc/PDA-HP catalyst for 15 minutes. The CO_2 gas at the catholyte outlet was quantified using GC. In the CEM-based system, the IrO_2 anode is used, and the anolyte is 0.5 M H_2SO_4. (d) Cell voltage – reaction time profile. The detailed experimental setup and conditions shown in the Method section.

In the BPM-based system (**Supplementary Figure 2a**), *i*-CO_2 is generated from the reaction between CO_3^{2-} and H^+. The H^+ is derived from water dissociation in the BPM. Because of the use of both cation exchange layer (CEL) and anion exchange layer (AEL) in the BPM, crossover of ions can be largely eliminated, and asymmetric electrolyte pH can be used. A continuous and stable supply of H^+ is generated by the dissociation of water at the junction between the CEL and AEL, driven by the electric field.

In contrast, in the CEM-based system (**Supplementary Figure 2b**), an acid must be used as the anolyte, with acidic oxygen evolution reaction (OER) occurring at the anode. Unlike the BPM-based system, where proton generation and transport across the membrane are directly tied to the applied current (via water dissociation), the CEM-based system has multiple proton sources: (1) a concentration gradient from the acidic anode to the alkaline cathode, and (2) proton migration driven by the electric field. As a result, more H^+ ions combine with CO_3^{2-} ions to form *i*-CO_2 in the CEM-based electrolyzer, leading to a higher *i*-CO_2 concentration but lower utilization efficiency. Moreover, the proton-rich local environment favors HER over *i*-CO_2RR, making it challenging to improve the FE_{CO}.

Our experimental results (**Supplementary Figure 2c**) using a MEA for carbonate electrolysis with both BPM and CEM configurations revealed notable differences in the CO_2 concentration detected at the outlet, with significant CO_2 loss in the CEM system. This CO_2 loss leads to increased energy consumption due to the need for CO_2 recirculation and separation.

In addition, the CEM-based system is not amenable to steady-state operation without continuous addition of acid and salt to the anolyte, as the initial pH gradient will be eliminated because of the co-ion transport and neutralization (**Supplementary Figure 2d**). Moreover, the use of a noble metal catalyst, such as IrO_2 at the anode, adds further capital costs to the overall process.

Therefore, a detailed comparison of BPM- and CEM-based systems for carbonate electrolysis shows that the CEM-based system, operating with an acidic anolyte and noble metal anode, is neither stable nor practical for real-world applications.

Supplementary Note 3. Local formation, transport, and conversion of *i*-CO_2 in carbonate electrolyzer (Supplementary Figures 3-5)

Owing to the low concentration of CO_2 (~400 ppm) in air, the dominant species is carbonate (CO_3^{2-}) rather than bicarbonate (HCO_3^-) in an energy-efficient direct air capture system.[1,10] The full conversion of carbonate to bicarbonate would require much more energy consumption because of the slow kinetics for CO_2 capture at the capture liquid with lower pH. As such, in the direct air capture system, it is necessary to conduct carbonate conversion instead of bicarbonate conversion.

Local generation of *i*-CO_2 in carbonate system

For carbonate electrolysis, the liquid form of CO_3^{2-} should be first converted into *in situ* CO_2 (g) and CO_2 (aq) for their continuous reduction into carbon products.

In the BPM-based carbonate electrolyzer, the *i*-CO_2 generation is based on the following equation:

$$CO_3^{2-} + 2H^+ \rightarrow CO_2 + H_2O$$

At 100 mA for electrolysis, the theoretical supply rate of CO_2 in carbonate system is calculated as follows:

$$\text{Flow rate}_{CO2} = \frac{0.1\,A\,cm^{-2} * 22.4\,L\,mol^{-1}}{96485\ \ C\,mol^{-1} * 2} * 1000 = \frac{0.1\,A\,cm^{-2} * 22.4\,L\,mol^{-1}}{96485\ \ A\,s\,mol^{-1} * 2} * 1000 = 0.01$$
$$\cdot\, cm^{-2} = 0.69\,mL \cdot min^{-1} \cdot cm^{-2}$$

The supply of *i*-CO_2 from the CEL/electrolyte interface to the cathode layer (CL) in the carbonate electrolyzer is limited by the side reaction as follows:

CO_2 loss at the CEL/catholyte interface:

$$CO_3^{2-}(aq) + H^+ \rightleftharpoons HCO_3^-(aq)$$

At the CEL/catholyte interface, some CO_3^{2-} may react with H^+ to form HCO_3^- instead of releasing CO_2. This process is highly dependent on the membrane's surface pH and the catholyte flow rate.

CO_2 loss on the cathode layer (CL):

In the cathode layer, the bulk electrolyte consists of a highly concentrated K_2CO_3 solution (pH >12). In addition, during electrolysis, no matter for HER or CO_2RR, significant amounts of OH^- are generated in the cathode layer. The following side reactions occurred at the cathode layer, resulting in a significant loss of *i*-CO_2.

$$CO_2(g) + OH^-(aq) \rightleftharpoons HCO_3^-(aq)$$

$$CO_2(g) + CO_3^{2-}(aq) + H_2O(l) \rightleftharpoons 2HCO_3^-(aq)$$

$CO_2(g) + 2OH^-(aq) \rightleftharpoons CO^{2-}_3(aq) + H_2O(l)$

Local conversion of i-CO_2 to CO on the cathode layer in the carbonate system

i-CO_2 can be converted into syngas with the following reactions:

(1) Production of CO:

i-CO_2 conversion of 100%: $CO_2 + H_2O + 2e^- \rightarrow CO + 2OH^-$

i-CO_2 conversion of 50%: $2CO_2 + 2e^- \rightarrow CO + CO^{2-}_3$

i-CO_2 conversion of 33%: $3CO_2 + H_2O + 2e^- \rightarrow CO + 2HCO^-_3$

(2) Production of H_2:

$2H_2O + 2e^- \rightarrow H_2 + 2OH^-$

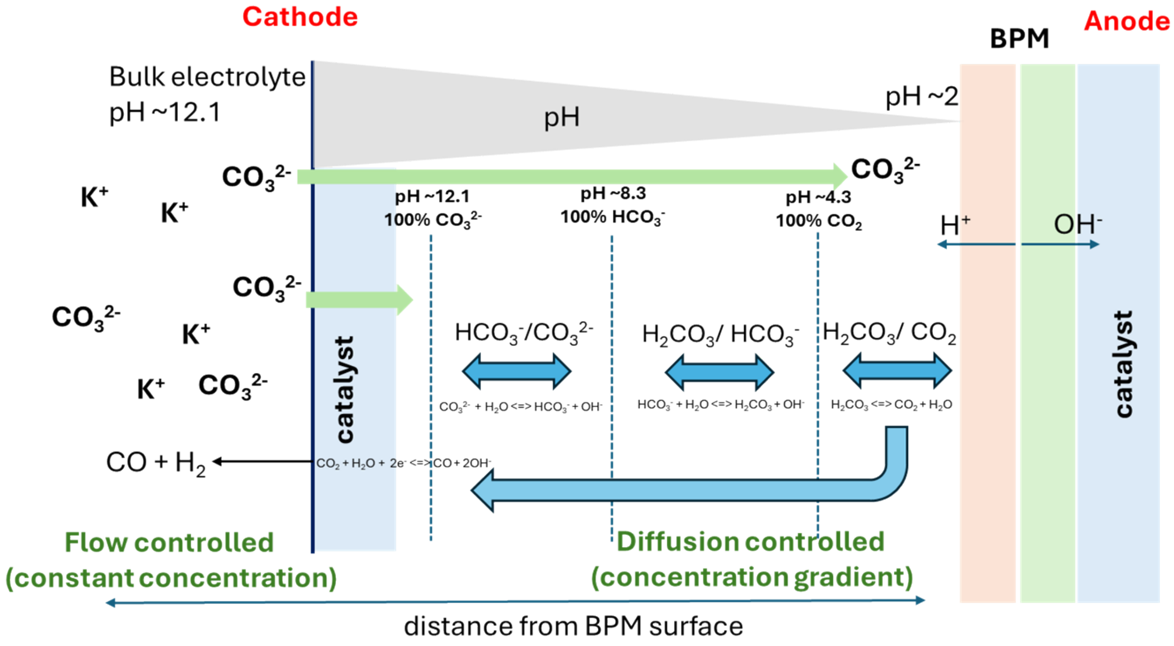

Supplementary Figure 3. Schematic illustration the local environments of catalyst interface. A pH gradient exists from the BPM interface (pH ~2) to the gas diffusion layer (GDL) of the cathode catalyst (pH ~12). The continuous supply of 1.5 M K_2CO_3 solution ensures a flow-controlled, constant concentration of carbonate at the catalyst surface. At the BPM interface, CO_3^{2-} reacts with H^+ to produce CO_2. This CO_2 undergoes diffusion-controlled transport, while various chemical equilibria are established in the local region between the BPM and the cathode surface.

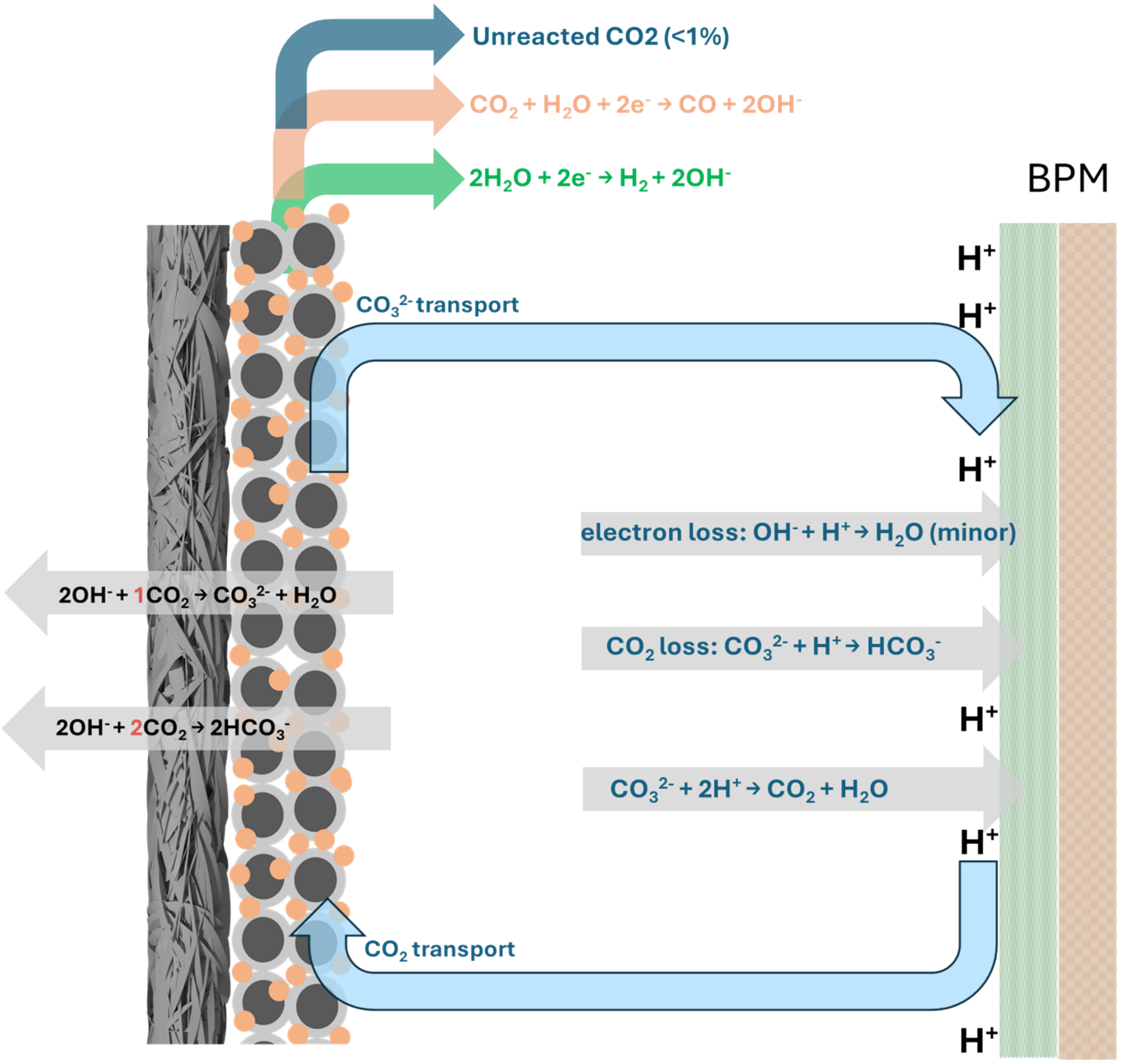

Supplementary Figure 4. Schematic illustration of the reactions occurring in the local environment of the BPM-based system for carbonate electrolysis.

Water dissociation in the BPM

$$H_2O(l) \rightleftharpoons OH^-(aq) + H^+(aq) \qquad K_w = 10^{-14}$$

OER at the anode:

$$4OH^-(aq) \rightleftharpoons O_2(g) + 2H_2O(l) + 4e^- \qquad E^\circ = 0.401V \text{ (vs. SHE)}$$

Reaction occurred at the BPM interface:

Reaction 1: $CO^{2-}_3(aq) + 2H^+(aq) \rightleftharpoons CO_2(g) + H_2O(l)$

The equilibrium constant for this reaction is related to the combination of the two dissociation constants of carbonic acid:

$$K_a1 \approx 4.3 \times 10^{-7} \text{ and } K_a2 \approx 4.7 \times 10^{-11}$$

$$K = \frac{1}{K_a1 \times K_a2} \approx \frac{1}{(4.3 \times 10^{-7}) \times (4.7 \times 10^{-11})} \approx 5 \times 10^{16}$$

Reaction 2: $CO_3^{2-}(aq) + H^+(aq) \rightleftharpoons HCO_3^-(aq)$

The equilibrium constant for this reaction is the inverse of the second dissociation constant of carbonic acid (K_{a2})

$$K = \frac{1}{K_a2} \approx \frac{1}{4.7 \times 10^{-11}} \approx 2.13 \times 10^{10}$$

Reaction 3: $HCO_3^-(aq) + H^+(aq) \rightleftharpoons CO_2(g) + H_2O(l)$

The equilibrium constant for this reaction is the inverse of the first dissociation constant of carbonic acid (K_{a1}).

$$K = \frac{1}{K_a1} \approx \frac{1}{4.3 \times 10^{-7}} \approx 2.33 \times 10^{6}$$

CO_2 and ion transfer from BPM to the cathode layer

Reaction 1: $CO_2(g) + H_2O(l) \rightleftharpoons H_2CO_3(aq)$

$$K \approx 1.7 \times 10^{-3}$$

This small value indicates that at equilibrium, only a small fraction of CO_2 in water exists as carbonic acid, while the majority remains as dissolved CO_2.

Reaction 2: $H_2CO_3(aq) + OH^-(aq) \rightleftharpoons HCO_3^-(aq) + H_2O(l)$

For the reaction between H_2CO_3 and OH^-, the equilibrium constant K is related to the inverse of K_{a1} because the reaction is the reverse of the acid dissociation process. Since OH^- neutralizes H^+, the equilibrium constant is:

$$K = \frac{[HCO_3^-]}{[H_2CO_3][OH^-]} = \frac{1}{K_a1 \times K_w} = \frac{1}{4.3 \times 10^{-7} \times 1 \times 10^{-14}} \approx 2.33 \times 10^{20}$$

Reaction 3: $HCO_3^-(aq) + OH^-(aq) \rightleftharpoons CO_3^{2-}(aq) + H_2O(l)$

For the reaction of HCO_3^- with OH^- to form carbonate, the equilibrium constant is related to the reverse of the second dissociation of carbonic acid (K_{a2}).

$$K = \frac{[CO_3^{2-}]}{[HCO_3^-][OH^-]} = \frac{1}{K_a2 \times K_w} = \frac{1}{(4.7 \times 10^{-11}) \times (1 \times 10^{-14})} \approx 2.13 \times 10^{24}$$

On the cathode layer:

Main reactions occurred on the cathode:

$CO_2(g) + 2H_2O + 2e^- \rightleftharpoons CO(g) + 2OH^-$ $E^\circ = -0.93V$ (vs. SHE)

$2H_2O + 2e^- \rightarrow H_{2(g)} + 2OH^-{}_{(aq)}$ $E^\circ = -0.827V$ (vs. SHE)

Side reactions of CO_2 loss:

$CO_2(g) + OH^-(aq) \rightleftharpoons HCO_3^-(aq)$

$CO_2(g) + CO^{2-}_3(aq) + H_2O(l) \rightleftharpoons 2HCO_3^-(aq)$

$CO_2(g) + 2OH^-(aq) \rightleftharpoons CO^{2-}_3(aq) + H_2O(l)$

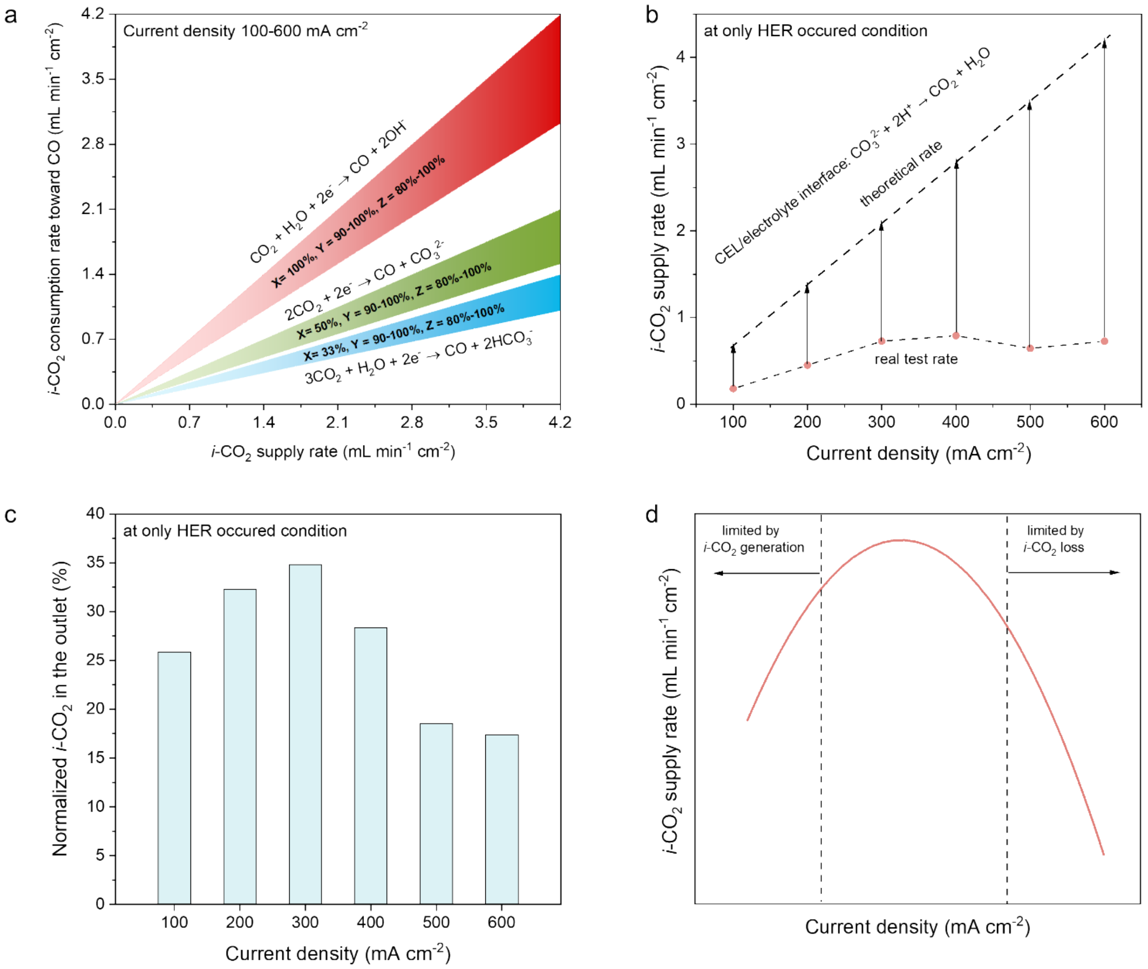

Supplementary Figure 5. Statistical analysis of local *i*-CO_2 supply and utilization. (a) Statistical analysis of the *i*-CO_2 supply and utilization in the BPM-based carbonate electrolyzer for the conversion of CO_2 to CO. We assumed that the CO_2 conversion at the cathode surface is X = 100%, 50%, and 33%; the CO_2 generation efficiency at the BPM surface is Y = 90%–100%; and the CO_2 transport efficiency from the BPM surface to the cathode surface is Z = 80%–100%. A detailed analysis of the competing reactions is presented in **Supplementary Note 3**. (b) Supply rate of *i*-CO_2 and (c) normalized *i*-CO_2 concentration in the outlet of the catholyte. In (b), we analyze the differences between the actual measured *i*-CO_2 rate in the outlet and the calculated theoretical rate. (d) Schematic illustration of the *i*-CO_2 supply rate at different current densities. In the low current density region, the process is primarily limited by *i*-CO_2 generation. In the high current density region, it is mainly limited by *i*-CO_2 loss due to acid-base neutralization reactions on the cathode layer.

Due to the highly complex chemical environment in real conditions for carbonate electrolysis, it is challenging to directly measure the local environment of the system and quantify the *i*-CO_2 concentration at the CEL/catholyte interface and within the cathode layer (CL). We first conducted a straightforward statistical analysis of the *i*-CO_2 consumption rate for the desired CO_2-to-CO conversion at theoretical i-CO_2 supply rate (**Supplementary Figure 5a**). The deviation in the CO generation rate from the theoretical i-CO_2 supply is attributed to i-CO_2 losses during the processes of X, Y, and Z, as mentioned above.

To experimentally simulate the i-CO_2 losses at different current density, we employed a CO_2-to-CO inert cathode to simulate the system and quantify CO_2 gas evolution at the catholyte outlet using gas chromatography. The cathode used was Pt/C on hydrophilic carbon paper (0.5 mg cm^{-2} Pt), where only the HER occurred. We measured the CO_2 concentration and calculated the actual i-$CO_2(g)$ supply rate under these HER conditions (**Supplementary Figure 5b**). Additionally, we calculated the normalized i-$CO_2(g)$ in the outlet (**Supplementary Figure 5c**), as shown by the following equation:

$$\text{Normalized } i\text{-}CO_2(g) = \frac{tested\ i - CO_2\ (g)\ supply\ rate\ in\ the\ outlet}{theoreticl\ i - CO_2\ supply\ rate} \times 100\%$$

Although only the HER occurred, we still observed that the i-CO_2 gas supply rate was significantly lower than the theoretical rate (**Supplementary Figure 5b**). This is primarily due to various side reactions taking place at the CEL/catholyte interface, during transport, and within the cathode layer.

The normalized i-CO_2 (g) supply rate exhibited a volcano-shaped trend, peaking at current densities of 200–300 mA/cm^2 (**Supplementary Figure 5c**). At lower current densities, such as 100 mA/cm^2, the low i-CO_2 supply rate may be attributed to inefficient i-CO_2 generation (**Supplementary Figure 5d**). This is because the H^+ supply rate at the CEL surface, and consequently the surface pH, is strongly dependent on current density.[9] At 100 mA/cm^2, the surface pH of CEL was not that low and consequently CO_3^{2-} couples with H^+ and produced significant amount of HCO_3^- rather than release of i-CO_2. At high current densities, a lower surface pH of CEL may promote the direct reaction of CO_3^{2-} with H^+ to release CO_2, rather than forming HCO_3^-.

In the high current density region (>300 mA/cm^2), the normalized i-CO_2 supply rate decreases further, likely due to excessive OH^- generation from the electrolysis reactions at the cathode, creating a highly basic environment at the cathode layer (**Supplementary Figure 5d**). Under such conditions, there is significant i-CO_2 loss as it reverts to (bi)carbonate.

The optimal i-$CO_2(g)$ supply rate was observed in the 200–300 mA/cm^2 range. This trend aligns with the carbonate electrolysis test results using the CoPc/HP and CoPc/NP catalysts, where CO Faradaic efficiency (FE) was slightly higher at 200 mA/cm^2 compared to 100 mA/cm^2.

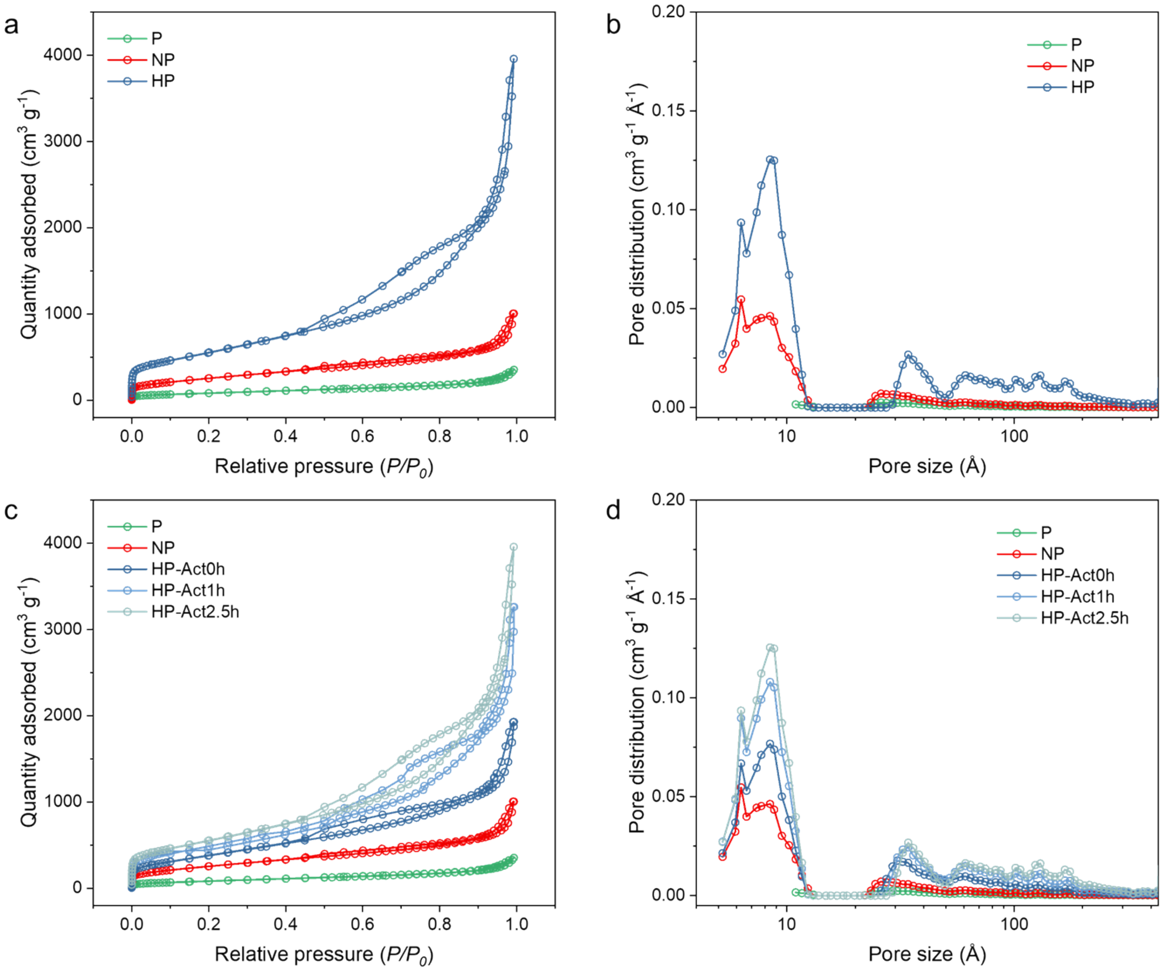

Supplementary Figure 6. BET analysis. (a,c) BET isothermal plot and (b,d) pore size distribution on various carbons. In (a) and (b), HP refers to the optimal meso-to-micro ratio achieved after 2.5 hours of CO_2 activation. (c) and (d) display the CO_2 activation at durations of 0 hours, 1 hour, and 2.5 hours.

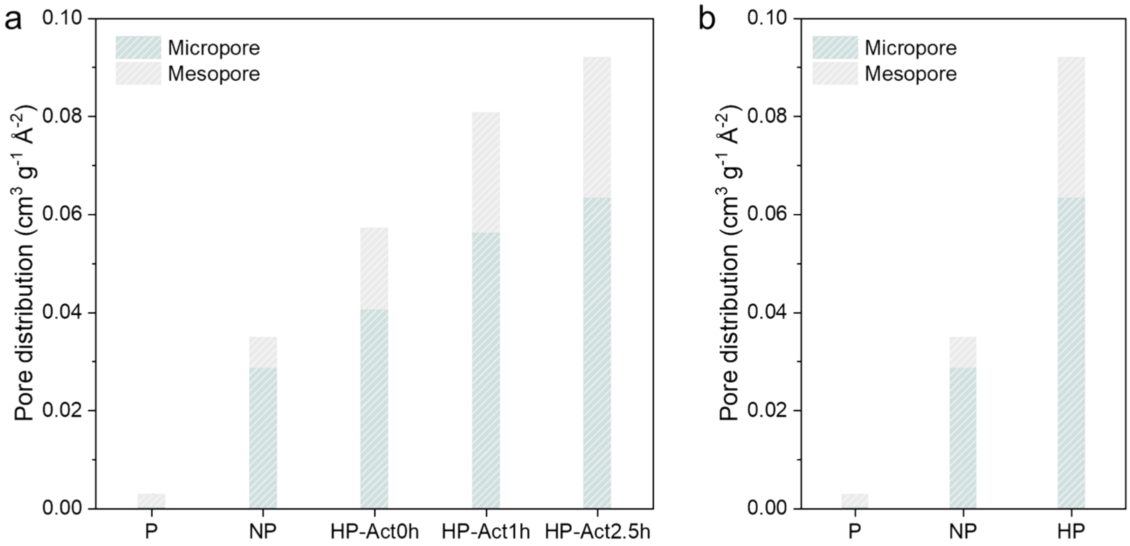

Supplementary Figure 7. Pore distribution analysis. (a) – (b) Pore volume distributions of various carbons with the meso-to-micro pore ratio. In (b), HP refers to the optimal meso-to-micro ratio achieved after 2.5 hours of CO_2 activation.

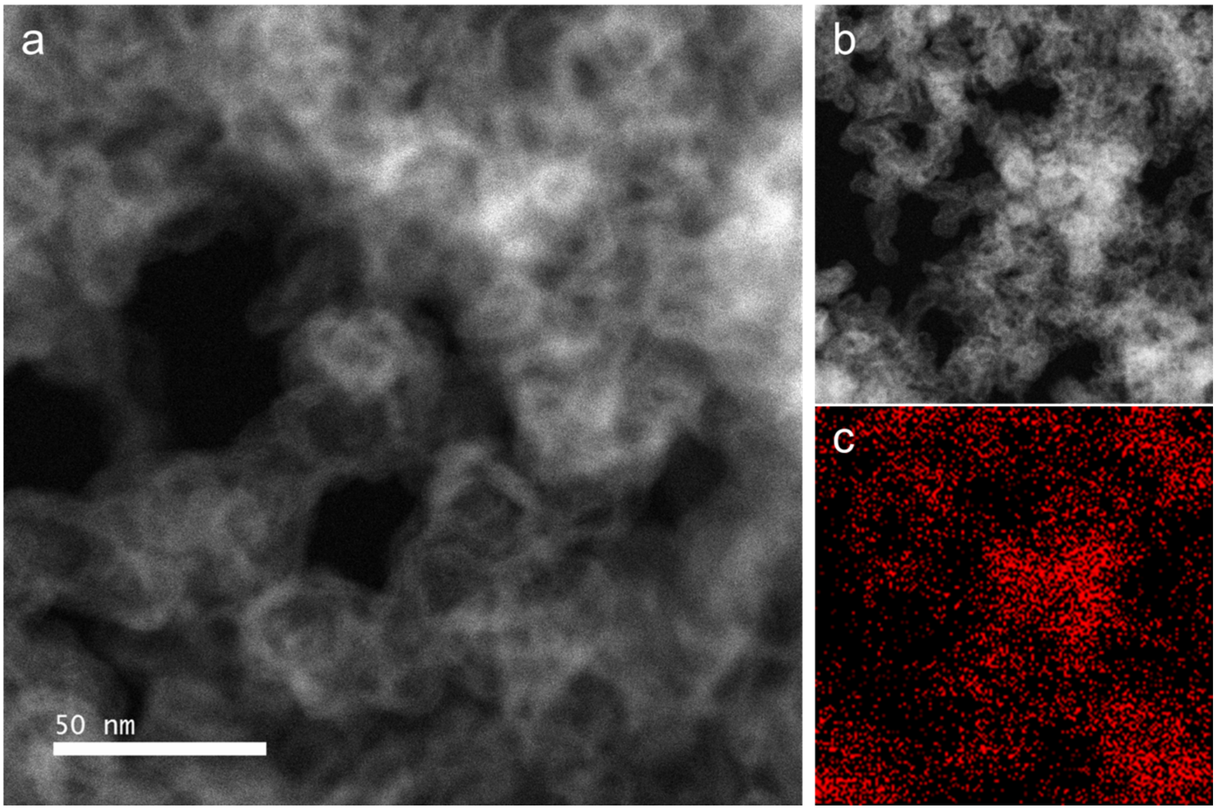

Supplementary Figure 8. (a) HRTEM image and (b) HAADF-STEM-EDS mapping of hierarchically porous carbon (HP).

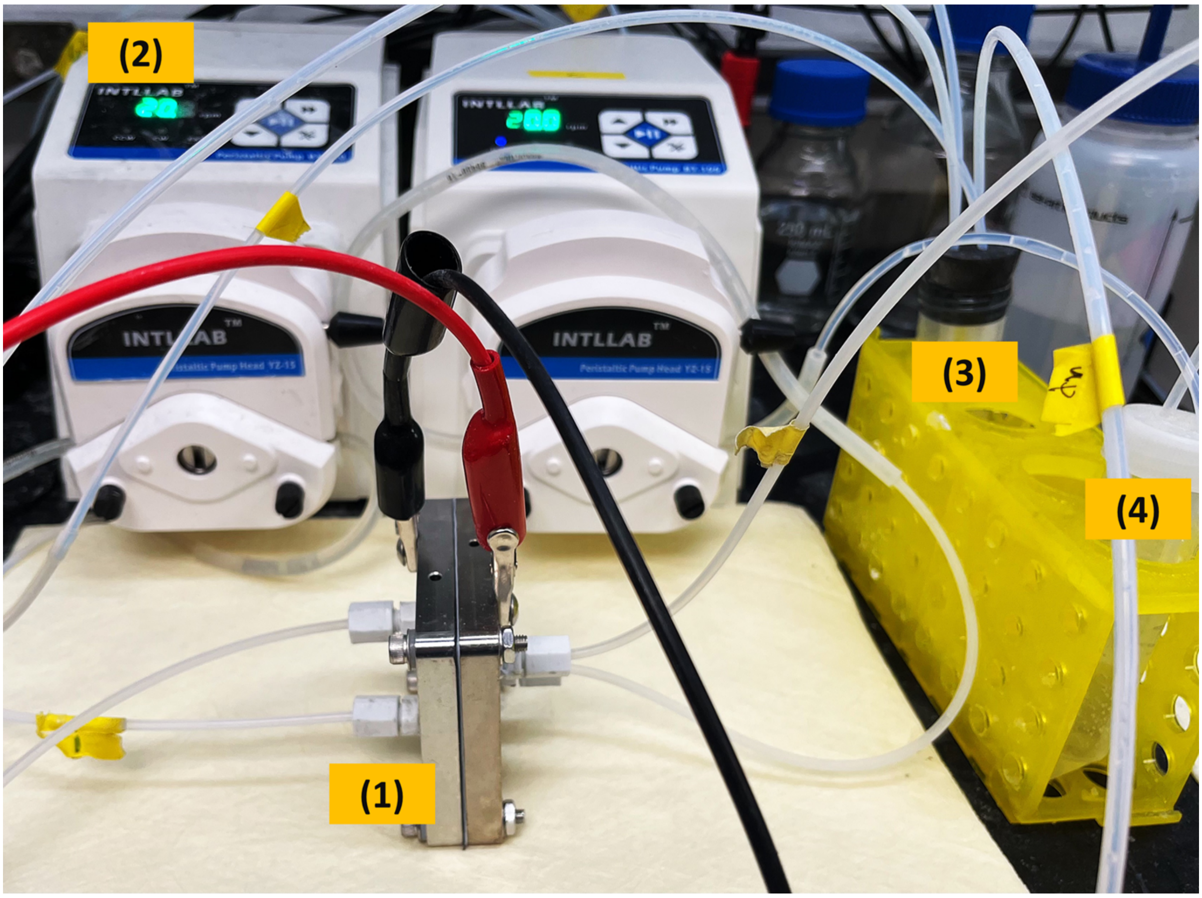

Supplementary Figure 9. Experimental set-up for the carbonate electrochemical cell assembly. In this Figure, (1) is the BPM-based electrolyzer. (2) is the peristaltic pump. (3) is the catholyte reservoir with a gas tight cap. Four holes are used in this rubber cap, including two lines for catholyte circulating, and two lines for Ar gas purging. (4) is the anolyte reservoir.

Supplementary Note 4. EIS and complex capacitance analysis

Electrochemical impedance spectroscopy (EIS) analysis was carried out to explore the dynamic behaviors within porous carbon structures under non-Faradaic conditions. EIS is a widely employed technique for investigating electrochemical systems, enabling the study of reaction mechanisms in a non-destructive manner. The total capacitance and the relaxation time constant (τ_o) of the model catalysts are obtained from EIS response through the complex capacitance analysis. In general, complex capacitance C(*ω*) is defined as follows:

$$Z(\omega) = \frac{1}{j\,\omega\,C(\omega)}$$

$$C(\omega) = C^{'}(\omega) - j\,C''(\omega)$$

$$C^{'} = \frac{-Z''(\omega)}{\omega|Z(\omega)|^2},\ C^{''} = \frac{Z'(\omega)}{\omega|Z(\omega)|^2}$$

Where $Z(\omega)$ is impedance and ω is frequency. The real part of complex capacitance ($C'(\omega)$) indicates the capacitance as a function of frequency and the imaginary part ($C''(\omega)$) is related to the energy dissipation of the capacitor by an irreversible process, such as IR drop and irreversible Faradaic charge transfer. From the peak frequency of $C''(\omega)$, the relaxation time constant (τ_o) is calculated as below.

$$\tau_o = (2\pi f_o)^{-1}$$

where the f_o is the peak frequency. The relaxation time constant, τ_o, is highly related to the penetrability that is defined by the pore structure of electrodes and electrochemical parameters in pores.

According to the literature,[11] the total capacitance (C_{dl}) is typically determined by extracting the flat value from the plot of $C'(\omega)$ in low frequency region. However, in our samples, the presence of flat features is not clearly observed. Instead, we estimated the total static capacitance (C_{dl}) of PDA-treated carbons compared with the values from the integrated area under $C''(\omega)$ curves. The integrated area under the $C''(\omega)$ is proportional to the capacitance of carbons based on the Kramers- Kronig relations, as followed below.

$$A = -\int_{-\infty}^{\infty} C^{''}(\omega) d\log f = 0.682\ C_{dl}$$

where A is the peak area under $C''(\omega)$ curves. Due to the technical hardness of very low frequency region, we calculated the A by double the right half-side of curves (the shadowed part in **Supplementary Figure 10**).

$$C_{dl} = -\frac{2}{0.682}A_{right-half},\ A_{right-half} = \int_{f_o}^{10^5} C^{''}(\omega)\ d\log f$$

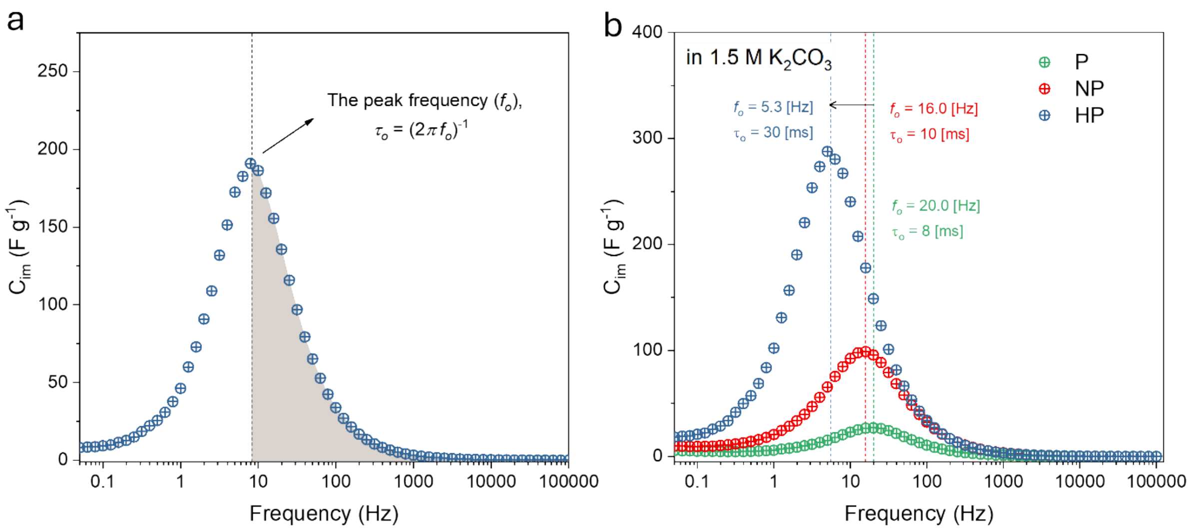

Supplementary Figure 10. EIS analysis. (a) Imaginary part of complex capacitance (C_{im}) obtained by complex capacitance analysis through EIS method. Relaxation time constant (τ_o) is calculated from the peak frequency (f_o) of C_{im} using the relation $\tau_o = (2\pi f_o)^{-1}$. The total static capacitance (C_{dl}) is obtained by double the integration area of the right half-side of curves (denoted as the shadowed part). (b) Imaginary capacitance plots of three different carbon supports: P, NP and HP. The HP used the optimum meso-to-micro ratio, the detailed optimization of HP was shown in **Supplementary Figure 49**.

The total capacitance (C_{dl}) and the relaxation time constant (τ_o) based on the above analysis are related to the effective/active electrochemical surface area and the speed of transport within the porous structure, respectively. The total capacitance (C_{dl}), obtained by integration of the complex capacitance function with frequency, is a strong function of the materials preparation, with the HP having by far the largest (~476 F g^{-1} compared to ~220 and ~65 F g^{-1} for the NP and P supports respectively). Interestingly, the effective relaxation time constant (τ_o) for species transport within the porous electrodes shows a slight increase, indicating longer stationary times, but it demonstrates only a relatively weak function of the apparent gravimetric capacitance. For example, the HP shows ~7.3 times higher maximum capacitance than P but a τ_o that is only 3.7 times as long (30 ms versus 8 ms).

In summary, this analysis demonstrates that HP not only significantly increases the effective surface area by nearly an order of magnitude, but does also in a way that does slightly slow down the transport processes essential to device operation. Further optimization using this type of analysis may be useful in driving additional performance gains toward a commercial device.

Supplementary Table 2. Elemental analysis of carbon support materials.

Samples	Carbon (wt%)	Hydrogen (wt%)	Nitrogen (wt%)	Oxygen (wt%)
P	97.61	0.27	0.09	<0.1
PDA-P	93.87	0.52	**0.87**	1.99
NP	97.81	0.22	<0.05	<0.1
PDA-NP	89.60	0.88	**1.90**	4.00
HP	97.69	0.20	<0.05	<0.1
PDA-HP	87.18	1.24	**2.21**	4.49

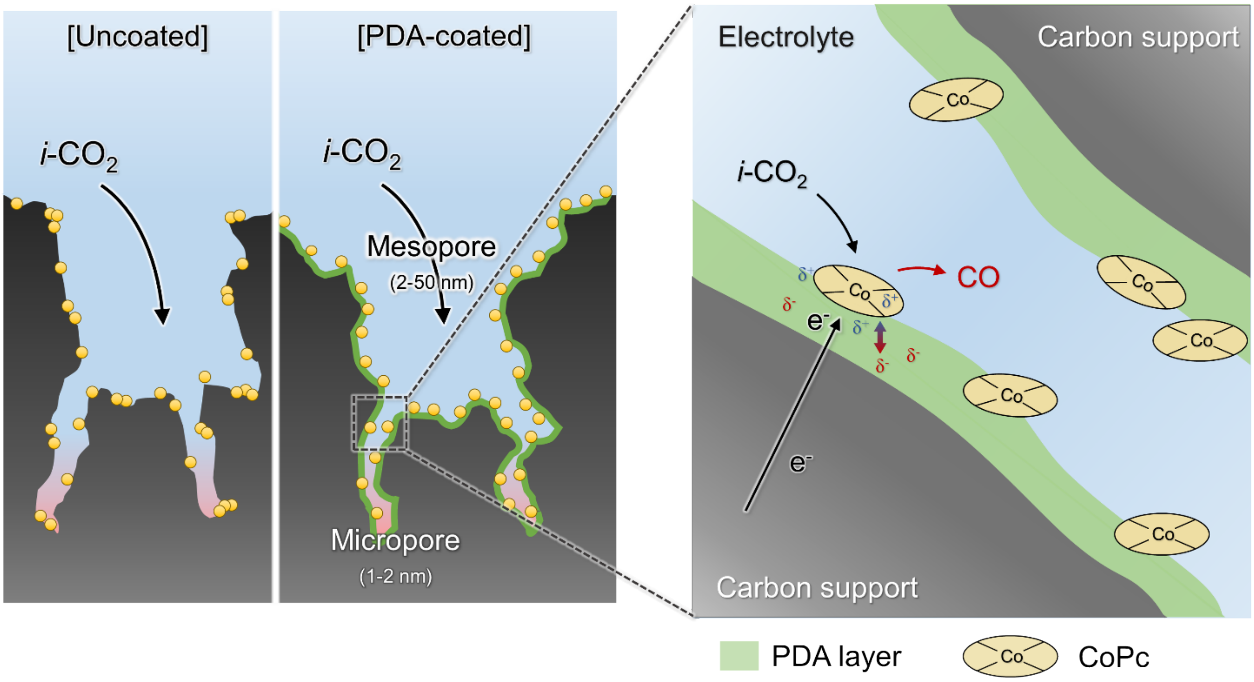

Supplementary Figure 11. Schematic illustration of CoPc molecules dispersed on a PDA-coated hierarchical porous carbon support, facilitating the diffusion of *i*-CO_2, enhancing the dispersion of molecular catalysts, and optimizing the electronic properties of the Co center.

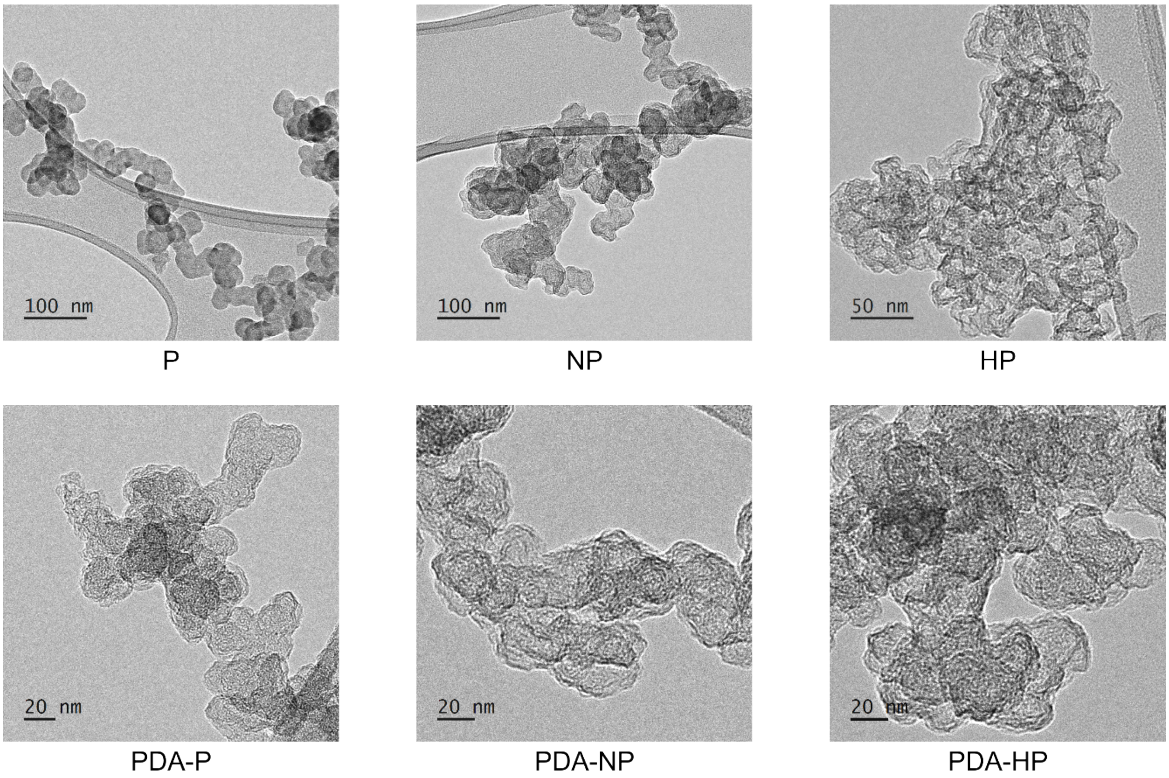

Supplementary Figure 12. HRTEM images of various carbons before and after PDA coating.

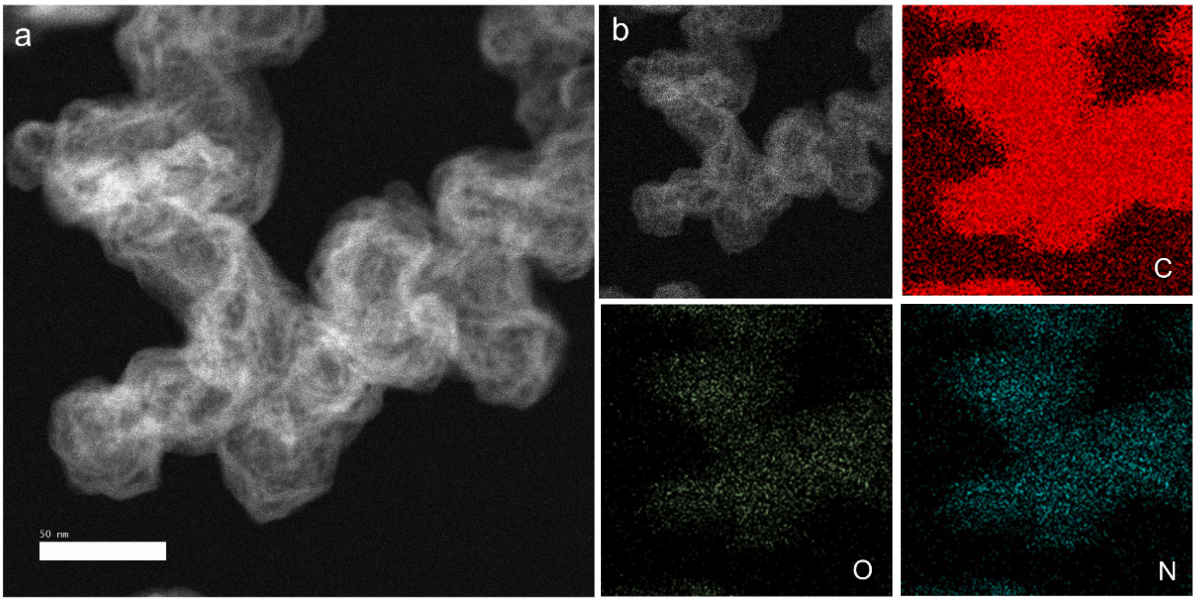

Supplementary Figure 13. (a) HRTEM image and (b) HAADF-STEM-EDS mapping of PDA-treated hierarchically porous carbon (PDA-HP).

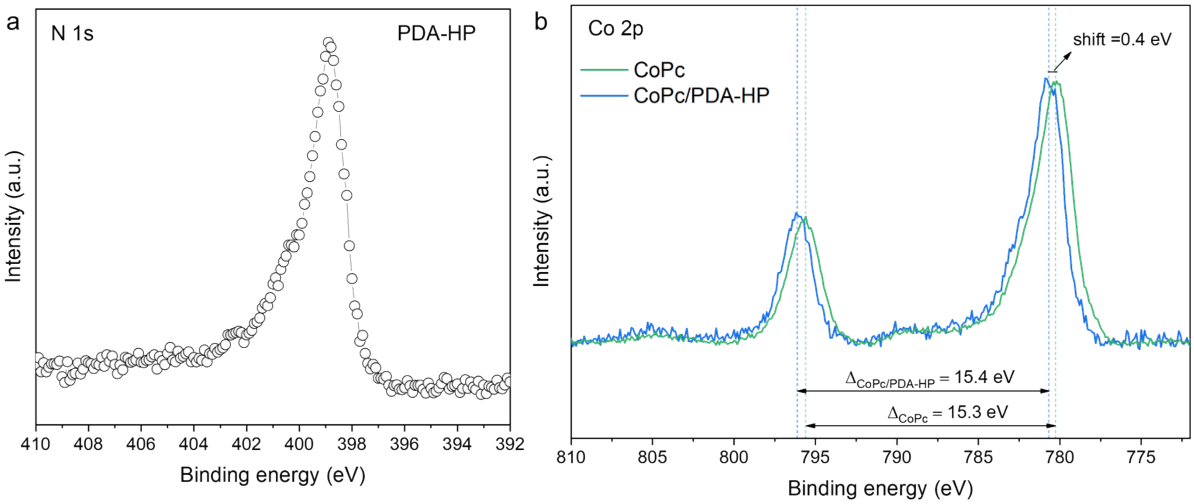

Supplementary Figure 14. XPS analysis of PDA-HP, CoPc, and CoPc/PDA-HP. (a) XPS N 1s signal of PDA-HP. (b) XPS Co 2p spectra of supported and un-supported CoPc on PDA-treated carbon material.

XPS analysis confirmed that nitrogen was successfully incorporated into the carbon supports via PDA coating, with amino group nitrogen being dominant in PDA-HP. After introducing the CoPc molecular catalysts, the Co *2p* spectrum of CoPc/PDA-HP exhibited an upshift to a higher binding energy compared to both unsupported CoPc and CoPc/PDA-HP. Additionally, the spin-orbit splitting (15.4 eV) of CoPc/PDA-HP was larger than that of unsupported CoPc, indicating a lower charge density at the Co sites. This suggests that the Co sites in CoPc become electron-deficient upon deposition onto the PDA-HP supports.

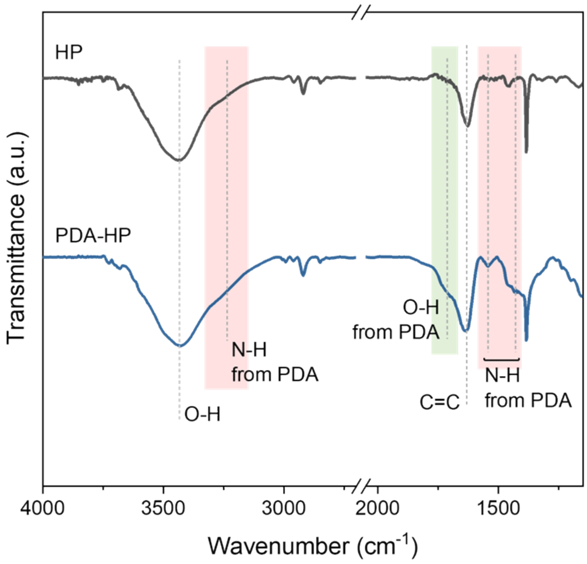

Supplementary Figure 15. FTIR on HP and PDA-HP.

The surface functional groups on the carbon supports were further confirmed by FTIR analysis. After PDA polymer coating on the HP and other carbon supports, both amino (N-H) and hydroxyl (O-H) groups were detected.

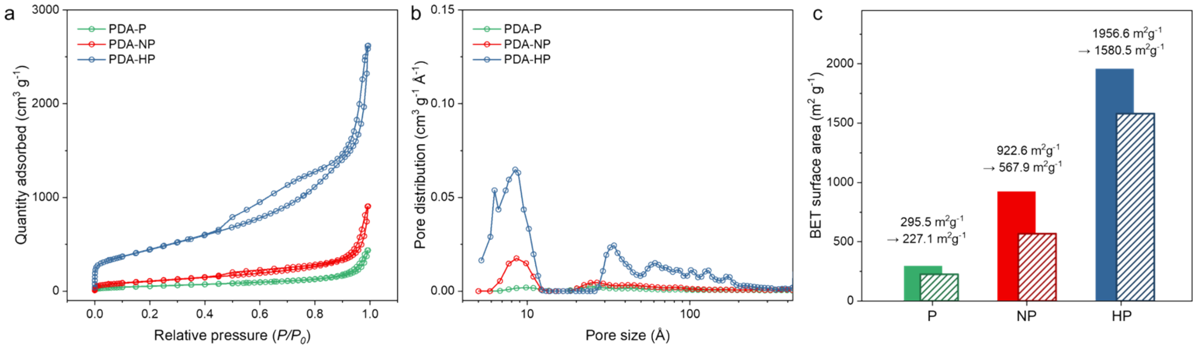

Supplementary Figure 16. BET analysis on PDA-coated carbons. (a) BET nitrogen adsorption isotherm plot and (b) pore size distribution of PDA-coated carbon support materials. (c) The surface area changes after the PDA treatment for 30 mins.

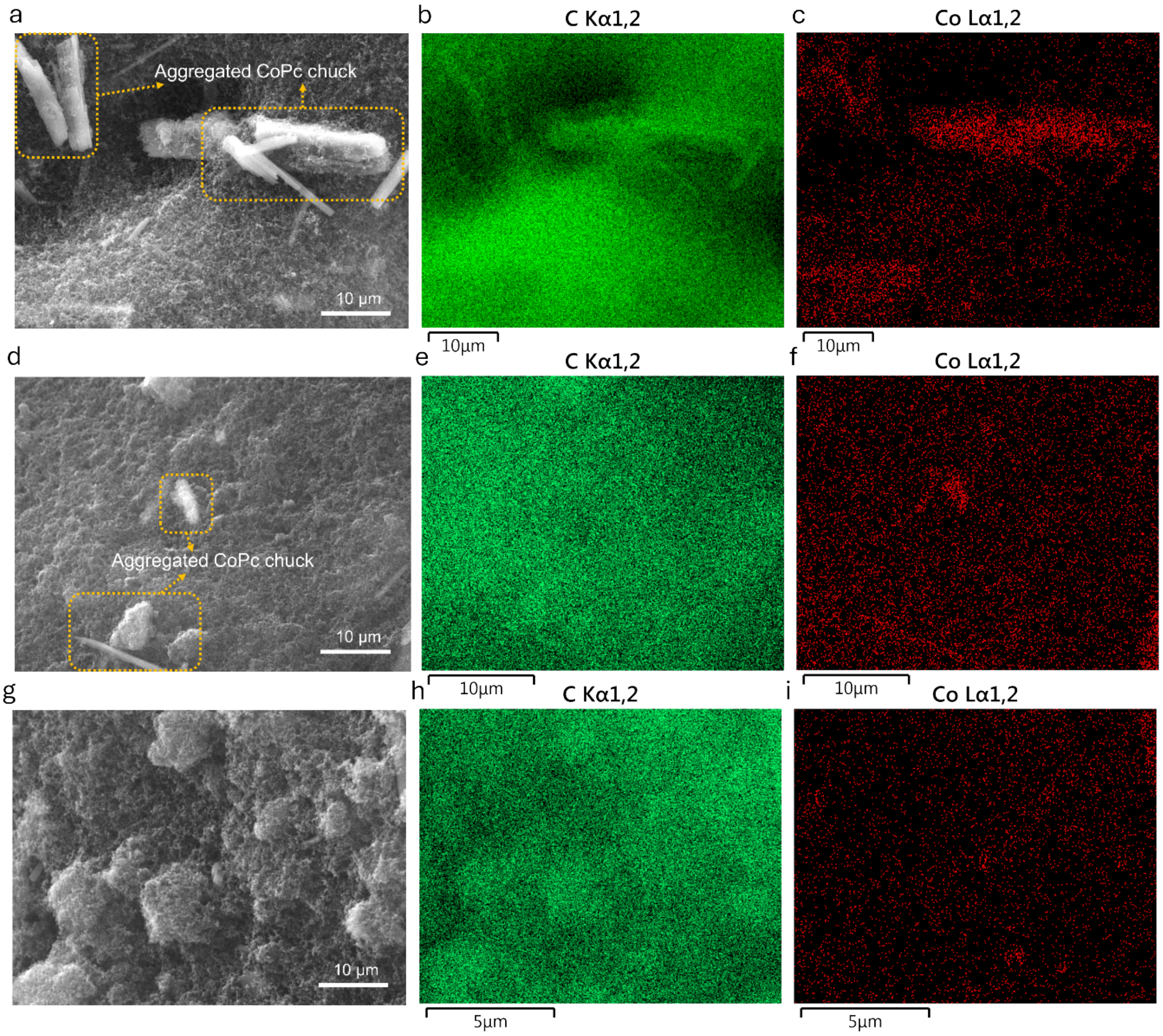

Supplementary Figure 17. SEM-EDS images of (a)-(c) CoPc/P, (d)-(f) CoPc/HP, and (g)-(i) CoPc/PDA-HP. Aggregated CoPc chuck formed in uncoated samples.

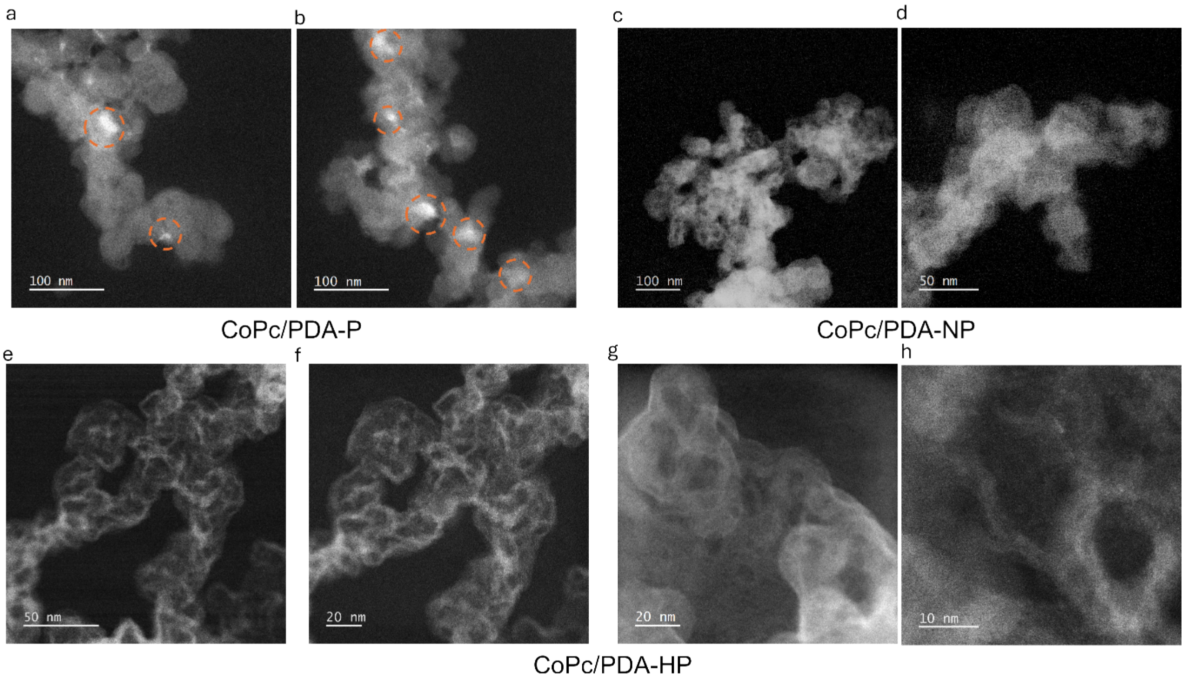

Supplementary Figure 18. HRTEM images of (a) – (b) CoPc/PDA-P, (c) – (d) CoPc/PDA-NP, and (e) – (h) CoPc/PDA-HP. Aggregation of CoPc (highlighted by circles in a and b) is observed in the CoPc/PDA-P sample.

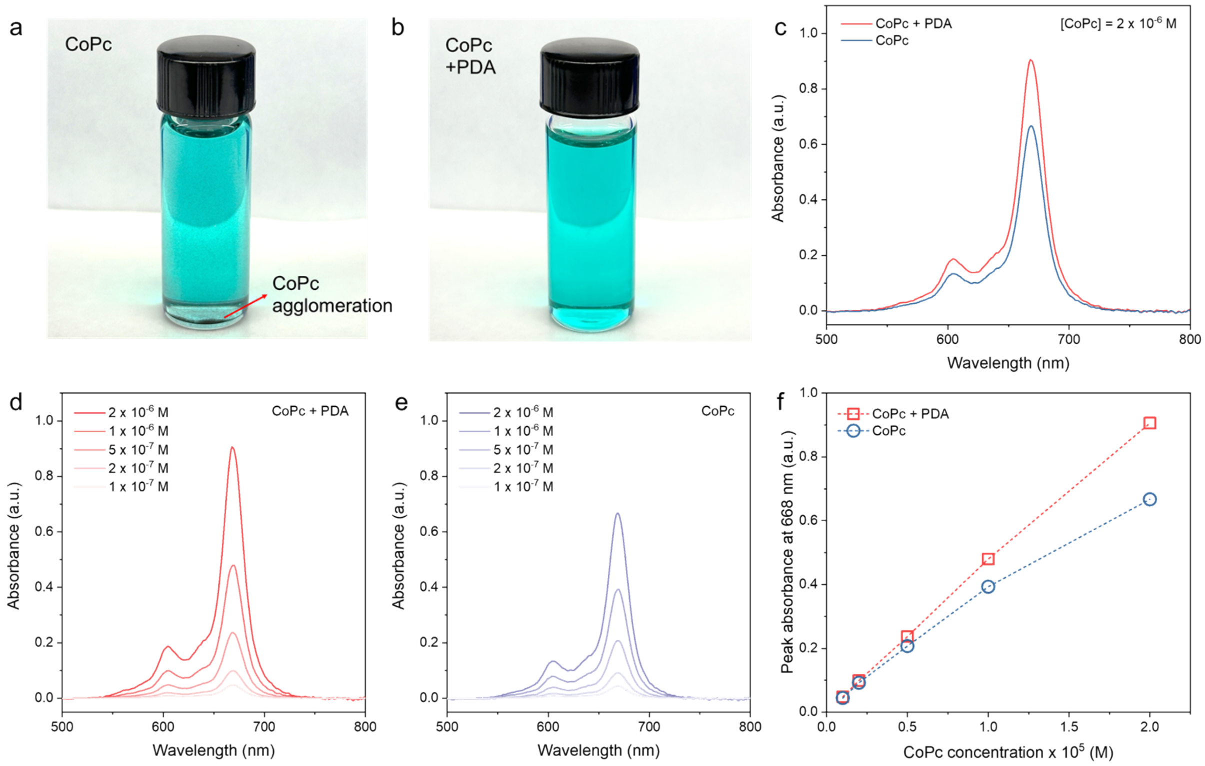

Supplementary Figure 19. UV-Vis spectroscopy analysis of CoPc dispersion. (a)-(b) Photos of CoPc dispersed in DMF solutions with and without the addition of PDA, showing significant agglomeration in the solution without PDA. (c)-(e) Representative spectra of the CoPc Q-band absorbance in DMF deposition solutions with varying CoPc concentrations, both with and without PDA. (f) Peak monomer absorbance (668 nm) for CoPc and CoPc + PDA samples prepared at different CoPc concentrations. A quasi-linear increase in peak absorbance was observed for the CoPc samples with the addition of PDA.

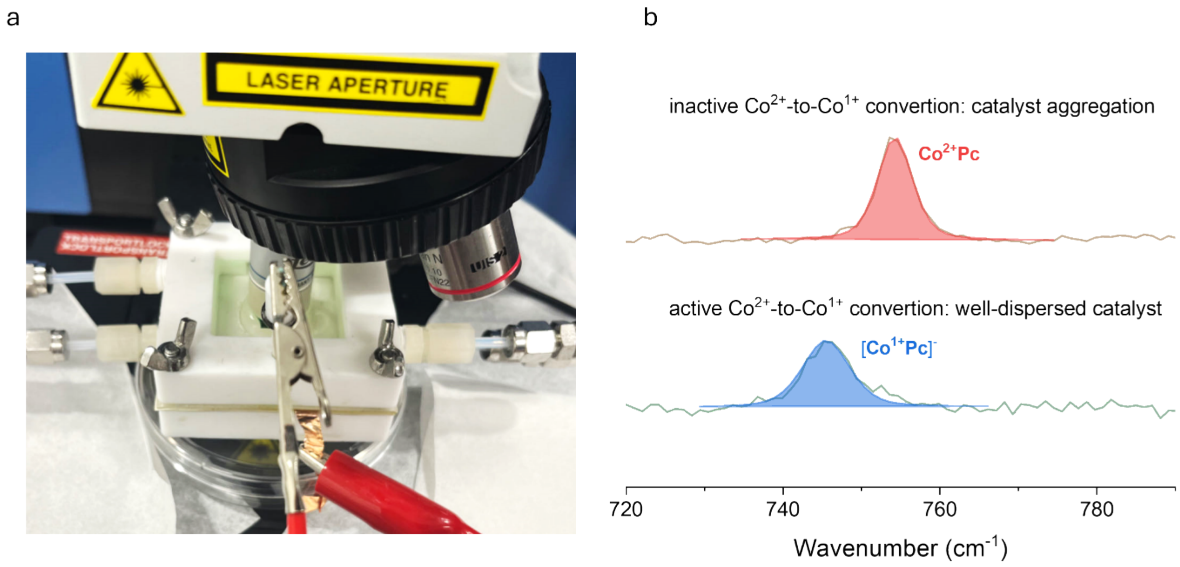

Supplementary Figure 20. In situ Raman setup for studying the dispersion mechanism. (a) Photo of the in-situ Raman cell in a three-electrode system. (b) Schematic illustration of the dispersion/aggregation mechanism, monitored by tracking changes in the Co chemical states.

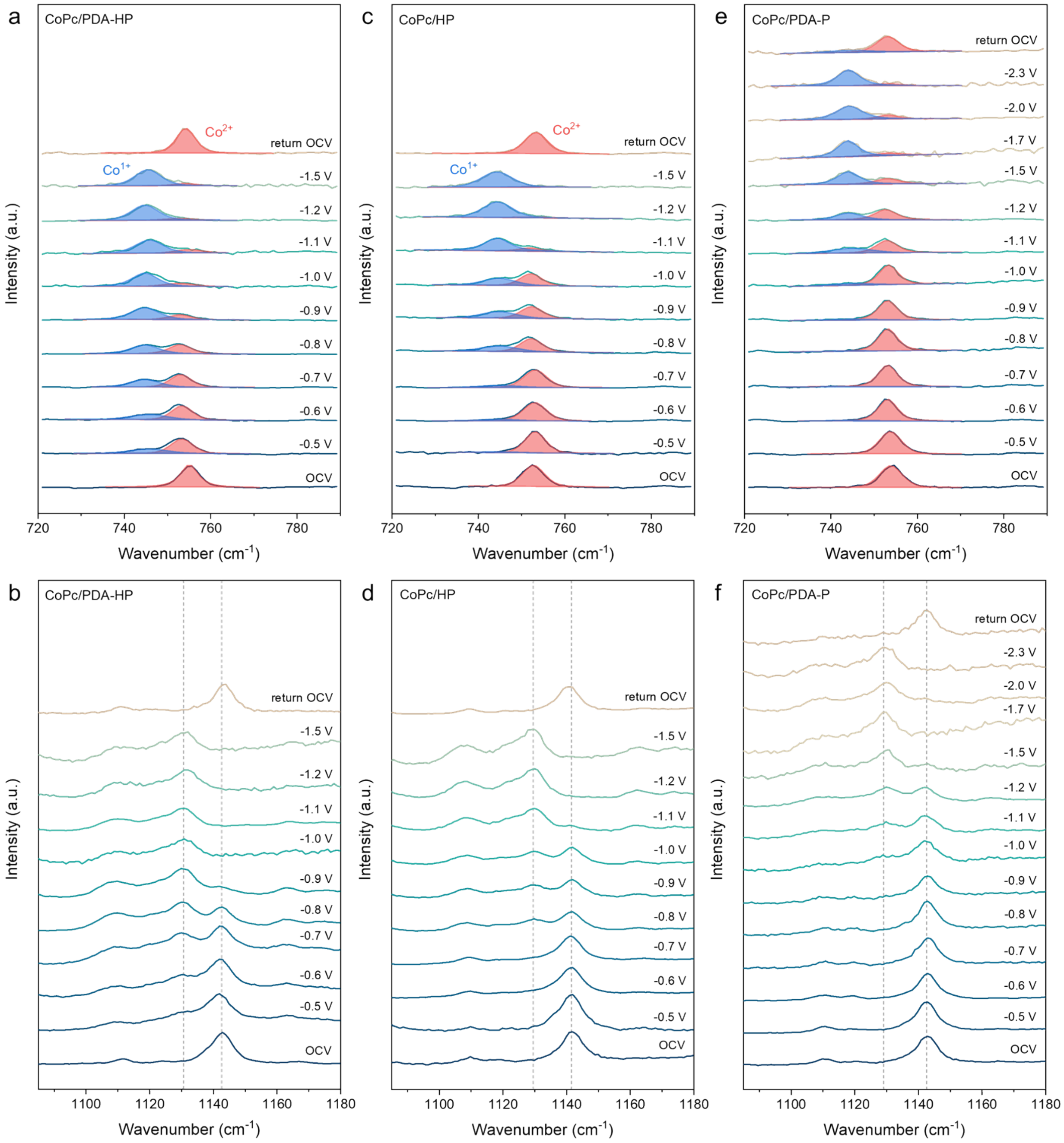

Supplementary Figure 21. *In-situ* Raman analysis on different catalysts. (a)-(b) CoPc/PDA-HP. (c)-(d) CoPc/HP. (e)-(f) CoPc/PDA-P.

In (a), (c), and (e), we summarized the inactive Co^{2+}Pc to active Co^{1+}Pc transition in the wavenumber region of 745-755 cm^{-1}.[12,13] Similar Co chemical state transition is occurred in the wavenumber region of 1128-1142 cm^{-1}, as shown in (b), (d), and (f). The results indicated that the optimal HP carbon support, combined with a PDA coating, significantly enhances the rate and extent of the Co^{2+} to Co^{1+} transition, suggesting improved dispersion of CoPc on the support.

Supplementary Note 5. Investigation of CO_2 mass transport using simulated CO_2 gas. (Supplementary Figures 22-25, Tabe 3)

Flow cell measurements at low CO_2 supply rates

In the carbonate system with low *i*-CO_2 concentrations, we investigated the mass transport behavior of various CoPc-loaded carbon supports by simulating catalytic performance in a low-concentration CO_2 gas environment. The formation of CO is highly dependent on the local [CO_2], with a high $^*CO_2$ surface coverage being a key factor in promoting CO production.[14] The first electron transfer in the CO_2-to-CO reaction is known to be the rate-determining step, which suggests that the activity would scale linearly with CO_2 concentration.

In practice, the gas-phase CO_2 concentration at the three-phase boundary can be regulated in two ways: (1) adjusting the CO_2 concentration in the feed gas by diluting it with an inert gas (e.g., N_2), and (2) controlling the CO_2 gas flow rates.

In conventional gas-phase CO_2 electrolyzers within flow cells, a continuous CO_2 supply (e.g., 30 mL/min) is typically used. However, our analysis of *i*-CO_2 concentrations in a BPM-based carbonate electrolyzer revealed that the theoretical CO_2 concentrations are significantly lower (**Supplementary Note 3 and Supplementary Figure 3-5**). For instance, at a current density of 100 mA/cm², the theoretical CO_2 supply rate is only 0.69 mL/min/cm², corresponding to just 0.52 μmol/s. When accounting for CO_2 loss during local transport, the actual CO_2 supply rate falls below 0.69 mL/min/cm². Additionally, previous simulations predicted that the CO_2 volumetric fraction would be less than 8%.[9]

To simulate these conditions, we performed experiments by adjusting both the CO_2 partial pressure and flux rates. The flow cell setup (**Supplementary Figure 22**) featured a CoPc-based cathode, a Ni foam anode, and an anion exchange membrane. Low-concentration CO_2 gas (diluted with N_2) was introduced into the flow chamber, with the total flow rate controlled at 30 sccm. The catholyte used was 1.5 M K_2CO_3, and the anolyte was 1 M KOH, while the CO_2 partial pressure (P_{CO2}) varied between 0.1 and 1 atm. The cell was operated at current densities of 100 and 200 mA/cm².

As shown in **Supplementary Figure 23,** the CoPc/P exhibited a lower FE_{CO} at high P_{CO2}, with FE dropping from > 80% when P_{CO2} > 80%, and quickly declining to below 50% when P_{CO2} fell below 20%. In contrast, CoPc on HP demonstrated a much higher FE and a slower decrease in efficiency with decreasing P_{CO2}. Moreover, PDA modification of HP led to improved FE_{CO} at low CO_2 concentrations compared to the unmodified carbon support, maintaining FE_{CO} above 80% even when P_{CO2} dropped below 20%.

Similar experiments were conducted by varying CO_2 flow rates. The FE_{CO} remained above 80% on CoPc/PDA-HP even when the CO_2 flow rate decreased to 2.5 mL/min.

MEA cell for single pass conversion of CO_2

To further investigate mass transport behavior within and across the cathode layer of CoPc-based catalysts on various porous carbon supports, we evaluated their performance in MEA-based electrolyzers for CO_2 reduction. Single pass conversion (SPC) and the stoichiometric CO_2 consumption ratio (λstoic) were used as diagnostic tools to analyze mass transport and assess catalyst performance.[15] These metrics provide insights into the efficiency of the catalyst layer in utilizing locally supplied CO_2, particularly under electrolysis conditions where CO_2 is consumed both catalytically (via CO_2-to-CO conversion) and non-catalytically (through acid-base reactions in a locally alkaline environment), leading to highly CO_2-depleted conditions. This behavior mirrors that of carbonate electrolysis systems with ultra-low CO_2 supply rates.

We first investigated the CO_2 mass transport mechanism within the MEA cell (**Supplementary Figure 24-25**). In-plane carbon transport within the catalyst layer facilitates the catalytic conversion of CO_2 to CO, while non-catalytic CO_2 consumption occurs as CO_2 reacts with OH^-, generated catalytically, to form HCO_3^- and CO_3^{2-} species within the cathode. Out-of-plane carbon transport involves the transfer of anions across the anion exchange membrane (AEM). The efficiency of in-plane carbon transport is significantly affected by the properties of the cathode catalyst.

Three scenarios illustrate possible mass transport conditions:

1. OH^- Crossover: In this scenario, only OH^- crosses the AEM, and no additional CO_2 is consumed. However, this is unlikely, as both the HER and the CO_2RR produce OH^-, which reacts with CO_2 to form CO_3^{2-} and HCO_3^-. These anions then need to cross the membrane to balance the charge.
2. CO_3^{2-} Crossover: This scenario indicates that an extra CO_2 molecule is consumed in acid-base reactions to produce CO_3^{2-}. With 100% FE_{CO}, the maximum single pass conversion (SPC) of CO_2 is 50%.
3. HCO_3^- Crossover: Here, two additional CO_2 molecules are required for the formation of HCO_3^-. At 100% FE_{CO}, the maximum SPC of CO_2 in this case is 33%.

We employed both catalytic SPC and the λstoic to compare different carbon supports and study mass transport behavior. These two parameters reflect both CO_2 utilization, FE_{CO}, and CO_2 consumption.

- **Catalytic Single Pass Conversion (SPC)**: $SPC = \frac{\dot{V}_{CO}}{\dot{V}_{CO2,in}} \times 100$

- **Stoichiometric Ratio for Total CO_2 Consumption (λstoic)**: $\lambda_{\text{stoich}} = \frac{CO_{2in}}{CO_{2\,\text{con}}}$

SPC is the ratio between outlet flow of CO and total CO_2 input flow; λ_{stoich} is the ratio between CO_2 input flow and total CO_2 consumption. A high SPC and low λ_{stoich} signify efficient CO_2 transfer and subsequent catalytic CO_2 conversion.

The electrolyte-free cathodic chamber was fed with humidified CO_2. 0.1 M $KHCO_3$ was circulated as the anolyte, with a flow rate of 20 mL/min. The cathode and anode were separated by an AEM. A N_2 bleeding line is inserted as the flow rate internal standard. The N_2 bleeding line is inserted after the reactor and in front of the GC. The actual total gas flow rate into the GC sample loop could be calculated as:

$$\dot{V}_{\text{Total}} = \dot{V}_{N_2} + \dot{V}_{\text{electrolyzer}} = \frac{\dot{V}_{N_2}}{C_{N_2}}$$

$\dot{V}_{\text{Total}}\,(mL/s)$ is the total stream flow rate to GC. $\dot{V}_{N_2}(mL/s)$ is defined as the N_2 bleeding flow rate. $\dot{V}_{\text{electrolyzer}}(mL/s)$ is the reactor product stream flow rate. $C_{N_2}(\%VOL)$ is the N_2 concentration detected by GC.

The results in **Supplementary Table 3** demonstrated over 89% FE_{CO} on CoPc/PDA-HP at current densities of up to 300 mA cm^{-2}. It exhibited a low stoichiometric CO_2 excess (λ_{stoich}) ranging from 1.3 to 1.4, with >48% of SPC at the electrolyzer exit stream. The λ_{stoich} trend across the three carbon materials was PDA-HP < HP < P, while the SPC followed the order PDA-HP > HP > P. These results highlight the enhanced local transport of CO_2 and ions (CO_3^{2-}, OH^-) and the significantly improved CO_2 utilization under CO_2-limited conditions.

The "CO_2-starved" conditions in the gas-phase CO_2 electrolyzer are primarily due to the alkaline environment generated by the catalytic reactions of HER/CO_2RR, which leads to non-catalytic acid-base CO_2 consumption. This environment closely resembles the local conditions in carbonate-based systems at high current densities. Therefore, the mass transport dynamics observed in gas-phase CO_2 electrolyzers can offer valuable insights for carbonate electrolyzers, given their similar local environments.

In summary, the results in both flow cell and MEA electrolyzer indicate that the design of porous carbon supports for loading molecular CoPc catalysts significantly improves CO_2 mass transport. This enhancement is attributed to the hierarchical structure of the carbon, featuring both mesopores and micropores. The mesopores facilitate rapid CO_2 delivery to the catalyst sites, while the micropores prolong CO_2 retention within the pores. The hierarchical structure acts as a "CO_2 reservoir" that promotes local CO_2 accumulation in CO_2-deficient environments. Furthermore, PDA modification of the carbon support ensures uniform dispersion of CoPc within the pores, preventing its aggregation under electrochemical conditions and increased the active sites availability. This improved Co active site distribution enhances the connection between CO_2 molecules and the active sites, thereby increasing CO_2 diffusion and utilization within the catalyst layer.

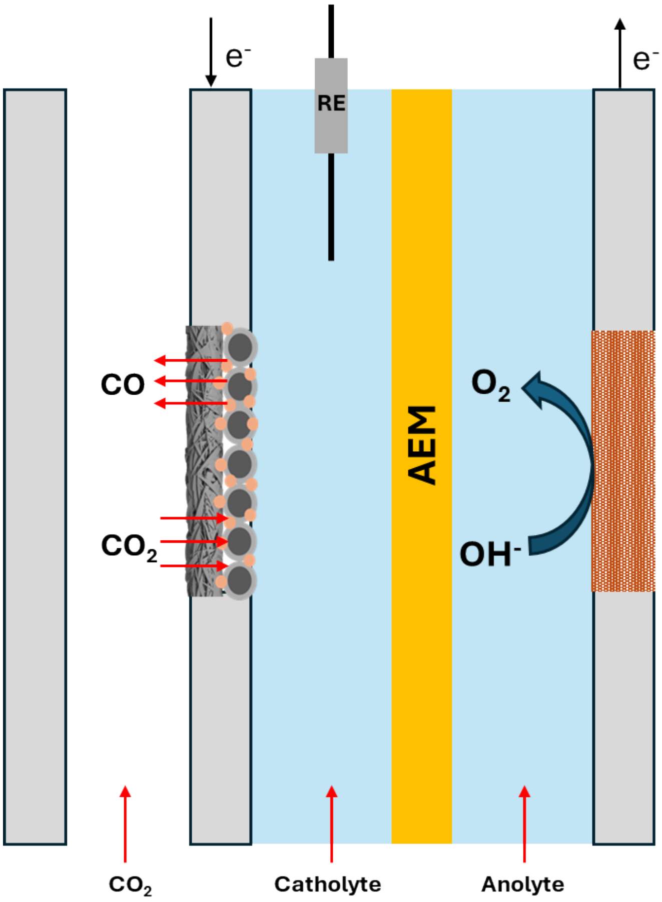

Supplementary Figure 22. Schematic illustration of flow cell set-up for gas CO_2 reduction.

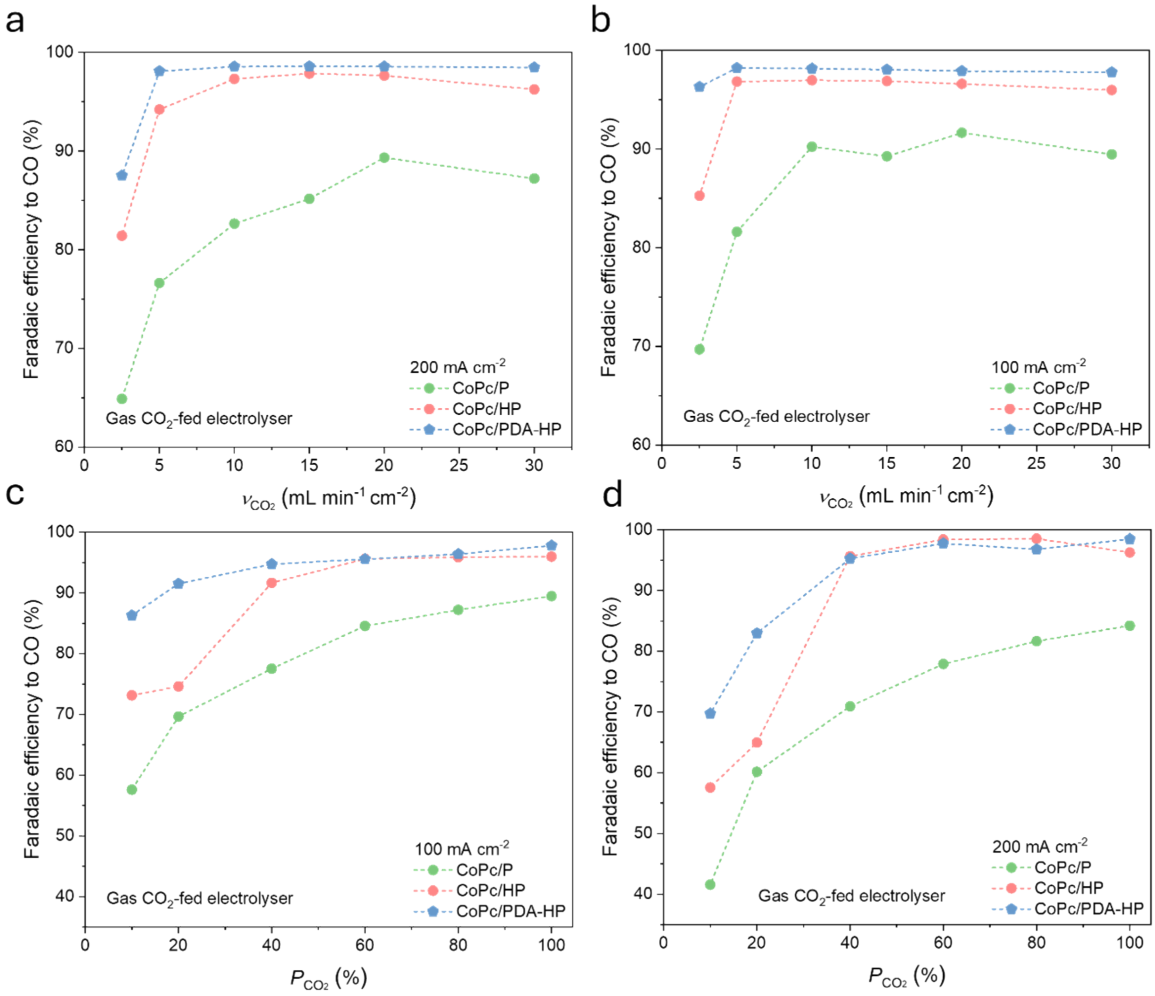

Supplementary Figure 23. Faradaic efficiency to CO for gas-CO_2-fed electrolyzer as a function of (a) – (b) CO_2 flow rate and (c) – (d) CO_2 partial pressure at 100 and 200 mA/cm^2.

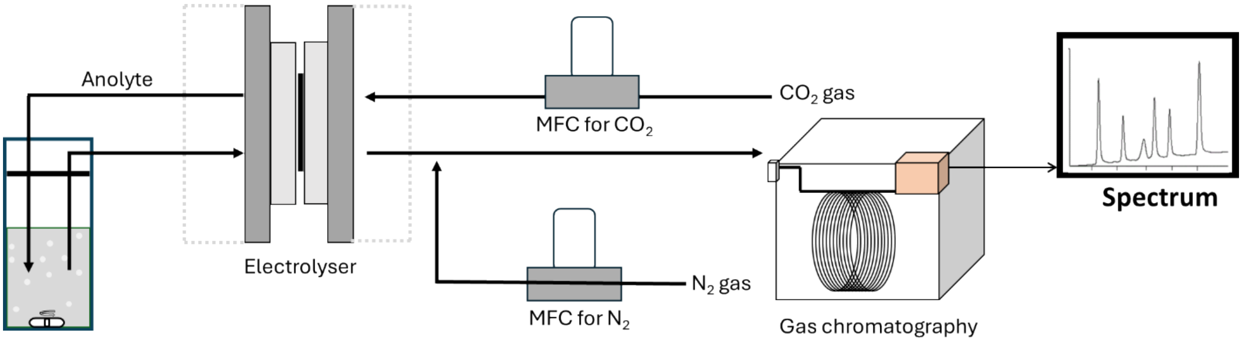

Supplementary Figure 24. Schematic illustration of CO_2 reduction in MEA-based electrolyzer. Mass flow controllers are used to regulate the flow rates of CO_2 and N_2, with N_2 serving as an internal standard.

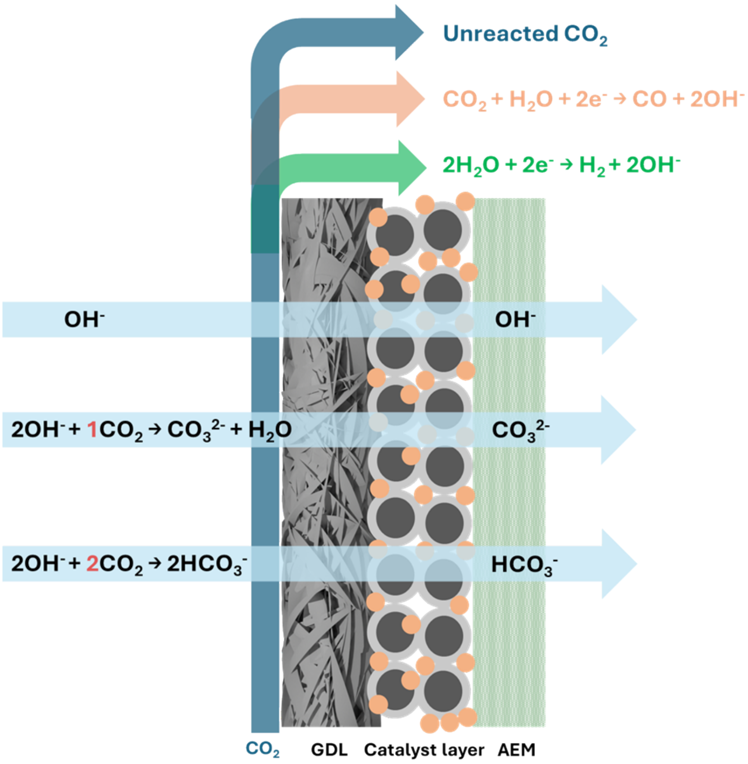

Supplementary Figure 25. Schematic illustration of local chemical environments in MEA-based CO_2 electrolyzer with AEM.

Supplementary Table 3. Summary of FE_{CO}, SPC, and λ_{stoic} for CO_2 reduction in MEA-based configuration with AEM using CoPc-based catalysts.

	FE_{CO} (%)		SPC (%)		λ_{stoich}	
Current density (mA/cm^2)	**200**	**300**	**200**	**300**	**200**	**300**
CoPc/P	56	51	28.4	26.6	2.1	2.0
CoPc/HP	69	73	35.0	38.1	1.8	1.4
CoPc/PDA-HP	94	89	47.6	48.1	1.4	1.3

Supplementary Note 6. Investigation of CO_2 mass transport using CO_2 isotherm and the heat of CO_2 adsorption

The capture, retention, and sequestration of CO_2 are generating significant interest in the fields of energy and environmental research. Carbon materials with high surface area and micropore volume offer the potential to be used for CO_2 adsorption. It is useful to consider the material surface's specific affinity for CO_2 adsorption as a factor in its ability to capture and retain CO_2. Not all carbon materials will be suitable or effective for this purpose, making it essential to determine the desired characteristics for a given application. Gas adsorption isotherms are commonly employed to elucidate the porous structures.

In this study, we collected CO_2 adsorption isotherms using a Micrometrics 3Flex surface analyzer instrument equipped with a temperature controller. To calculate the isosteric heat of CO_2 adsorption on various carbon materials, data for the full range of surface coverage (zero to saturation) was collected. The affinity of CO_2 to the various carbons was determined through measurement of the heat of CO_2 adsorption. The isosteric heat of adsorption was calculated using the Clausius-Clapeyron equation, which involves analyzing adsorption isotherms obtained at different temperatures.

$$\frac{d\ln P}{d\,T} = \frac{\Delta H_{ads}}{RT^2}$$

$$-\Delta H_{ads} = \left(-R\frac{d\ln P}{d\frac{1}{T}}\right)$$

Where $-\Delta H_{ads}$ is the heat of adsorption, R is the gas constant, ln P is the natural logarithm of pressure, T is the analysis temperature. Essentially, heat of adsorption is determined from slopes of *ln*(P) against 1/T at same adsorption quantity.

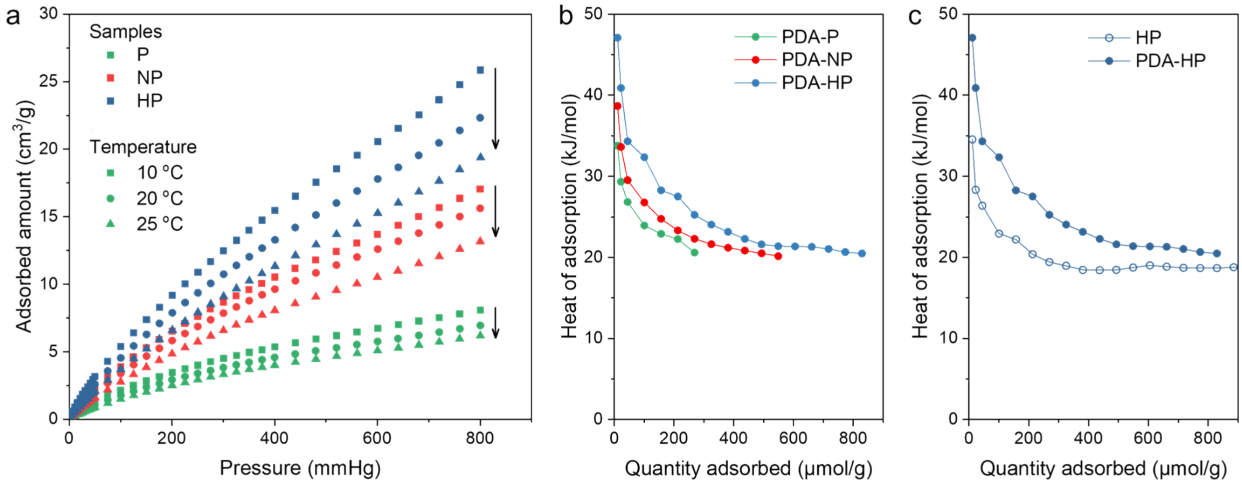

Supplementary Figure 26. CO_2 adsorption isothermal analysis. (a) CO_2 adsorption isotherms of PDA-coated carbon support at 0, 10 and 25 ^{o}C. (b) Isosteric heat of adsorption for CO_2 on PDA-coated three different porous carbons. (c) Increased isosteric heat of adsorption on micro-mesoporous carbons after PDA coating.

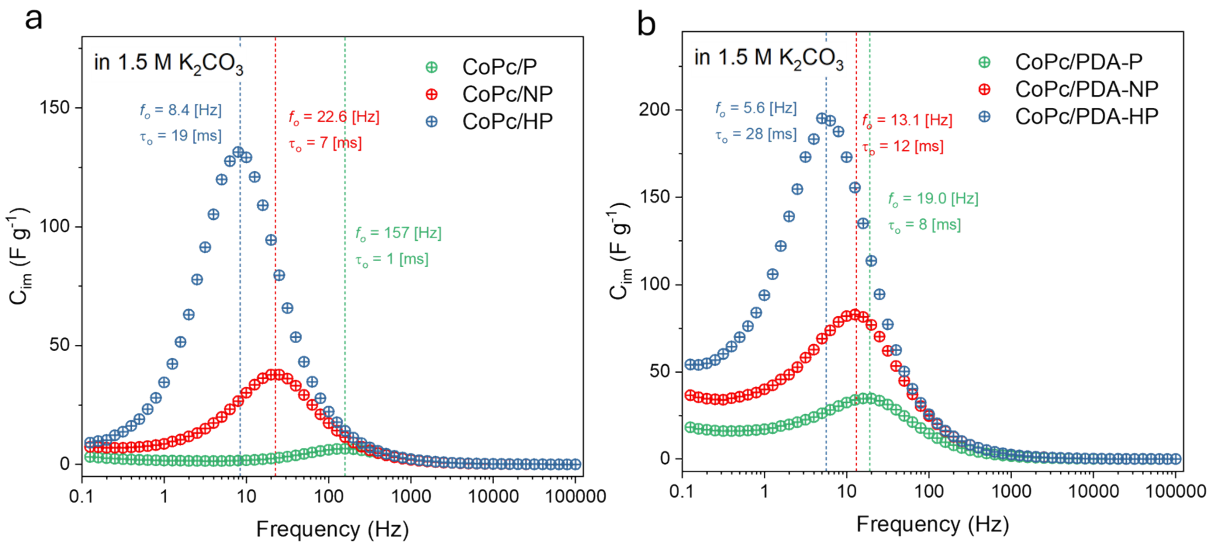

Supplementary Figure 27. EIS analysis of CoPc on various carbon supports. (a) Imaginary capacitance plots of CoPc loaded on three different carbon supports: P, NP and HP; and (b) three carbon supports with PDA: PDA-P, PDA-NP, PDA-HP. The HP used the optimum meso-to-micro ratio, the detailed optimization of HP was shown in **Supplementary Figure 49**.

The results showed that the total capacitance (C_{dl}) and the relaxation time constant (τ_o) trend in CoPc loaded on coated and uncoated carbons showed the same trend as compared to the three carbons without CoPc and PDA. Both C_{dl} and τ_o showed CoPc/HP > CoPc/NP > CoPc/P and CoPc/PDA-HP > CoPc/PDA-NP > CoPc/PDA-P.

Supplementary Note 7. Investigation of CO_3^{2-} and OH^- transport (Supplementary Figure 28-32)

In addition to *i*-CO_2 transport, the transport of ions (CO_3^{2-} and OH^-) plays a crucial role in the carbonate electrolysis system.

In the bulk electrolyte, CO_3^{2-} is supplied from the back side of the carbon paper and passes through the catalyst layer (CL) to reach the CEL/electrolyte interface. The CO_3^{2-} concentration remains consistent as it is flow-controlled.

We first conducted EIS analysis (**Supplementary Fig. 28**) to compare PDA-coated and uncoated HP carbons in both 1.5 M K_2CO_3 and 1.5 M KOH. The results showed an increased affinity between CO_3^{2-} ions and the PDA layer. Cyclic voltammetry (CV) analysis (**Supplementary Fig. 29**) further confirmed similar pseudocapacitive charge storage, driven by rapid redox interactions specifically between the PDA layer and carbonate ions. These findings suggest that within the porous carbon layer (CL), interactions between CO_3^{2-} and the PDA-carbon support occur. These optimal interactions extended CO_3^{2-} retention time, reduced local OH^- buildup, and minimized *i*-CO_2 loss, thus improving overall performance.[9]

During CO_3^{2-} transport between CL and CEL/catholyte interface, we used additional experimental data and found that CL thickness significantly impacts the ability of CO_3^{2-} to pass through the CL and reach the CEL surface (**Supplementary Figs. 30-31**). The optimal catalyst loading was determined to be 2 mg/cm^2. At higher loadings (>3.5 mg/cm^2), the CL became too dense (>85 μm thick), increasing diffusional mass transfer resistance. This dense CL blocked carbonate transport, reducing the opportunity for CO_3^{2-} to interact with H^+ and generate *i*-CO_2. Additionally, the thicker CL increased the likelihood of *i*-CO_2 being recaptured by CO_3^{2-} over its longer diffusion path.

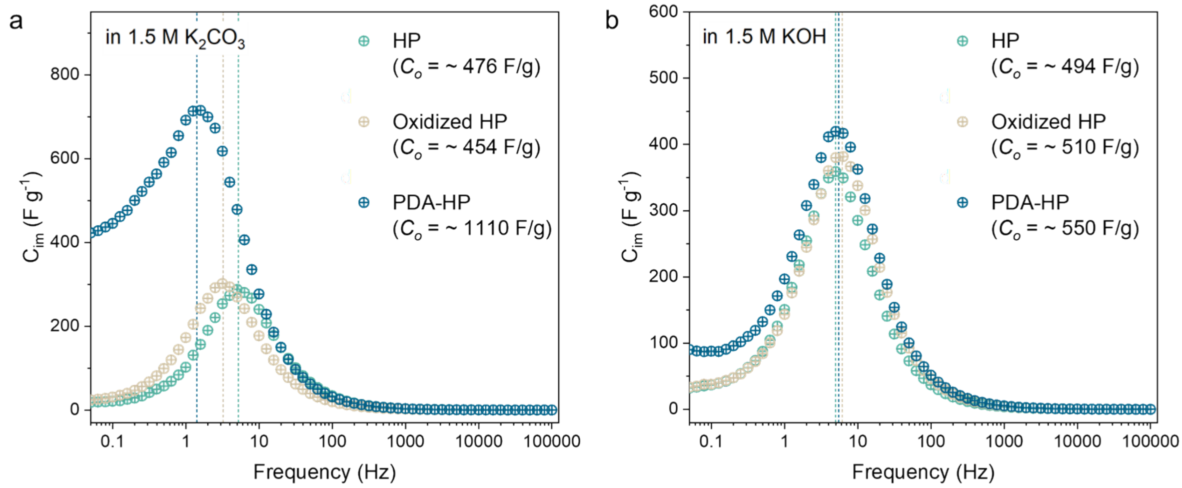

Supplementary Figure 28. EIS comparisons between carbonate and noncarbonate electrolyte. Imaginary part of complex capacitance (C_{im}) obtained by complex capacitance analysis for bare, oxidized, and PDA-coated hierarchical carbons through EIS method in (a) 1.5 M K_2CO_3 (carbonate electrolyte), and (b) 1.5 M KOH (noncarbonate electrolyte).

The PDA layers induce a significantly higher apparent capacitance (C_{dl}) in electrolytes with carbonate anions compared to those with hydroxide anions (in non-carbonate electrolytes). This observation suggests pseudocapacitive charge storage through rapid redox interactions exclusively between the PDA layer and carbonate ions, highlighting an increased affinity between them. Furthermore, in the carbonate electrolysis environment, carbonate ions hinder the approach of OH^- ions to the cathode layer, helping to reduce *i*-CO_2 loss.

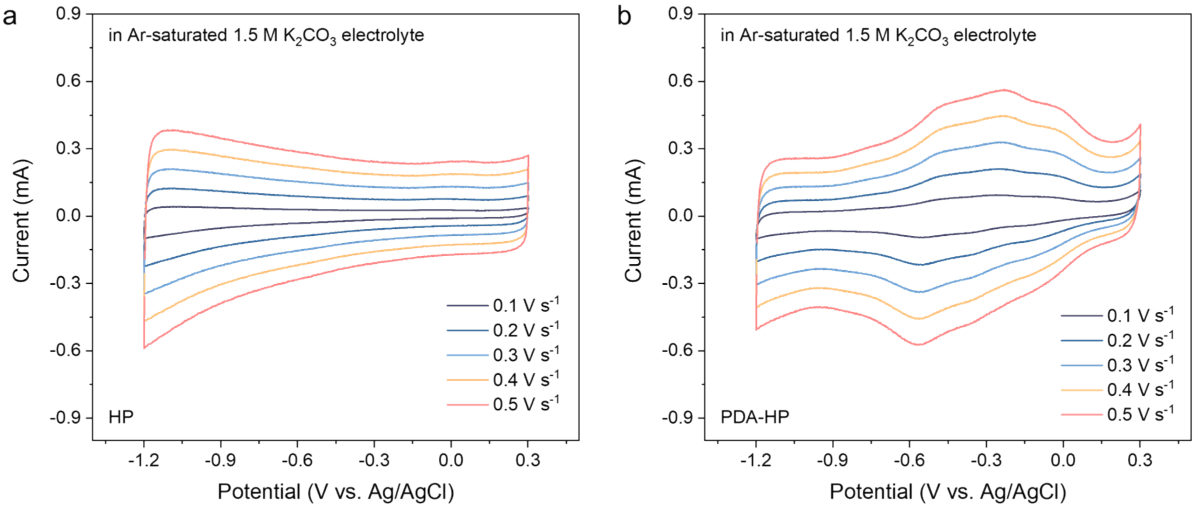

Supplementary Figure 29. Cyclic voltammetry measurements performed in Ar-saturated aqueous 1.5 M K_2CO_3 using scan-rate dependent voltammetry for (a) HP and (b) PDA-HP

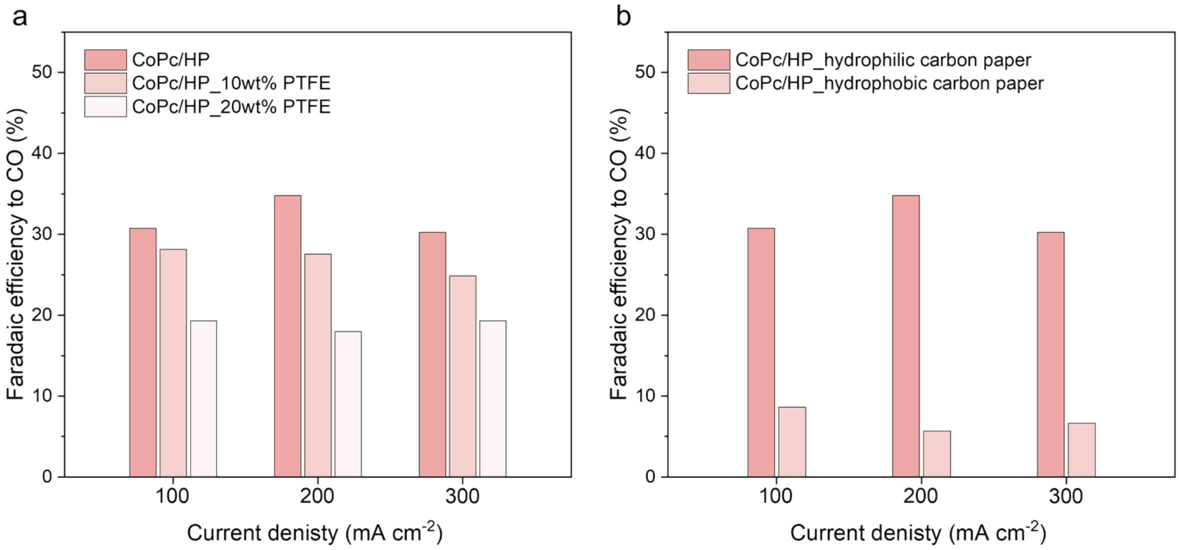

Supplementary Figure 30. Hydrophilicity/hydrophobicity effect for carbonate reduction performance. Faradaic efficiency to CO for catalyst inks with and without the hydrophobic PTFE ionomer. Comparison of Faradaic efficiency to CO for catalysts on hydrophilic (Freudenberg H23) versus hydrophobic (Freudenberg H23C3) carbon papers. We used the optimum catalyst loading of 2 mg/cm^2 (CoPc + carbon). The catalyst contains 40 wt% carbon by mass.

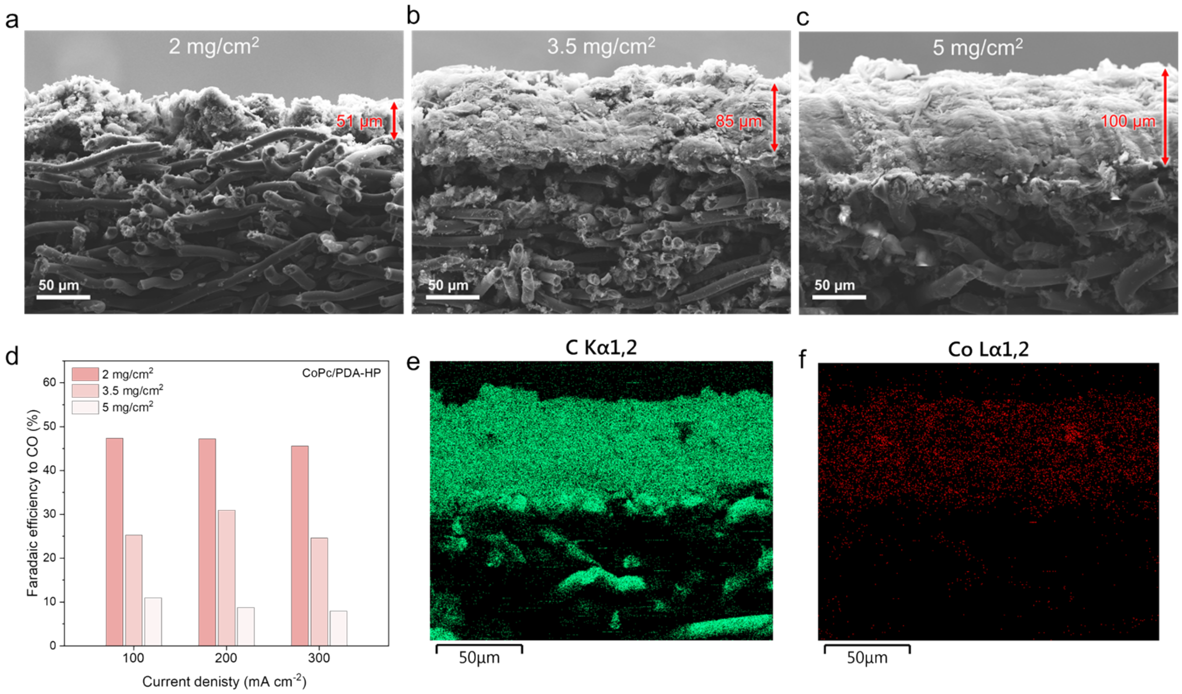

Supplementary Figure 31. Effect of catalyst thickness on carbonate electrolysis in an MEA-based system. Cross-sectional SEM images of CoPc/PDA-HP catalysts with different loadings: (a) 2 mg/cm², (b) 3.5 mg/cm², and (c) 5 mg/cm². The CoPc content in the catalyst is 40 wt%. (d) Faradaic efficiency to CO for the three catalyst loadings. (e)-(f) EDS images of the CoPc/PDA-HP catalyst with a 5 mg/cm² loading.

OH$^-$ distribution in various carbon supports:

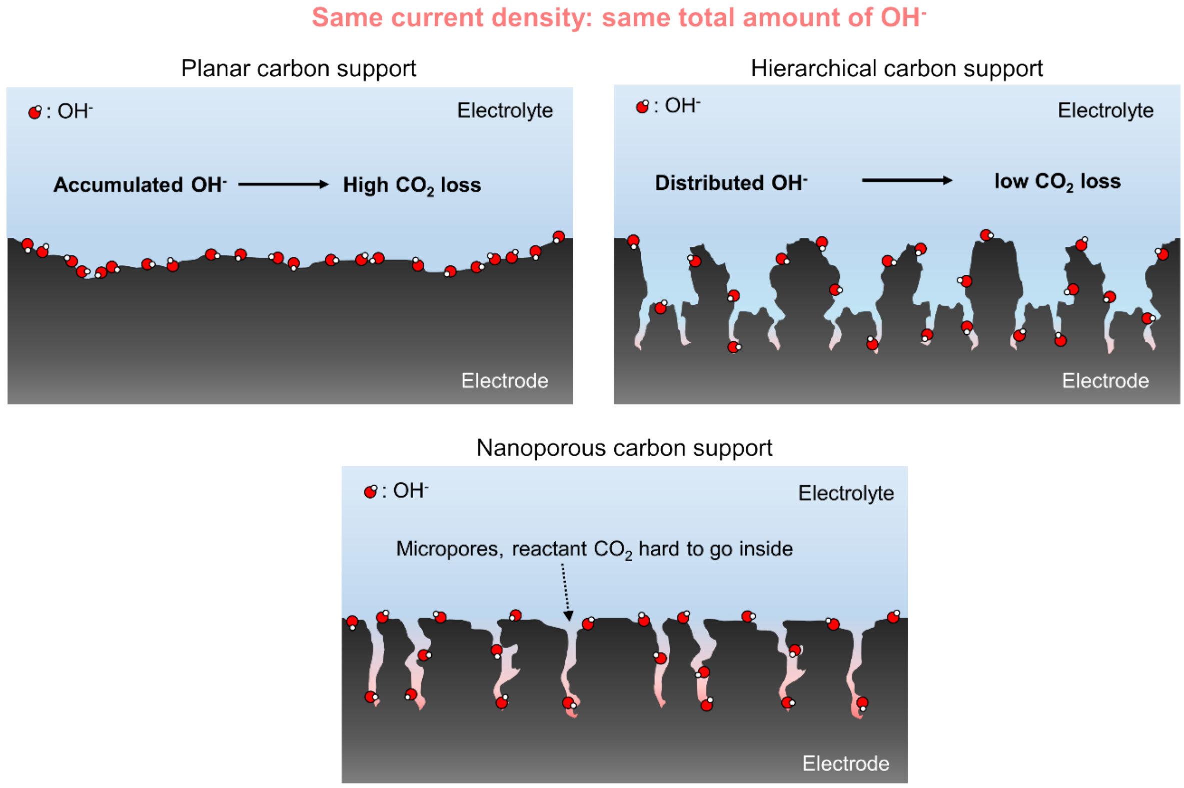

Supplementary Figure 32. Schematic illustration of OH$^-$ distribution on various carbon supports.

Under open-circuit potential (OCP) conditions, the OH$^-$ concentration corresponds to the pH of the pure carbonate system, which is approximately 12, indicating an OH$^-$ concentration of 0.01 M.

During electrolysis, OH$^-$ concentration increased at the cathode layer (CL). Under constant current density, which maintains a steady OH$^-$ production rate (mol/s), a comparison between planar carbon and hierarchical carbon revealed that the OH$^-$ production rate normalized to electrochemically active surface area (mol m^{-2} s^{-1}) was lower for hierarchical carbon, helping to mitigate i-CO_2 loss in the cathode layer. In nanoporous carbon, although OH$^-$ is also well-distributed and diluted across the entire cathode layer, the significant barrier to i-CO_2 transport into the pores limited performance on this type of carbon support.

The uniform distribution of CoPc molecules, efficient diffusion of i-CO_2 and carbonate ions, and even spread of OH$^-$ (as illustrated in **Supplementary Fig. 32**) were all crucial in enhancing CO_2 transport and utilization.

Supplementary Note 8. Comparison between HP and NP

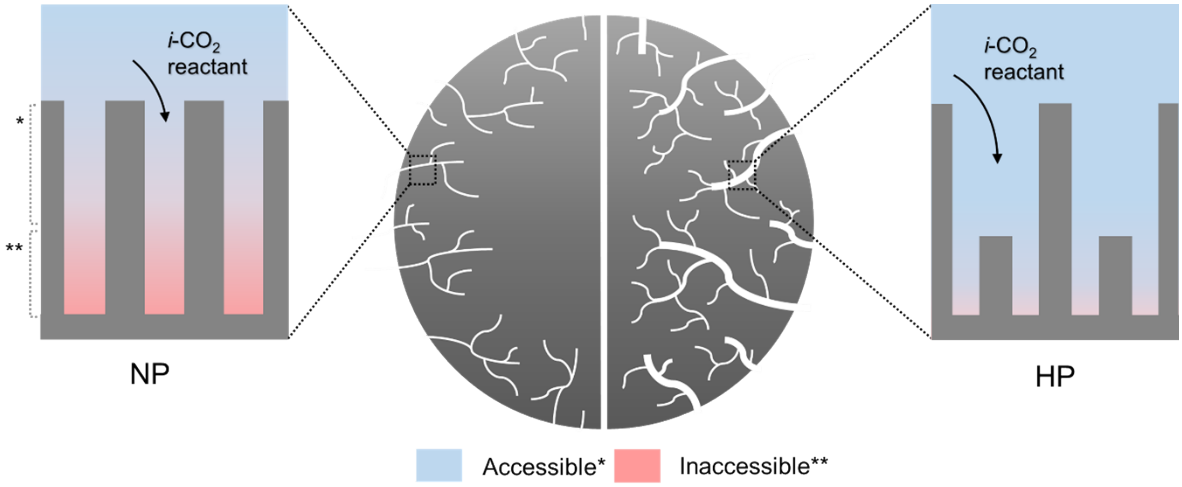

Supplementary Figure 33. Schematic illustration of morphological differences between nanoporous (NP) carbon and hierarchical porous (HP) carbon.

In a hierarchical structure used as a CoPc support, the interconnected mesopores and micropores enhance local CO_2 and electrolyte transport. The mesopores between the micropores serve as reservoirs, while the ordered mesoporous structure significantly aids in forming the electrode/electrolyte interface by improving electrolyte wetting within the micropores.[11,16]

Micropores typically have small openings (1-4 nm) and can be tortuous. When a structure is dominated only by micropores without mesopores, the long diffusion paths through the micropore channels create significant kinetic barriers to mass transport.[17] This means that without mesopores, reactants and electrolytes struggle to reach the active sites located deep within the micropores, leaving it electrochemically inactive.

In new experimental results, we further modified NP carbon through CO_2 activation and coated it with PDA, increasing both the micropore fraction and total surface area (**Supplementary Fig. 34**) compared to the pristine PDA-NP. However, the lack of significant mesopores resulted in up to a 12% decrease in FE_{CO} during carbonate electrolysis at current densities of 100-400 mA/cm^2.

To investigate further, we controlled for similar BET surface areas and compared CO_2-activated PDA-NP (micropore-rich) with PDA-HP (mesopore-rich) (**Supplementary Fig. 35**). At comparable BET surface areas of 1151 and 1226 m^2/g, CoPc/PDA-HP consistently showed a higher FE_{CO} than CoPc/PDA-NP-CO_2, with differences of up to 20% in FE_{CO} for carbonate electrolysis at 100-400 mA/cm^2.

Finally, we normalized the CoPc/(Cdl/BET) ratio to test three different PDA-carbon materials (**Supplementary Fig. 36**). The CO production trend remained consistent with the results shown in

Figure 4a, where the same amount of CoPc was used. This suggests that the CoPc concentration had already reached saturation, and further increases in CoPc content did not enhance reaction activity.

These results indicate that simply increasing the concentration of active sites and surface area is insufficient to improve catalytic performance. Instead, optimizing the carbon support structure to enhance CO_2 transport, along with better dispersion and utilization of active sites, is more critical for boosting activity.

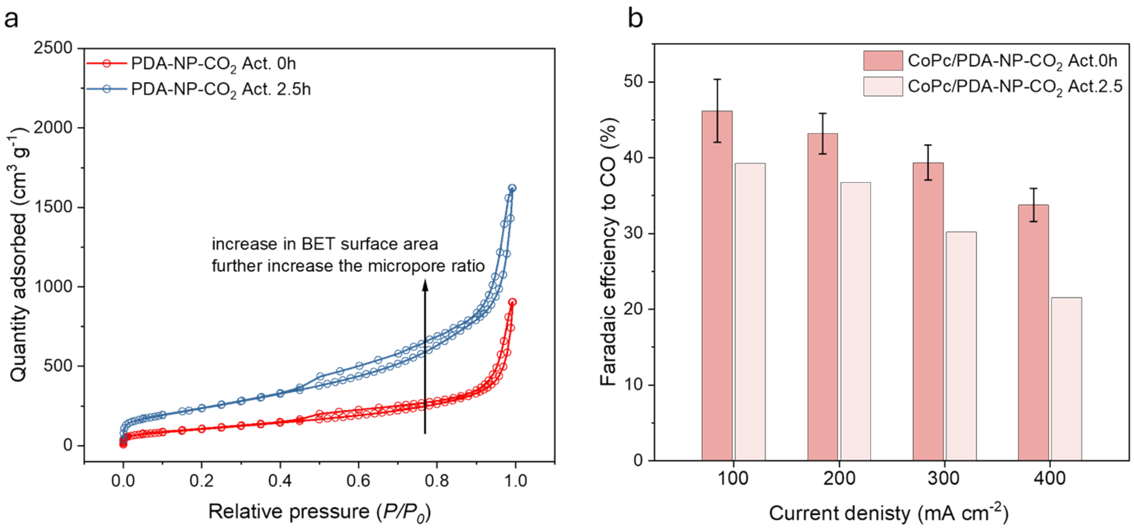

Supplementary Figure 34. Investigation of NP. (a) BET nitrogen adsorption isotherm plot and (b) Faradaic efficiency to CO on PDA-NP. We compared pristine NP coated with PDA (without CO_2 activation) to CO_2-activated NP coated with PDA. The CO_2 activation significantly increased the BET surface area and enhanced the micropore ratio. We used the optimum catalyst loading of 2 mg/cm^2 (CoPc + carbon). The catalyst contains 40 wt% carbon by mass.

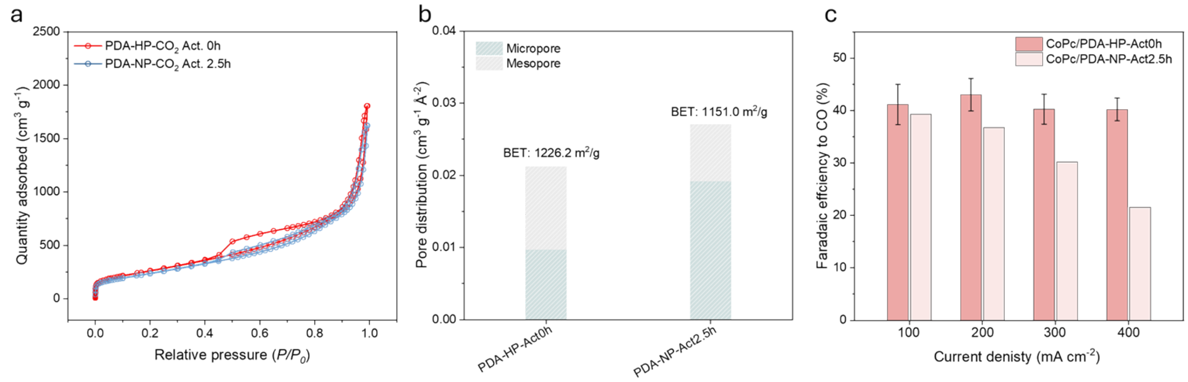

Supplementary Figure 35. Comparison of PDA-HP and PDA-NP with similar BET area. (a) BET nitrogen adsorption isotherm plot and (b) pore volume distribution, and (c) Faradaic efficiency to CO on PDA-HP and PDA-NP. We compared pristine HP coated with PDA (without CO_2 activation) to CO_2-activated NP coated with PDA. Although these two samples exhibited similar BET surface areas, they differed in their dominant pore structures. We used the optimum catalyst loading of 2 mg/cm^2 (CoPc + carbon). The catalyst contains 40 wt% carbon by mass.

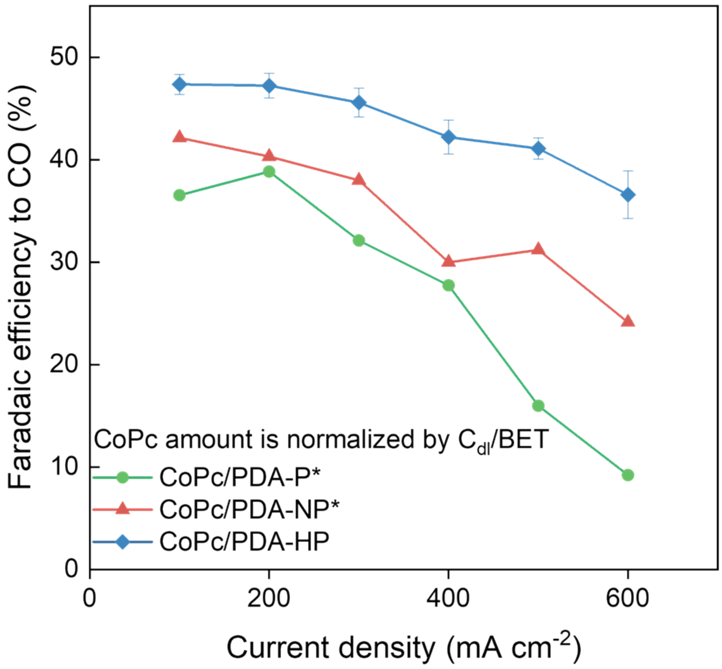

Supplementary Figure 36. Comparison of carbonate electrolysis performance with C$_{dl}$/BET normalized CoPc amount. The Faradaic efficiency for CO was measured on various CoPc/PDA-carbon materials, with the CoPc amount normalized by the C$_{dl}$/BET ratio. We used the optimum catalyst loading of 2 mg/cm^2 (CoPc + carbon).

$$\text{CoPc amount in PDA-NP} = \frac{Cdl/BET\ (PDA-HP)}{Cdl/BET\ (PDA-NP)} \times \text{ CoPc amount in PDA-HP}$$

$$\text{CoPc amount in PDA-P} = \frac{Cdl/BET\ (PDA-HP)}{Cdl/BET\ (PDA-P)} \times \text{ CoPc amount in PDA-HP}$$

We fixed the CoPc/(Cdl/BET) ratio in three carbon supports, and normalized and increased the CoPc amounts for PDA-NP and PDA-P supports. We denoted the normalized catalysts as CoPc/PDA-NP* and CoPc/PDA-P*.

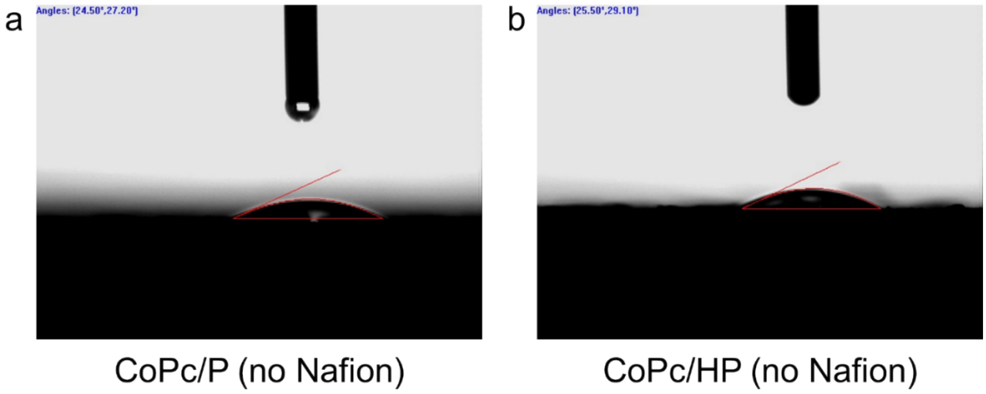

CoPc/P (no Nafion)

CoPc/HP (no Nafion)

Supplementary Figure 37. Contact angle measurements for CoPc-based GDE. (a) CoPc/P and (b) CoPc/HP on carbon paper without a Nafion binder. Ultra hydrophilic property of electrode was observed. Although untreated carbon is hydrophobic, the CoPc molecules are hydrophilic. Without the addition of Nafion, the GDE displayed the hydrophilic characteristics of CoPc.

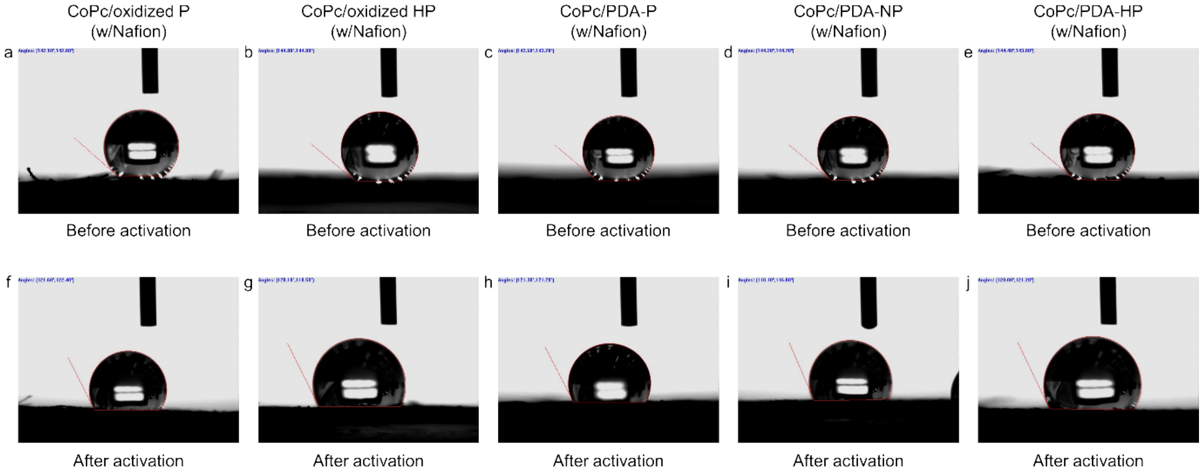

Supplementary Figure 38. Contact angle measurements for CoPc-based GDE. (a) CoPc/oxidized-P, (b) CoPc/oxidized-HP, (c) CoPc/PDA-P, CoPc/PDA-NP, and CoPc/PDA-HP on carbon paper with a Nafion binder. (f)-(g) show the contact angles of the GDEs after 5 minutes of electroreductive activation in a carbonate system at a current density of 100 mA/cm². The slight hydrophobicity is attributed to the presence of the Nafion binder in the GDE, while enhanced hydrophilic properties were observed under electrolysis conditions. Nafion is commonly used as a binder in aqueous electrolysis systems to prevent the physical detachment of catalysts from the substrate.

Nafion is primarily hydrophilic due to its sulfonic acid groups, which attract water molecules and allow for proton conductivity. However, the polymer backbone of Nafion is hydrophobic. This duality means that Nafion has both hydrophobic and hydrophilic properties, with the hydrophilic domains forming channels that facilitate ion transport.

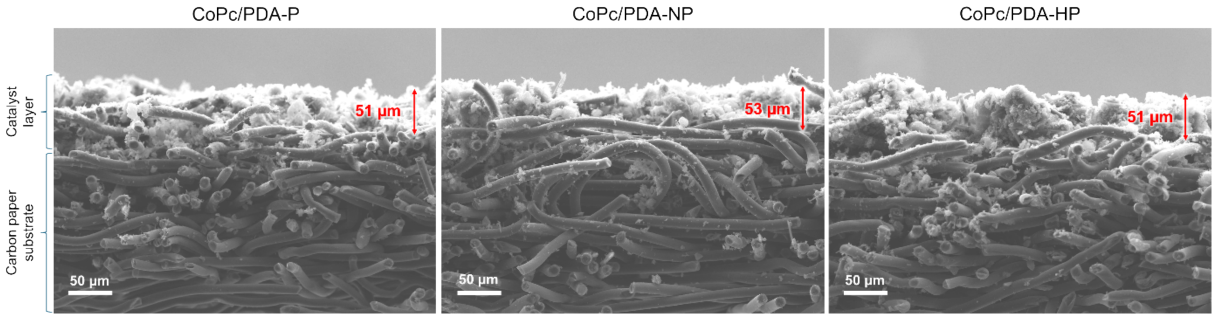

Supplementary Figure 39. Cross sectional SEM images of CoPc/PDA-carbons on carbon paper substrate. We used the optimum catalyst loading of 2 mg/cm^2 (CoPc + carbon). The catalyst contains 40 wt% carbon by mass. We observed a consistent thickness of 51-53 µm, indicating that thickness variations among the samples can be ruled out as a factor for the differences in FE$_{CO}$.

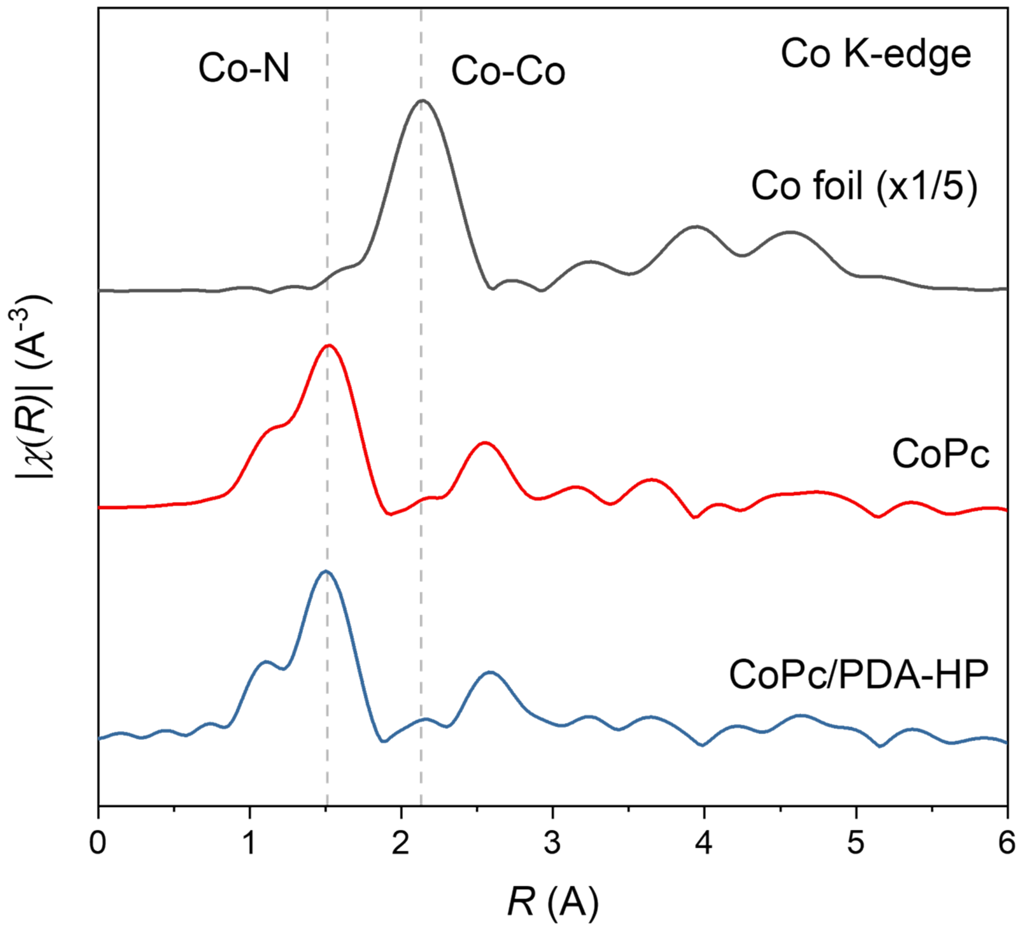

Supplementary Figure 40. EXAFS spectra in the Co K-edge spectrum for the as-synthesized samples.

In all cases we observe a pre-edge peak at 7715 eV that is characteristic of square-planar Co-N_4 in CoPc; EXAFS shows that the Co-N_4 remained intact on PDA-HP.

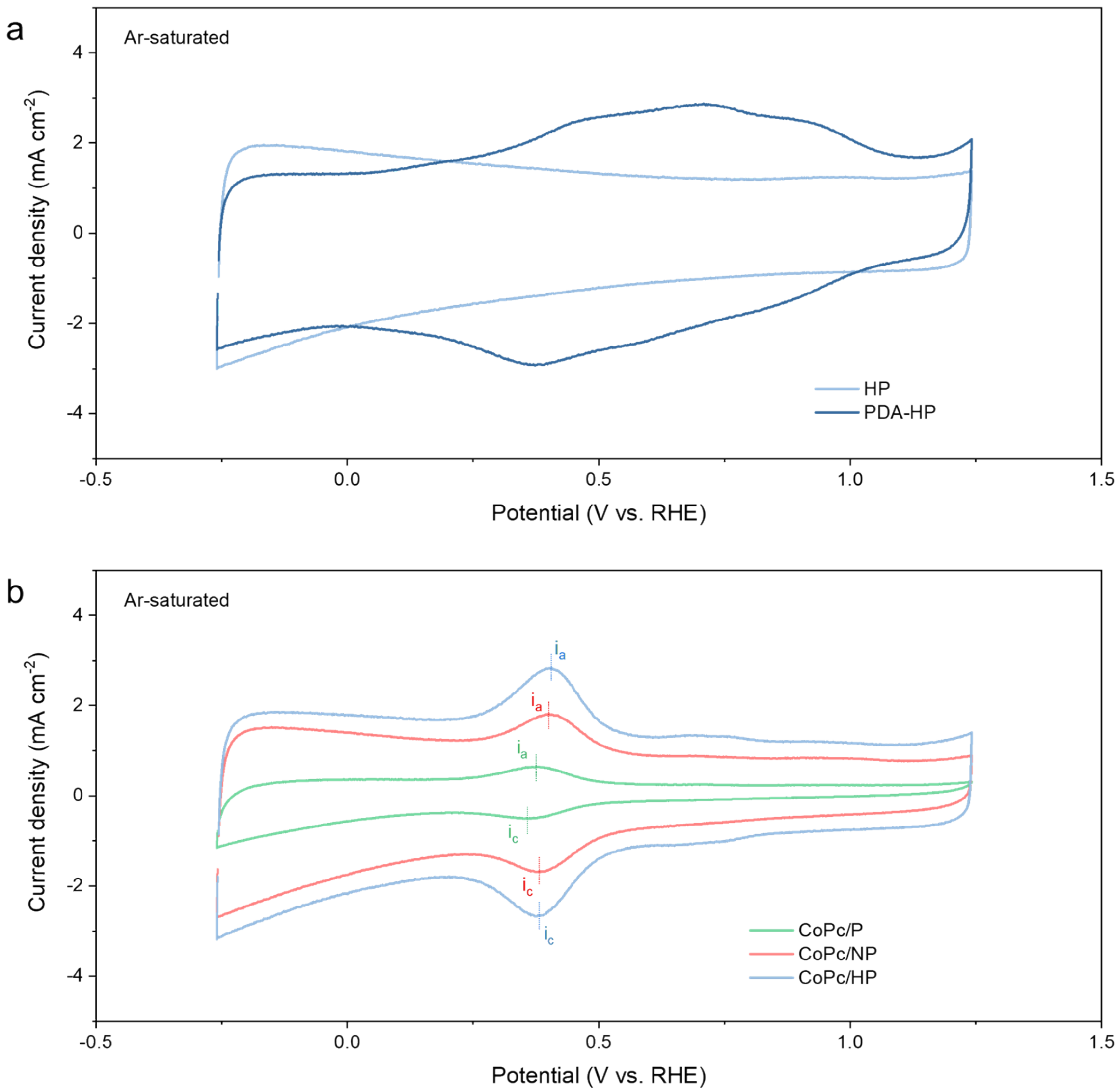

Supplementary Figure 41. CV analysis on different catalysts in Ar-saturated K_2CO_3 solution. In (a), the peaks at ~0.45 V_{RHE} and 0.95 V_{RHE} correspond to the redox peak of PDA.

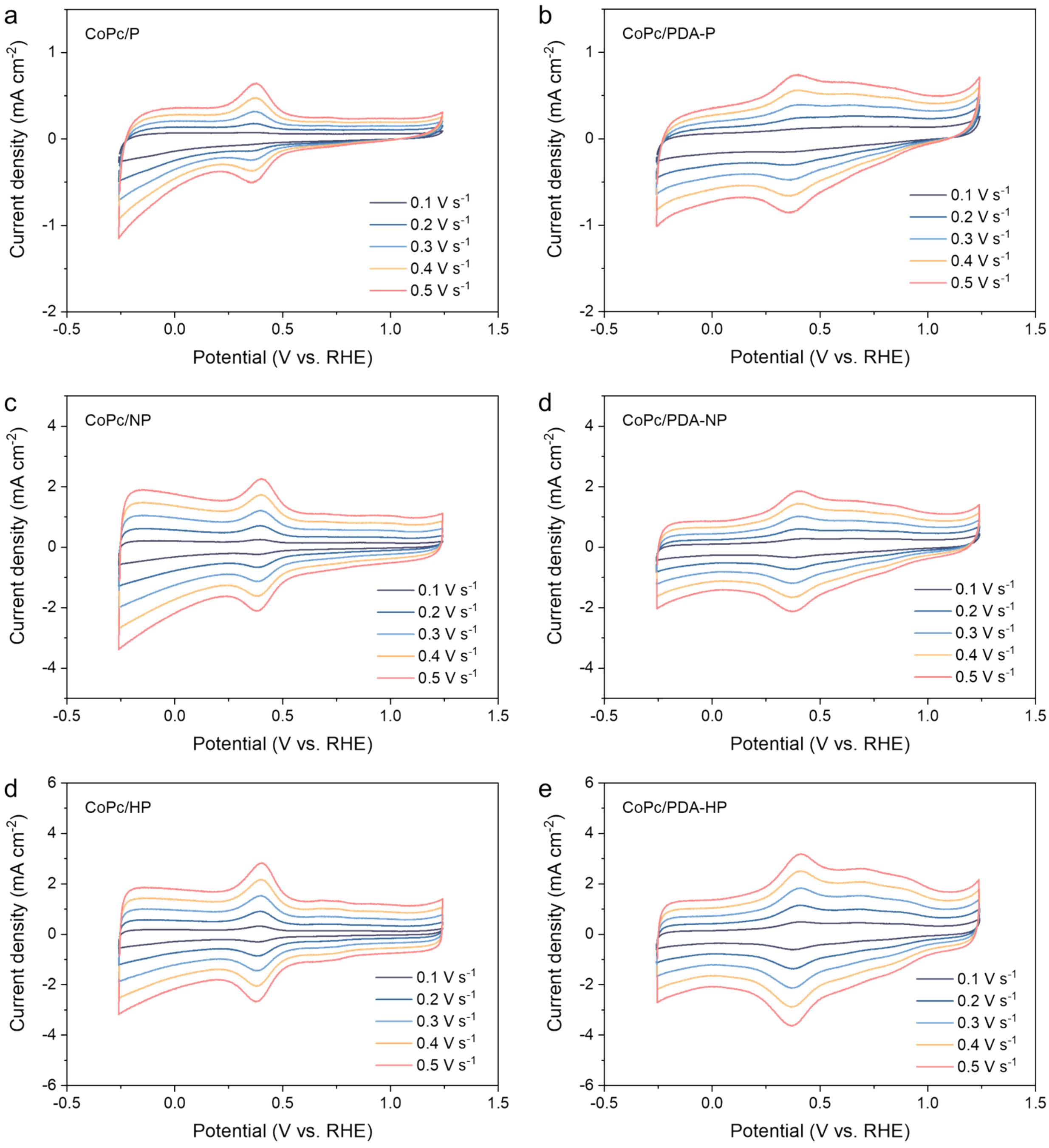

Supplementary Figure 42. CV analysis under the Ar-saturated 1.5 M K_2CO_3 conditions. CV results of (a) CoPc/P, (b) CoPc/PDA-P, (c) CoPc/NP, (d) CoPc/PDA-NP, (e) CoPc/HP, and (f) CoPc/PDA-HP with a scan rate ranging from 100 to 500 mV s^{-1}.

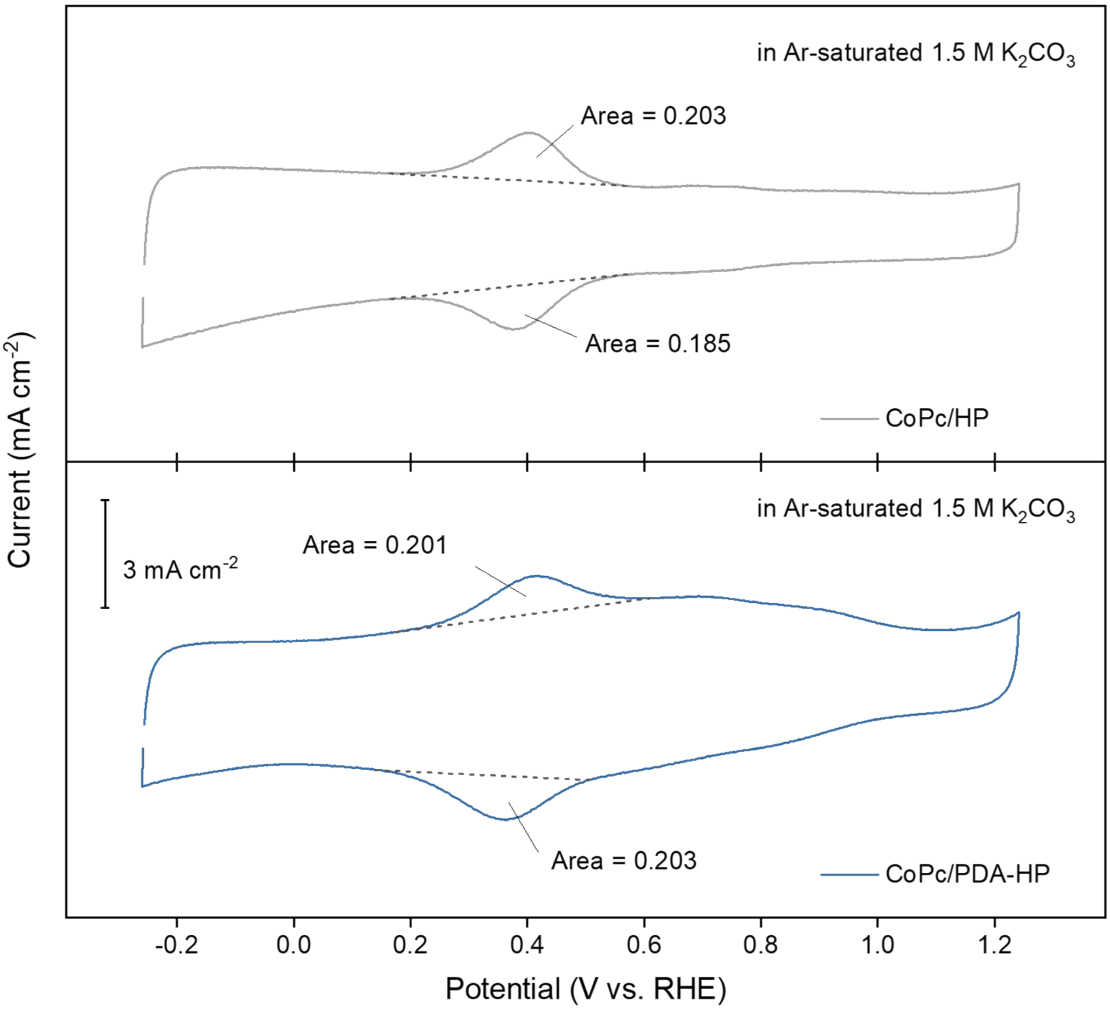

Supplementary Figure 43. CV analysis of Co redox peak. Co redox peak CV curves were recorded for CoPc/HP and CoPc/PDA-HP in an Ar-saturated 1.5 M K_2CO_3 electrolyte at a scan rate of 0.5 V s^{-1}. We calculated the Co site densities for each sample based on the area of the Co redox peak (Co^{2+}/Co^{1+} redox couple) at approximately 0.4 V.

The peak separation seen in voltammetry (~ 25 mV) was relatively constant as a function of scan rate and for the different supports (**Supplementary Fig. 42-43**), indicating fast kinetics for CoPc oxidation/reduction, even in the presence of the PDA. From the Co redox behavior in the CV, we were able to obtain insights into the electronic state of the cobalt sites in different reaction environments, such as P, NP, and HP, as shown in **Figure 3b**.

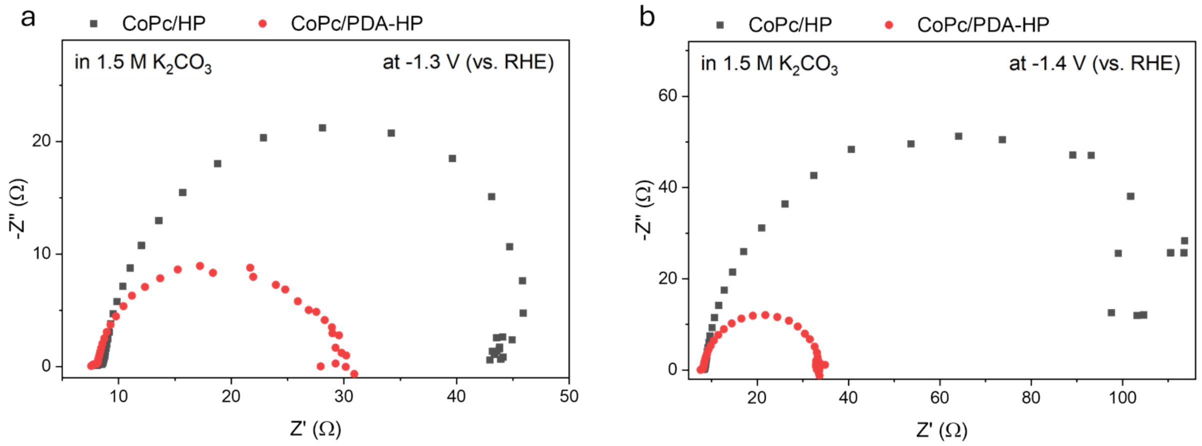

Supplementary Figure 44. EIS analysis at faradaic region. EIS test of charge transfer resistance for CoPc/HP and CoPc/PDA-HP at faradaic region at (a) -1.3 V_{RHE} and (b) -1.4 V_{RHE}.

The results demonstrated that coating the carbon support with PDA improved charge transfer between the electrode (CoPc + carbon) and the solution-phase reactants. We observed that shifting the potential negatively further reduced charge transfer resistance in CoPc/PDA-HP, while CoPc/HP exhibited an opposite trend. This may be because, at more negative potentials, CoPc on HP without PDA more readily aggregates. The non-conductive nature of aggregated CoPc subsequently increases charge transfer resistance.

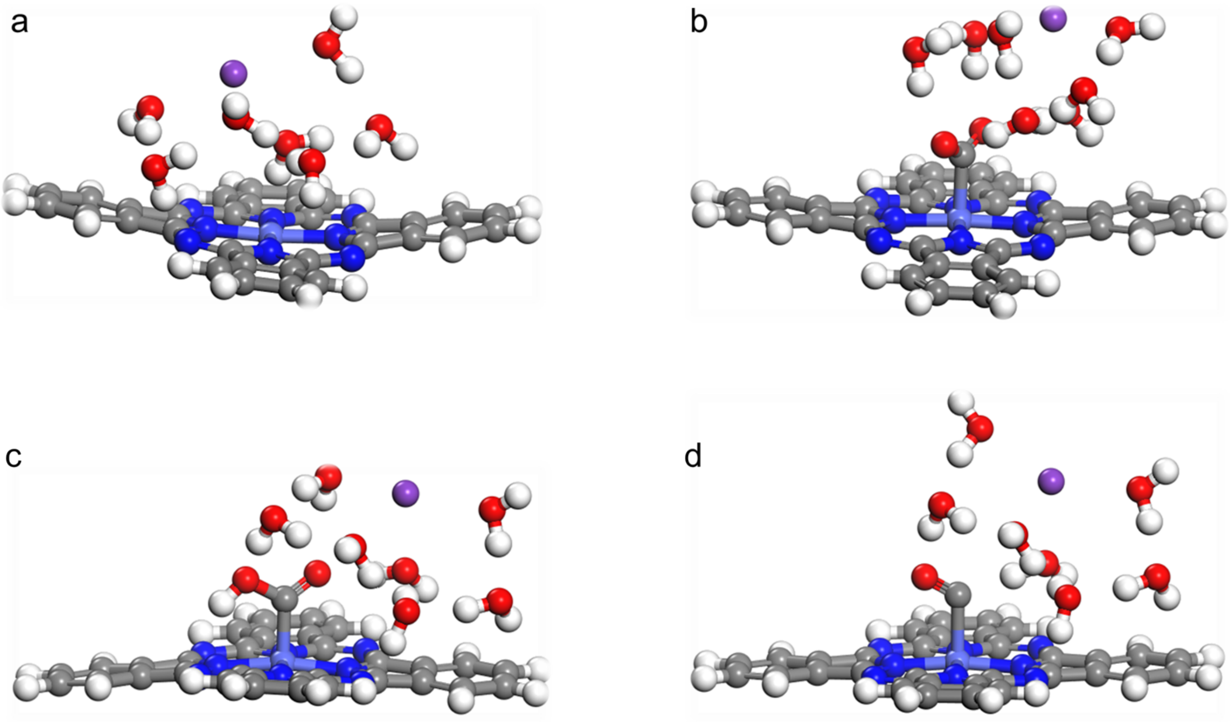

Supplementary Figure 45. The optimized atomic configuration of adsorbed intermediates (no adsorption, CO_2*, COOH*, CO*) on the pristine CoPc in CO_2RR. Carbon, grey; hydrogen, white; oxygen, red; nitrogen, blue; cobalt, indigo; potassium, purple.

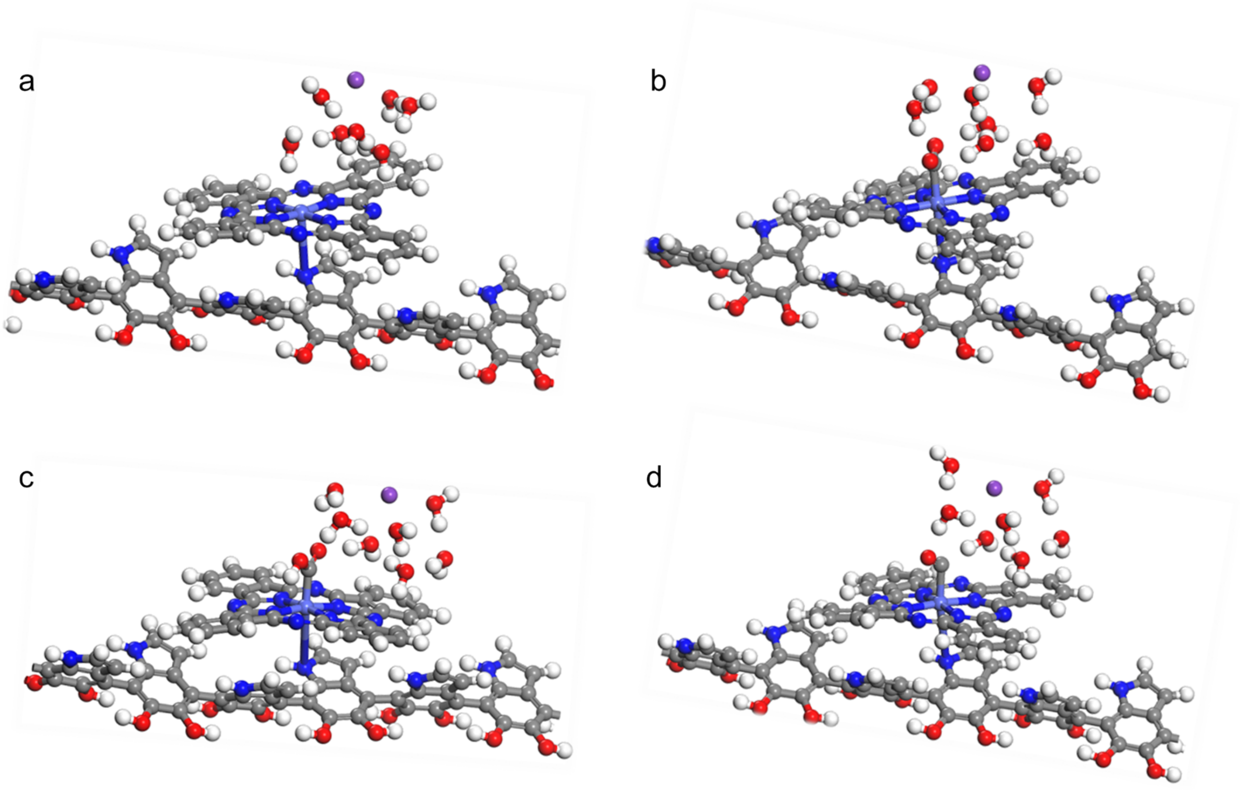

Supplementary Figure 46. The optimized atomic configuration of adsorbed intermediates (no adsorption, CO_2*, COOH*, CO*) on the CoPc/N-PDA in CO_2RR. Carbon, grey; hydrogen, white; oxygen, red; nitrogen, blue; cobalt, indigo; potassium, purple.

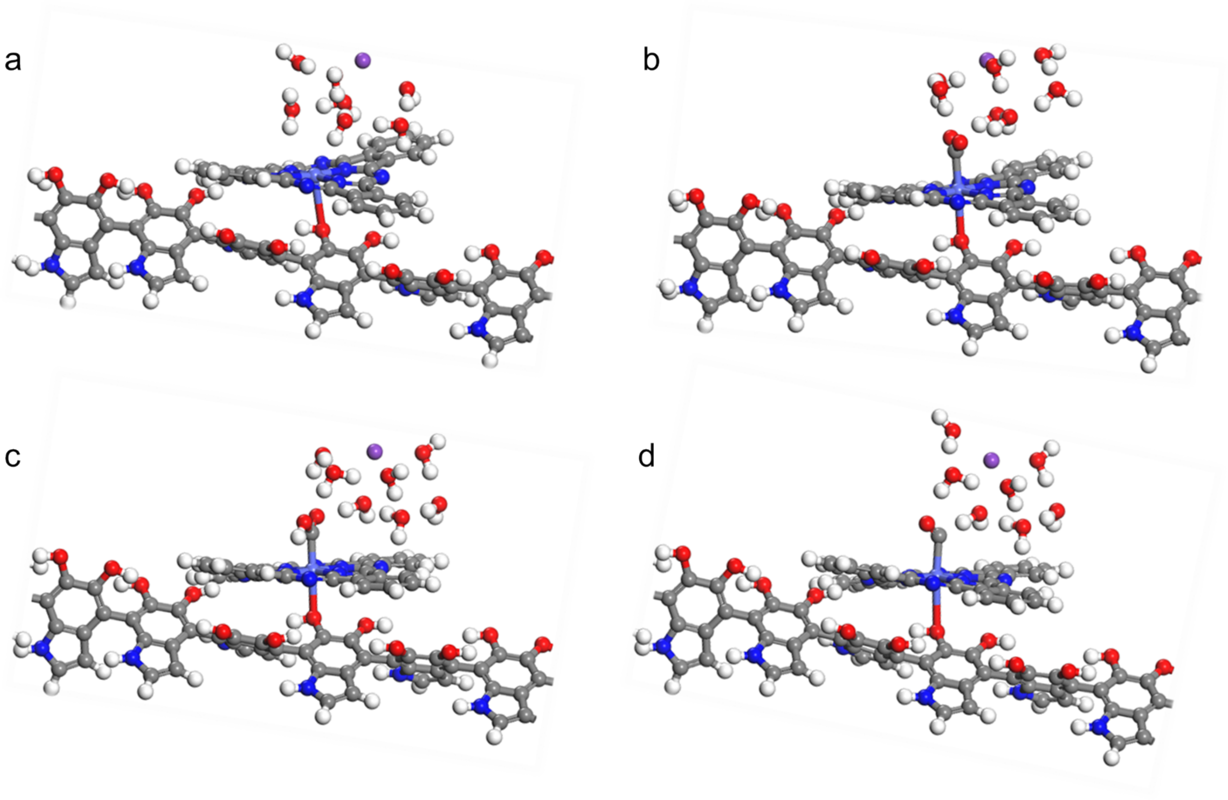

Supplementary Figure 47. The optimized atomic configuration of adsorbed intermediates (no adsorption, CO_2*, COOH*, CO*) on the CoPc/O-PDA in CO_2RR. Carbon, grey; hydrogen, white; oxygen, red; nitrogen, blue; cobalt, indigo; potassium, purple.

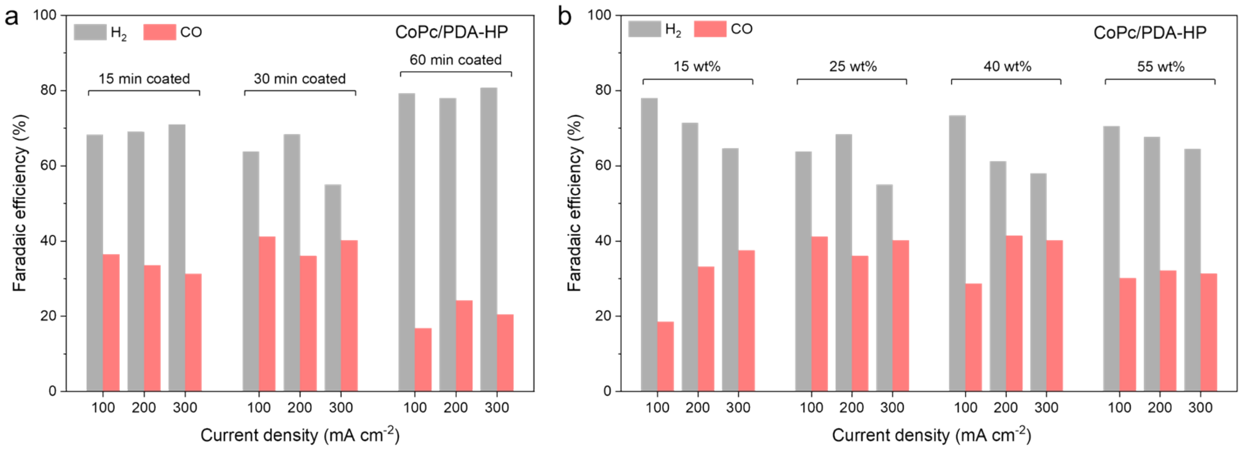

Supplementary Figure 48. Optimization of PDA treatment duration and loading. (a) Faradaic efficiency to CO and H_2 on CoPc/PDA-HP with various PDA treatment duration. (b) Faradaic efficiency to CO and H_2 on CoPc/PDA-HP with various loading amount of PDA-HP. The loading of catalyst (CoPc + PDA-HP) on carbon paper substrate is controlled at 2 mg/cm^2.

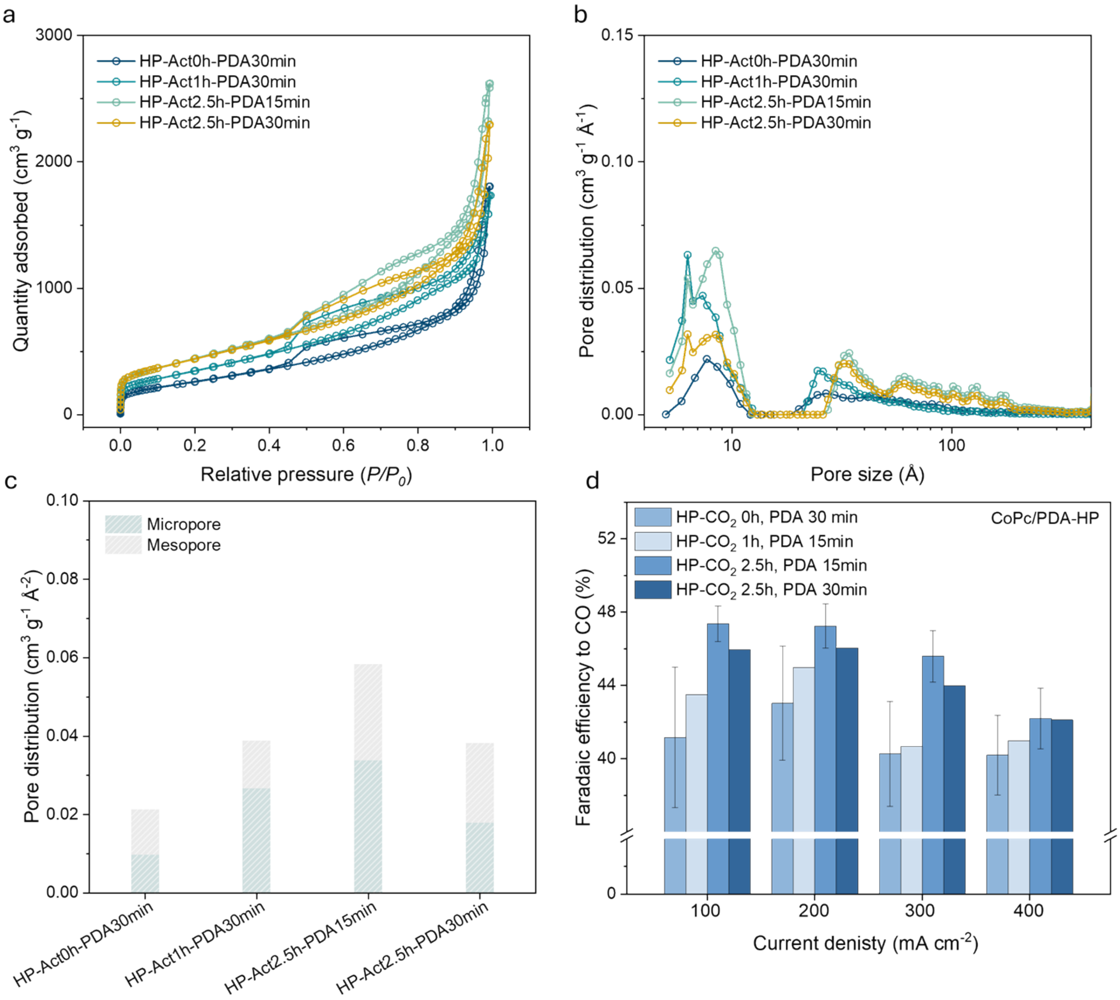

Supplementary Figure 49. Optimization of Meso-to-Micro ratio in PDA-HP. (a) BET nitrogen adsorption isotherm plot and (b) pore size distribution of PDA-coated HP with different CO_2 activation and PDA-coating durations. (c) Pore volume distributions of various carbons with the meso-to-micro pore ratio. (d) Faradaic efficiency to CO on CoPc/PDA-HP carbons. We used the optimum catalyst loading of 2 mg/cm^2 (CoPc + carbon). The catalyst contains 40 wt% carbon by mass. In the main text (Figures 2a and 4a), all performance tests were conducted using HP carbon with the optimal meso-to-micro pore ratio and PDA coating duration.

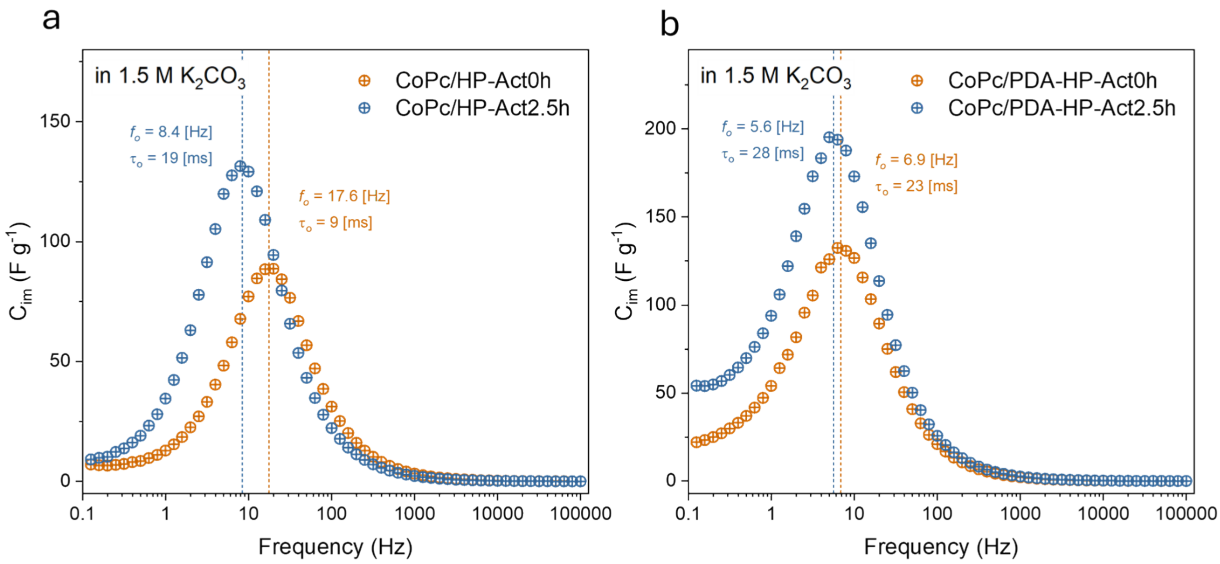

Supplementary Figure 50. EIS analysis of CoPc on HP carbon supports. Imaginary capacitance plots of CoPc loaded on HP and HP after 2.5 hours of CO_2 activation (a) without and (b) with PDA-coating.

Supplementary Note 9. the pore size effect of interposer

To control the local chemical environment (i.e., local pH and CO_2 concentrations), using an appropriate interposer layer between the cathode and membrane surface is critical (**Supplementary Figure 51-52**). We used an interposer layer with a thickness of 135 μm and tuned the pore size. From our previous simulation results in the MEA-based electrolyzer with CEM, a certain distance between the cathode and membrane enables control of local CO_2 concentrations and pH.[18] If the cathode is directly attached to the CEM or BPM interface, the acidic local environment favors HER. Meanwhile, the narrow free spaces lead to a limited transport of carbonate from the back side of the catalyst layer to the membrane surface to couple with H^+, resulting in an insufficient i-CO_2 supply. If an overly thick interposer is used, the i-CO_2 is consumed via its reactions with CO_3^{2-} or OH^- in the bulk electrolyte, also leading to a significant i-CO_2 loss.

We found that the pore size of the interposer is crucial for carbonate electrolytic activity via the *in situ* formation of triple phase boundaries (TPBs). As shown in **Supplementary Figure 52a**, according to Fick's law, i-CO_2 is transported from a high concentration (at membrane interface) to a low concentration (at catalyst surface). We assumed the catholyte flow through the interposer is a steady-state flow along the streamline. Under the constant forced flow rate of carbonate solution, the decrease pore size of interposer induced an increase of the forced flow rate of *in situ* produced CO_2 (aq) from the membrane interface to cathode surface. According to the Bernoulli principle (Eqn. 1), the increase of flow rate (increase in v) resulted in a local pressure drop inside of the pore channel of the interposer.

$$v^2/2 + gz + P/\rho = \text{constant} \quad \text{(Eqn. 1)}$$

According to the phase diagram of CO_2 (**Supplementary Figure 52b**), such local pressure drops resulted in a decrease in CO_2 (aq) solubility and accelerated the exsolution of CO_2 (g) through the rapid CO_2 (aq)-to-CO_2 (g) equilibrium shift, which induces the formation of CO_2 (g)-liquid-catalyst TPBs. As such, the total *in situ* CO_2 concentration [CO_2 (aq) + CO_2 (g)] could increase. The sufficient localized CO_2 species ensures the accessibility of the carbon reactant to catalysts and creates a thinner diffusion layer and fewer boundary gradients,[19] which can significantly facilitate reaction kinetics. Meanwhile, those equilibrium shifts and TPB formations can be dynamically regenerated during continuous electrolysis.

Experimentally, the detection of gaseous CO_2 at the outlet confirmed the CO_2 (aq)-to-CO_2 (g) equilibrium shift (**Supplementary Figure 53**). In addition, at 200 mA cm^{-2} for half-hour electrolysis, the maximum amount of CO observed was 803 μmol (equal to the FE_{CO} of 43%), and this occurred with an interposer layer pore size of 8 μm. The trend in the amount of CO_2 (g) closely aligns with the CO production rate using our CoPc/PDA-HP catalyst, exhibiting similar pore size-dependent behavior. The experimentally observed CO_2 (g) content and the CO_2-to-CO conversion rate are in line with the simulated local CO_2 concentration, indicating the TPB with sufficient CO_2 access indeed favored i-CO_2RR kinetics.

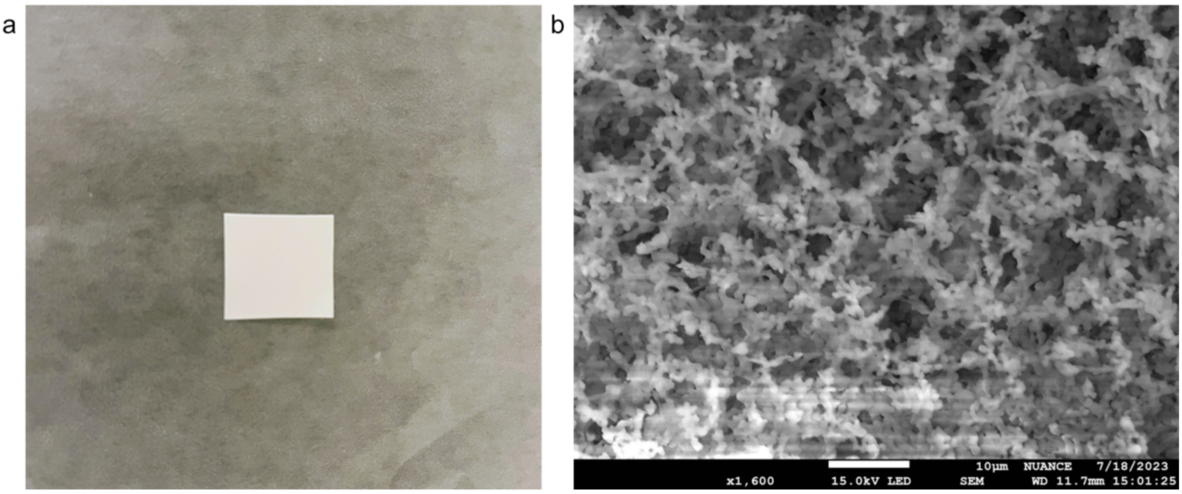

Supplementary Figure 51. (a) digital image of MCE interposer layer. (b) SEM images of interposer layer which has 8 μm-pore structures.

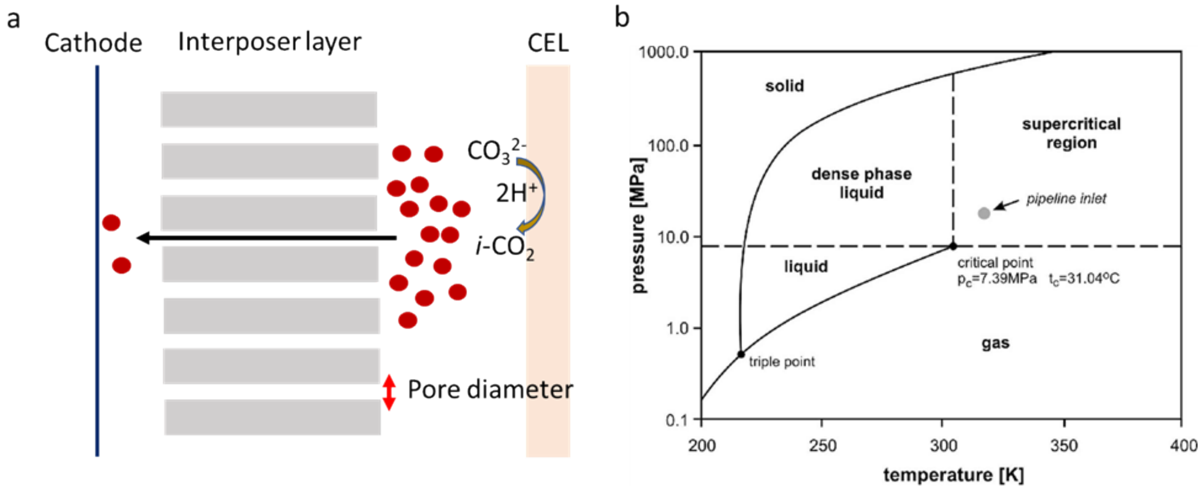

Supplementary Figure 52. (a) Local transport of i-CO_2 from CEL/electrolyte interface to the cathode surface. (b) Phase diagram of CO_2. The phase diagram is adopted from the literature.[20]

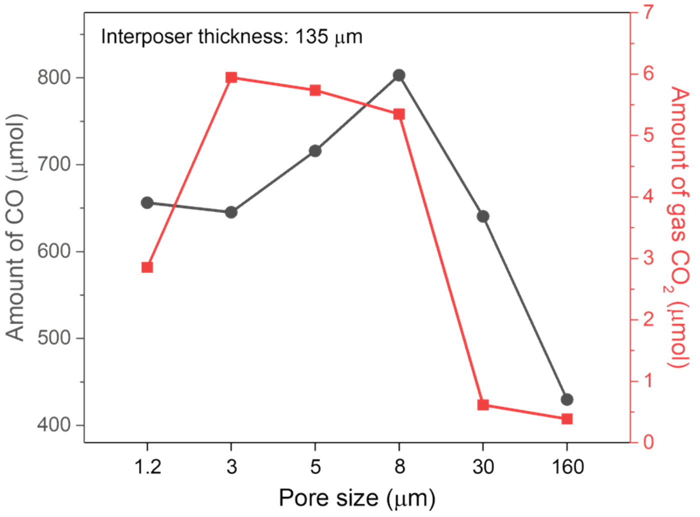

Supplementary Figure 53. Amount of CO (left Y-axis) and gas CO_2 (g) (right Y-axis) by using interposer layer with various pore diameters. The interposer thickness was controlled at 135 μm, and the electrolysis was performed at 200 mA cm^{-2} for 30 min.

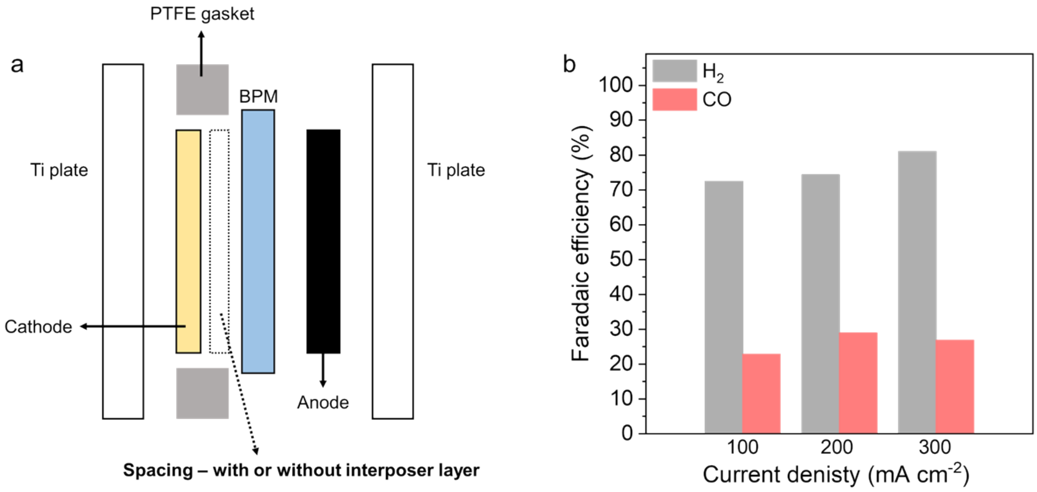

Supplementary Figure 54. (a) BPM system configuration with or without interposer layer. (b) Faradaic efficiency of CO and H_2 on CoPc/PDA-HP catalyst without interposer layer.

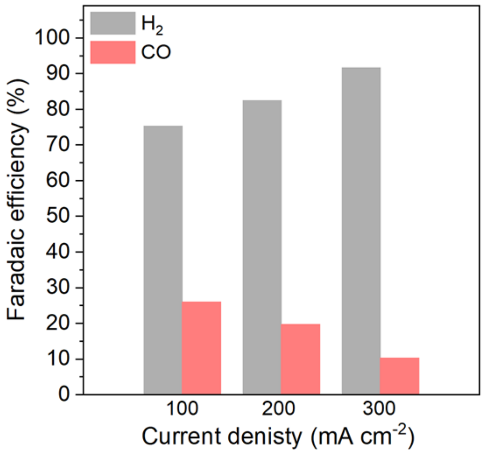

Supplementary Figure 55. Faradaic efficiency of CO and H_2 on CoPc catalyst loaded on air treated (oxidized) HP.

Supplementary Note 10. Analysis of OH^- regeneration at the cathode

The Faradaic efficiency for $OH^–$ generation was calculated based on the pH change of the electrolyte. We performed continuous 24-hour electrolysis at 100 mA. The catholyte (1.5 M K_2CO_3) volume was 200 mL. We used a calibrated pH probe and tested the pH changes of the electrolyte:

Before electrolysis: pH = 12.17

After 24-hour electrolysis: pH = 13.23

We define the Faraday efficiency for $OH^–$ as in the more-common electrodialysis systems[19]

$$FE_{OH^-} = \frac{accumulated\ mols\ of\ OH^-}{mols\ of\ charge\ passed} \times 100\%$$

Basically, the maximum rate of $OH^–$ can generate is given by the product of the current, Faradays constant, and the FE for CO_2 reduction assuming the concentration of bicarbonate is small in the cell and the only charge-carrying anions are $OH^–$ and $CO_3^{2–}$, which a reasonable assumption at the high pH operation of > 12.

During electrolysis, at the BPM surface, RXN 1-2 occurs, leading to CO_2 release. At the cathode, HER and *i*-CO2RR take place (RXN 3-4), both of which generate $OH^–$. The H^+ generation at the BPM surface (RXN 1) through water dissociation is balanced with the $OH^–$ generation at the cathode layer (RXN 3-4). At steady state, $OH^–$ must carry the ionic current for any HER faradaic reaction because carbonate is not consumed in the HER.

The accumulation of $OH^–$ occurs during the carbonate-to-CO_2-to-CO conversion process (RXN 3). For instance, if 10 moles of electrons pass through the system, 10 moles of H^+ will theoretically be generated at the BPM interface (RXN 1), releasing 5 moles of CO_2. If 2 moles of CO are produced from the CO_2-to-CO conversion (with FE_{CO} = 40%), 4 moles of $OH^–$ will be generated from RXN 3, leaving 3 moles of unreacted CO_2. During this process, 4 moles of electrons are used. The remaining 6 moles of electrons are consumed by the HER, generating 6 moles of $OH^–$ through RXN 4. This $OH^–$ is then consumed by the unreacted CO_2, converting it back to $CO_3^{2–}$ (RXN 5). Ultimately, 4 moles of $OH^–$ accumulate as a result of RXN 3, where CO_2 is utilized for CO production. Essentially, for every electron used in the reduction of CO_2, one $OH^–$ is produced.

BPM interface: $water\ dissociation: 2H_2O(l) \rightleftharpoons 2H^+(aq) + 2OH^-(aq)\ (RXN\ 1)$

i-CO_2 generation: $CO_3^{2-}(aq) + 2H^+(aq) \rightleftharpoons CO_2(g) + H_2O(l)$ (RXN 2)

$Cathode\ layer$: $CO_2(g) + 2H_2O + 2e^- \rightleftharpoons CO(g) + 2OH^-\ \ (RXN\ 3)$

$$2H_2O + 2e^- \rightarrow H_{2(g)} + 2OH^-_{(aq)} \ (RXN\ 4)$$

$$CO_{2(g)} + 2OH^- \rightarrow CO_3^{2-} + H_2O \ \ (RXN\ 5)$$

We have measured and calculated the faradaic efficiency for OH⁻ generation (FE_{OH^-}) based on the pH change and the moles of charge passed for 24-hour electrolysis at 100 mA. The FE_{OH^-} is ~ 35%, which is close to the average FE_{CO}.

The result showed that one electron used for carbon to CO conversion, one molecule of OH⁻ would be regenerated. It indicated that the alkaline capture solution can be regenerated after reactive capture.

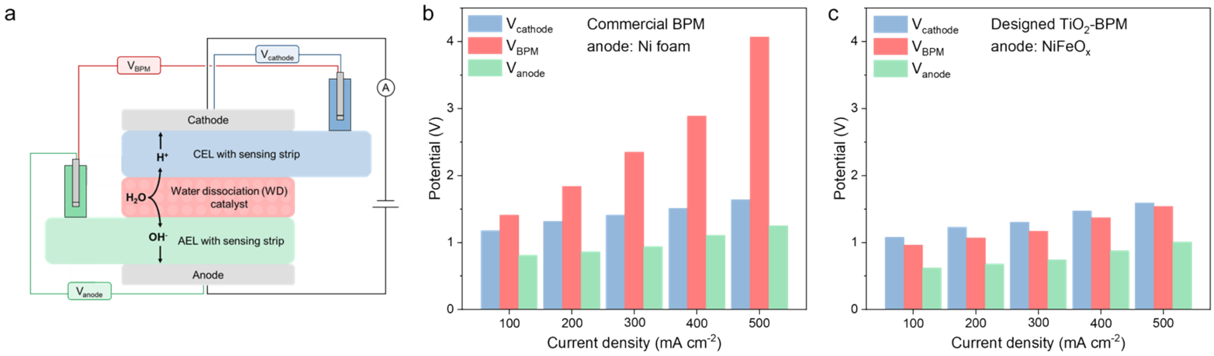

Supplementary Figure 56. Voltage breakdown measurements. (a) Schematic illustration of the membrane-potential-sensing setup in a BPM electrolyzer. Two reference electrodes and two sensing strips were used to monitor the voltage distribution in the electrolyzer. Voltage breakdown measurements in the (b) commercial BPM- and (c) custom-designed BPM-based electrolyzers at different current densities. The full cell voltages are the sum of all potentials for each component, which are recorded after 5 min of steady-state electrolysis.

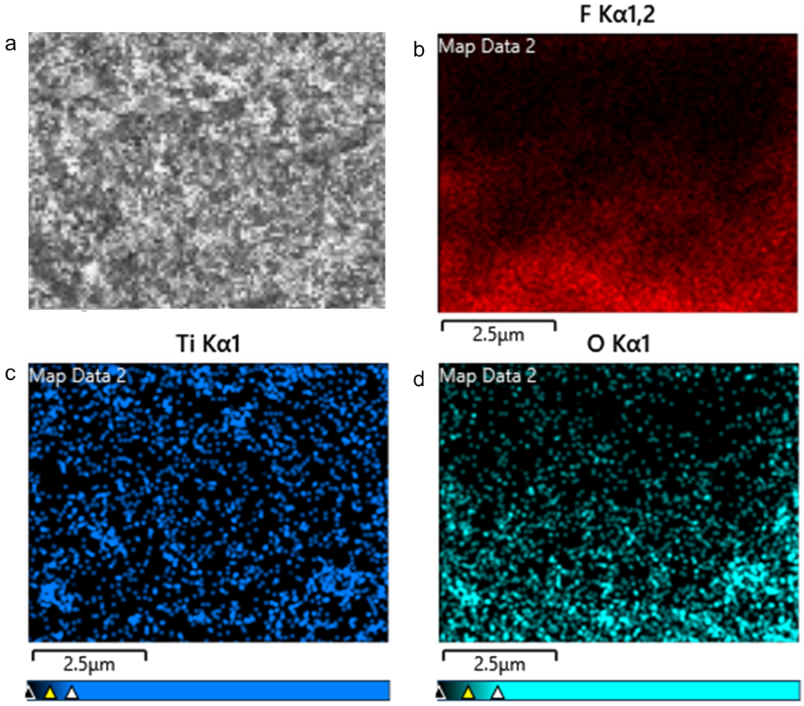

Supplementary Figure 57. SEM-EDS mapping of water dissociation catalyst (P25 TiO_2) layer on Nafion membrane.

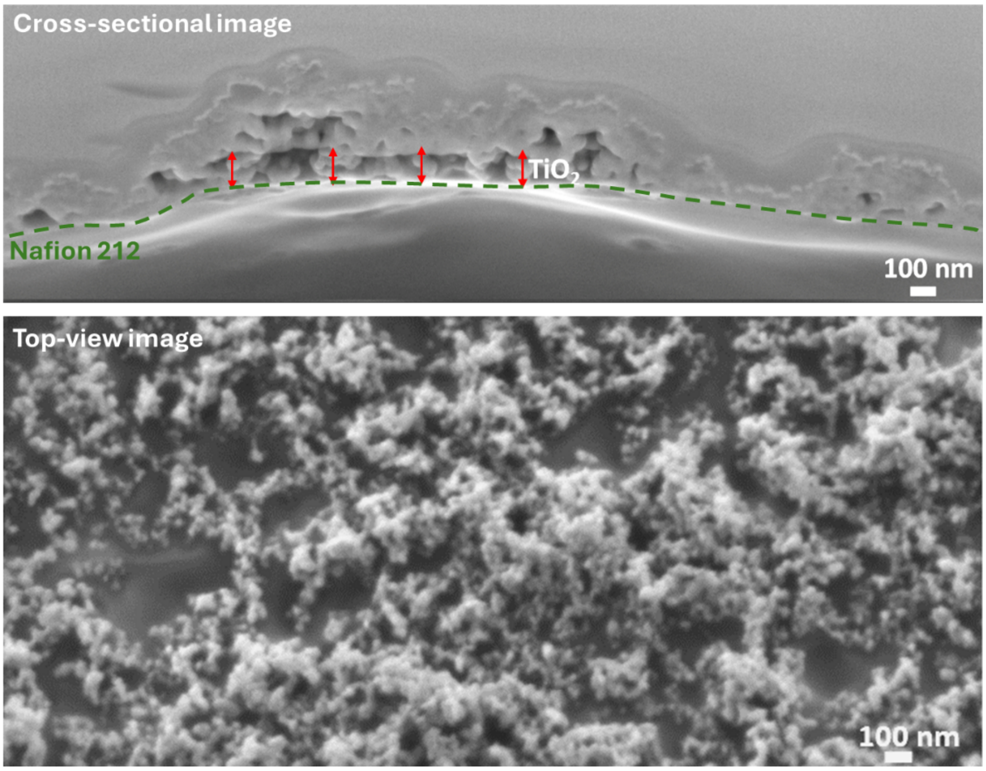

Supplementary Figure 58. SEM images of the custom-designed BPM with P25 TiO_2 catalyst spin-coated on the CEL. The top image presents a cross-sectional view of the catalyst layer on Nafion 212, while the bottom image shows a top-view image of the P25 TiO_2 catalyst layer. To prepare the cross-sectional sample, two layers of Pt were coated on the TiO_2 catalyst: one applied using a sputter coater and another deposited by the electron beam of the FIB. The image was captured at a 35-degree tilt.

Supplementary Table 4. Comparison of electrochemical conversion of carbon captured liquid to various products.

Reactant	Membrane	Cathode	Anode	Current density (mA cm^{-2})	Cell voltage (V)	Desired product	FE of product (%)	Maximum partial current density (mA cm^{-2})	EE (%)[b]	Stability (h)	Ref.
Potassium carbonate	P25 TiO_2-BPM	CoPc/PDA-HP	$NiFeO_x$	200	2.9	CO	47	222[a]	50	40	This work
	BPM	Ag NPs	Ni foam	200	3.8	CO	18	36	32	N/A	[21]
	CEM	Ag NPs	IrO_x/Ti	200	3.6	CO	46	92	42	23	[22]
	CEM	Cu/CoPc-CNTs	IrO_x/Ti	200	3.6	C_2H_4	34	68	N/A	20	[9]
Potassium bicarbonate	BPM	Ag foam	Ni foam	200	4.2	CO	32	64	N/A	10	[5]
	BPM	Ag NPs	Ni foam	200	N/A	CO	62	124	N/A	2.5	[23]
	BPM	Ag-coated carbon cloth	Platinum mesh	100	3.5	CO	37	37	N/A	2.5	[24]
	BPM	Ni-SAC	Ni foam	200	3.7	CO	93	186	N/A	18	[6]
	BPM	Porous Cu	Ni foam	400	7.0	CH_4	27	108	N/A	N/A	[25]
	BPM	Bi/C	Ni foam	100	4.1	$HCOO^-$	65	65	N/A	N/A	[26]
	BPM	CuSus/AgNaf	Ni foam	100	3.7	C_{2+}	42	42	N/A	N/A	[27]
Ammonium bicarbonate	AEM	ED-Bi	Ni foam	100	2.4	$HCOO^-$	75	75	N/A	5	[28]
Bicarbonate and carbonate mixture	BPM	Ag/C	Ni foam	50	3.5	CO	13	6.5	N/A	N/A	[29]
Amine-CO_2	CEM	Ag	Ni foam	100	N/A	CO	19	19	N/A	10	[30]
	CEM	Ni-N/C	TiO_2	100	N/A	CO	30	30	N/A	N/A	[31]

a. The maximum partial current density was based on the experimental results in main text Figure 4a, with 600 mA cm^{-2} and CO FE of 37%.

b. Syngas: molar ratio of H_2: CO = 2:1
If $FE_{CO} < 33\%$, additional CO was supplied from DAC-SOEC process. When the SOEC is assumed, the EE to CO is set to 80%. The analysis does assume (DAC+SOEC), the need for CO_2 regeneration, circulation, and an air contactor. The resultant effective EE for CO is 25% in this case of "CO-infill".

If $FE_{CO} > 33\%$, additional H_2 from water electrolyzer having EE for H_2 of 65%.

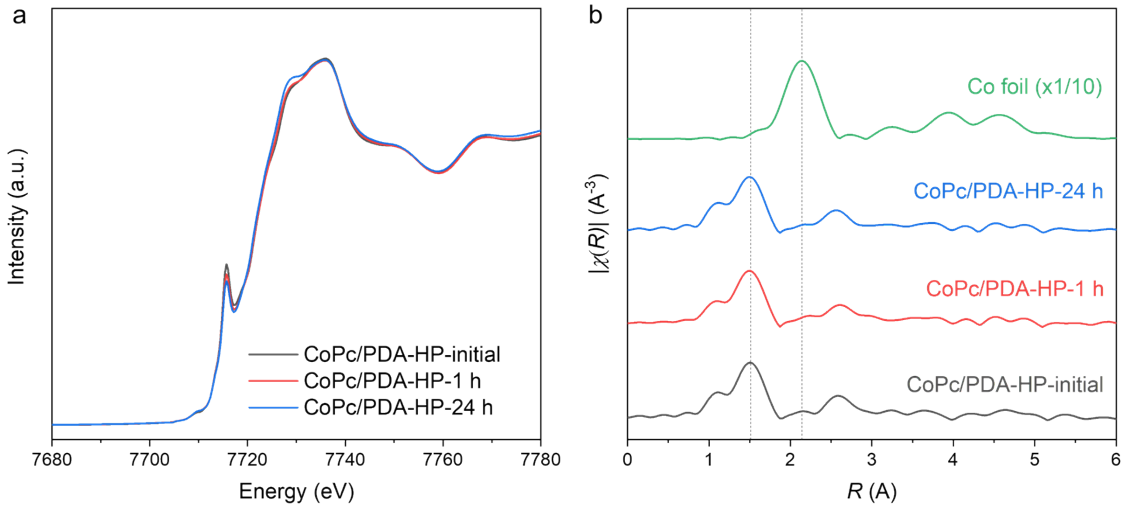

Supplementary Figure 59. Co K-edge (a) XANES and (b) EXAFS spectra of CoPc/PDA-HP catalyst before and after 1 and 24 h carbonate conversion reaction at 100 mV s^{-1}.

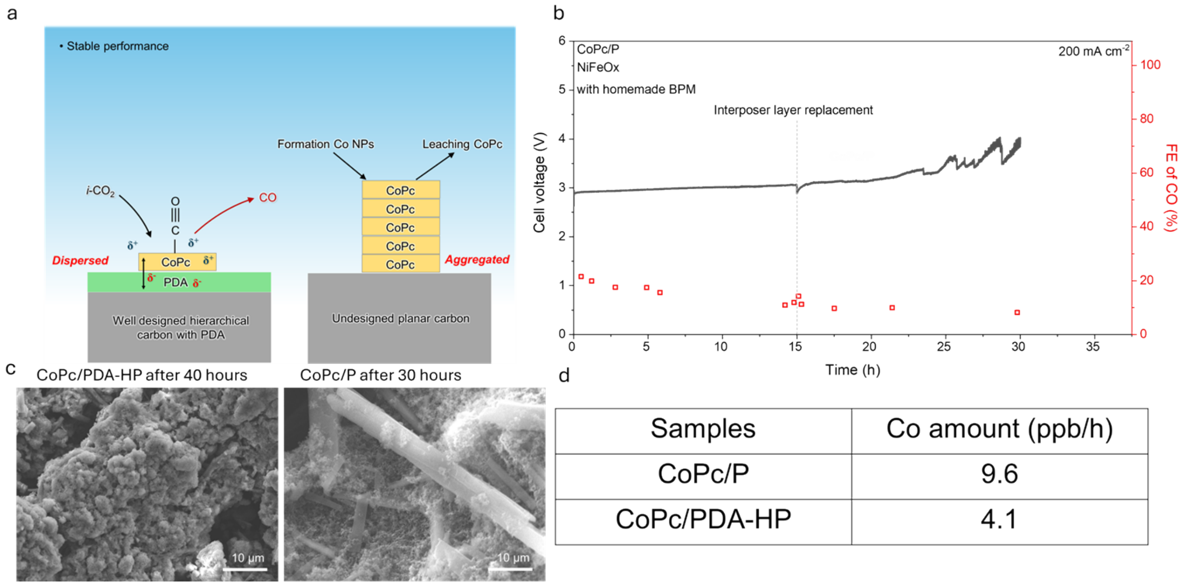

Samples	Co amount (ppb/h)
CoPc/P	9.6
CoPc/PDA-HP	4.1

Supplementary Figure 60. Stability comparison between CoPc/P and CoPc/PDA-HP. (a) Cell voltage (left Y-axis) and Faradaic efficiency to CO (right Y-axis) for 30 hours of electrolysis at 200 mA cm^{-2} for the case of the CoPc/P catalyst. The interposer layer was replaced after 15 hours. (b) SEM images of CoPc/PDA-HP and CoPc/P after stability tests at 200 mA cm^{-2} for 40 and 30 hours, respectively. (c) Schematic illustration showing how well-dispersed CoPc on the designed carbon support helps minimize aggregation under applied bias. (d) ICP analysis of post-electrolysis solutions, highlighting the different CoPc leaching rates into the catholyte.

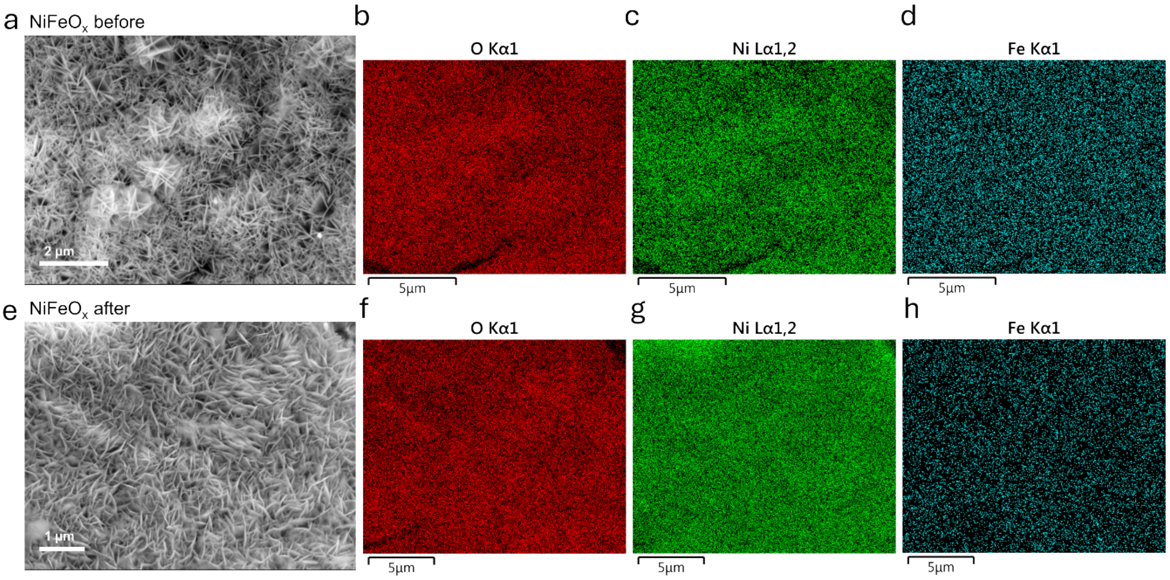

Supplementary Figure 61. SEM images of NiFeOx before and after 40-hour stability test at 200 mA/cm2 for carbonate electrolysis.

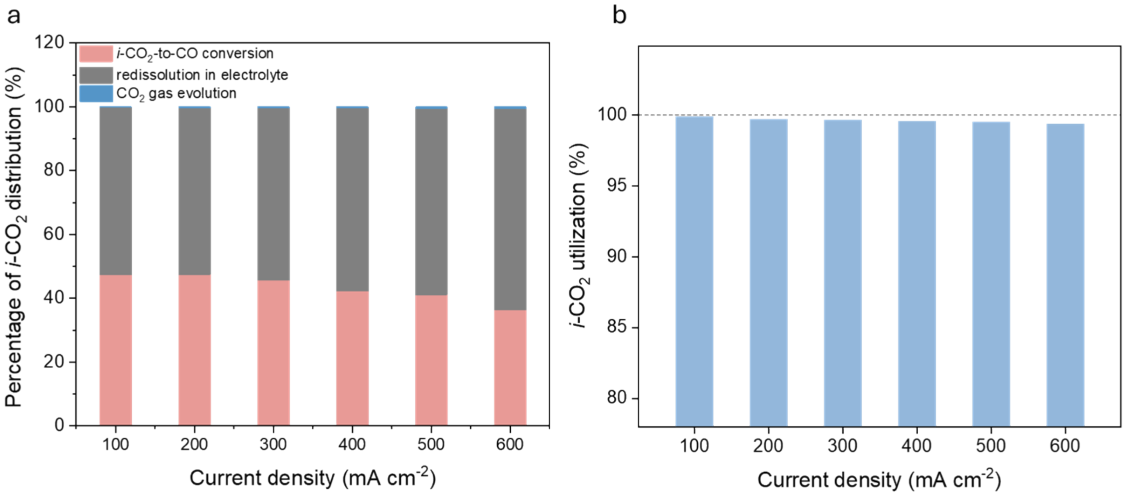

Supplementary Figure 62. (a) *i*-CO_2 distribution and (b) Carbon utilization for carbonate electrolysis of 30 min on CoPc/PDA-HP at 100-600 mA cm^{-2}.

Carbon utilization is defined as 1 minus the normalized ratio of CO_2 gas detected in the outlet of the carbonate system to the theoretically produced *i*-CO_2 at the BPM/electrolyte interface. The carbon utilization can be calculated by the equations as follows:

$$Carbon\ utlization = \left(1 - \frac{n_{CO2\ (g)}}{n_{CO2}^{0}}\right) \times 100\ \% = \left(1 - \frac{2Fn_{CO2\ (g)}}{Q}\right) \times 100\ \%$$

The redissolution of *i*-CO_2 occurred through the following reactions:

$CO_2(g) + OH^-(aq) \rightleftharpoons HCO_3^-(aq)$

$CO_2(g) + CO_3^{2-}(aq) + H_2O(l) \rightleftharpoons 2HCO_3^-(aq)$

$CO_2(g) + 2OH^-(aq) \rightleftharpoons CO_3^{2-}(aq) + H_2O(l)$

System	Electrolyte	Membrane	Cathode	Maximum Carbon utilization (%)	Reactor	Desired product	Ref.
Reactive capture	K_2CO_3	BPM	CoPc/PDA-HP	~99	MEA	CO	This work
	$KHCO_3$	BPM	Ag	~40	MEA	CO	[22]
	NH_4HCO_3	AEM	ED-Bi	75	MEA	$HCOO^-$	[28]
Gas CO_2 reduction	KOH	AEM	CoPc/C	4	Alkaline flow cell	CO	[32]
	KOH	AEM	Cu	24	Alkaline flow cell	C_{2+}	[33]
	N/A	AEM	Ag	40	Alkaline MEA	CO	[34]
	$KHCO_3$	AEM	Ni-SAC	40	Nuetral MEA	CO	[15]
	$KHCO_3$	AEM	Cu	4	Nuetral flow cell	C_{2+}	[35]
	N/A	AEM	Cu	30	Nuetral MEA	C_{2+}	[18]
	N/A	BPM [b]	Cu	78	Nuetral MEA	C_{2+}	[36]
	H_2SO_4	CEM	Ag	84	Acidic flow cell	CO	[37]
	Cs_2SO_4 (pH = 3)	CEM	Au/C	14	Acidic flow cell	CO	[38]
	H_3PO_4	AEM	Cu	45	Acidic flow cell	C_{2+}	[39]
	N/A	BPM	CuPc	78	Acidic MEA	CH_4	[40]

Supplementary Table 5. Comparison of carbon utilization in different systems.

b. In the gas CO_2 system, the carbon loss originates from three parts:
  (1) The escape of unreacted CO_2.
  (2) The combination reaction between CO_2 and OH^- to generate (bi)carbonate.
  (3) The crossover of (bi)carbonate.

c. A stationary unbuffered catholyte layer between BPM and cathode was used to keep the cathode interface as neutral.

Supplementary Note 11. Integrated system for direct air capture (DAC) coupled with carbonate electrolysis

DAC using a membrane contactor

In the ambient air where the CO_2 partial pressure is only ~400 ppm (roughly 0.4 mbar), carbonate species dominate in the post capture solution: $[CO_3^{2-}(aq)] >> [HCO_3^{-}(aq)]$ (**Supplementary Fig. 63**).

We present a practical lab-scale demonstration of DAC (**Supplementary Fig. 64**). Air was introduced into the membrane contactor at a flow rate of 500 sccm. Simultaneously, 50 mL of 3 M KOH solution was pumped into the membrane contactor at a rate of 100 mL/min using a peristaltic pump. A digital pH probe monitored the pH of the solution at specified time intervals. The combination of high KOH concentration and elevated air flow rate in the membrane contactor enhanced the CO_2 capture efficiency.

We observed a gradual decrease in the solution's pH, indicating the capture of CO_2 from the air. Based on the specification diagram for CO_2, HCO_3^-, and CO_3^{2-} as functions of pH (**Supplementary Fig. 63**), several reactions took place during the CO_2 absorption experiment. Initially, KOH reacts with CO_2 to form K_2CO_3 (Stage 1, RXN 1). Subsequently, K_2CO_3 reacts with additional CO_2 to produce $KHCO_3$ (Stage 2, RXN 2). Finally, the $KHCO_3$ solution becomes progressively saturated with CO_2 gas (Stage 3, RXN 3).

$$2KOH + CO_2 \rightarrow K_2CO_3 + H_2O \quad \text{(RXN 1)}$$

$$K_2CO_3 + CO_2 + H_2O \rightarrow 2KHCO_3 \quad \text{(RXN 2)}$$

$$CO_2\,(g) \rightarrow CO_2\,(aq) \quad \text{(RXN 3)}$$

Due to the low CO_2 concentration (~400 ppm) in the air and the high concentration of KOH in the capture solution, the primary reaction for a prolonged period was RXN 1, which neutralized the OH^- and slowly lowered the pH. The results showed that it took approximately 3 hours/mL for the solution to predominantly convert to K_2CO_3, with the pH decreasing from 14.6 in pure 3 M KOH to 12.8 as K_2CO_3 became the dominant species (**Supplementary Fig. 65a**), which corresponds to a CO_2 load of 64.7 g/L (**Supplementary Fig. 65b**).

CO_2 load (g/L) is calculated by:

$CO_2 \text{ load } = ([OH]_0 - [OH])/2 \times 44$

$pH =- log[H^+] =- log(\frac{10^{-14}}{[OH^-]})$

$pOH = 14 - pH$

$[OH^-] = 10^{-pOH}$

$[OH]_0$ is the OH⁻ concentration before reaction, which is 3 M in our case. $[OH]$ is the OH⁻ concentration that is measured by pH probe.

When the solution pH dropped to ~12.8, we qualitatively assessed the amount of K_2CO_3 formed by performing a precipitation reaction, as detailed below:

$$Ca(Cl)_2(aq) + K_2CO_3(aq) \rightarrow CaCO_3(s) + 2KCl\,(aq)$$

The precipitation occurs immediately upon mixing the clear $CaCl_2$ solution with the pH 12.8 post-capture liquid (**Supplementary Fig. 66**). After filtration and drying, the XRD pattern of the resulting white powder confirmed the formation of $CaCO_3$.

Due to the reduced basicity, the rate of conversion of K_2CO_3 to $KHCO_3$ becomes extremely slow (Stage 2). The conversion of carbonate to a slight ratio of bicarbonate in the 2nd stage is also monitored via pH changes and calculated using the dissociation constant of carbonic acid.

Carbonic acid (H_2CO_3) is a weak acid that dissociates in two steps. The dissociation constants for these steps are known as pK_{a1} and pK_{a2}.

First Dissociation Step:

$$H_2CO_3 \rightleftharpoons H^+ + HCO_3^-$$

The dissociation constant for this step is K_{a1}, and the negative logarithm of K_{a1} is pK_{a1}.

Second Dissociation Step:

$$HCO_3^- \rightleftharpoons H^+ + CO_3^{2-}$$

The dissociation constant for this step is K_{a2}, and the negative logarithm of K_{a2} is pK_{a2}.

The Pk_{a1} and PK_{a2} are 6.35 and 10.33, respectively. To determine the carbonate and bicarbonate composition in the stage of converting carbonate to bicarbonate, we used pK_{a2} for the calculation.

$$K_a2 = \frac{[H^+][CO_3^{2-}]}{[HCO_3^-]}$$

$$[H^+] = 10^{-pH}$$

$$K_a2 = 10^{-pK_a2} = 10^{-10.33} \approx 4.68 \times 10^{-11}$$

$$\frac{[HCO^-_3]}{[CO^{2-}_3]}=\frac{[H^+]}{K_a2}$$

The results demonstrated that the conversion of carbonate to bicarbonate proceeds very slowly (**Supplementary Fig. 65a**). It took an additional ~6 hours/mL for the pH to decrease from 12.76 to 12.25. After 8.4 hours/mL of continuous DAC, the ratio of HCO_3^- was still <2% in the carbonate and bicarbonate mixed solution. This finding aligns with literature reports indicating that the conversion of K_2CO_3 to $KHCO_3$ is significantly slower. The differential CO_2 capture rate (unit: mole h^{-1} L^{-1}) showed that the capture kinetics significantly decreased when the capture solution pH < 13.5 (**Supplementary Fig. 65c**).

To achieve the same CO_2 capture rate, a K_2CO_3-based system for producing $KHCO_3$ requires up to 14 times more contactors than a KOH-based system for producing K_2CO_3.[41] Given that air contactor capital expenditures (CAPEX) constitute approximately ~20% of the total DAC cost, using a post-capture solution primarily composed of $KHCO_3$ would be practical in the future unless the cost of air contactors is substantially reduced.

Carbonate electrolysis using DAC post-capture solution

We subsequently used a pH 12.8 solution from the DAC process for continuous electrolysis to produce syngas. For the electrolysis setup, we employed CoPc/PDA-HP as the cathode and Ni foam as the anode, with a commercial BPM membrane. At current densities ranging from 100 to 400 mA/cm², we achieved a FE_{CO} of over 40%.

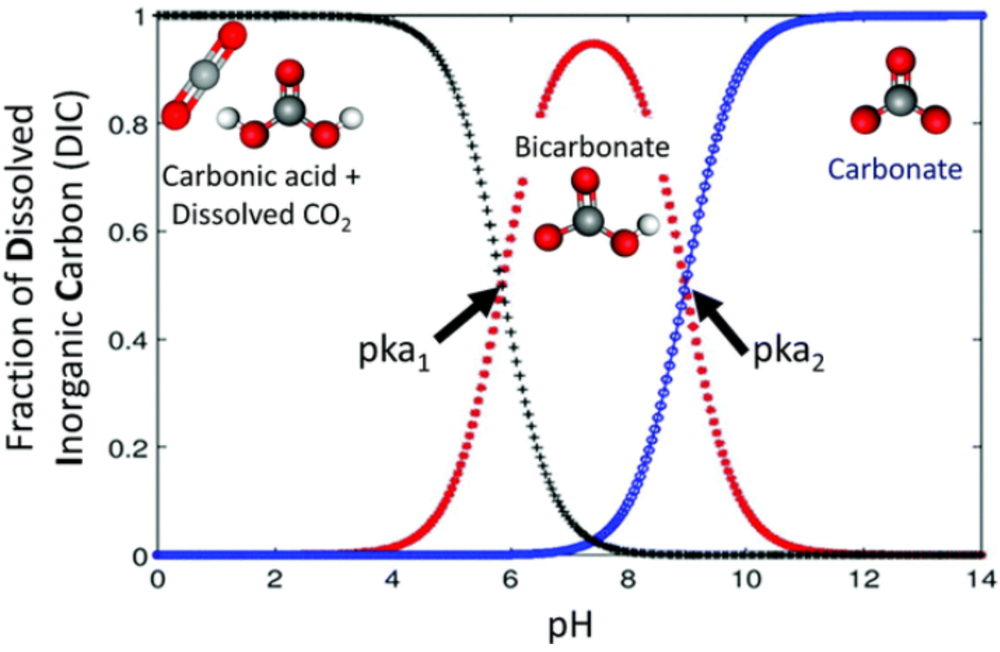

Supplementary Figure 63. Speciation diagram for the carbonic acid system as a function of pH at room temperature. This figure is adopted from the literature.[42]

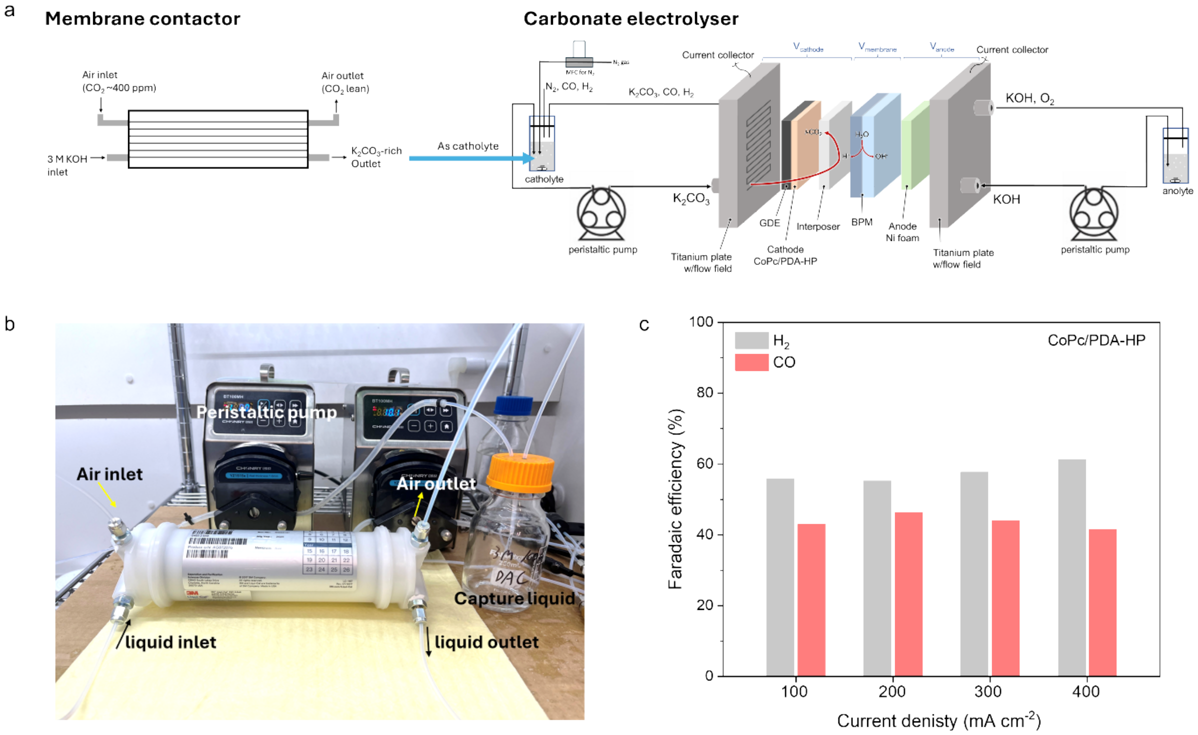

Supplementary Figure 64. Lab-scale integrated system for DAC coupled with carbonate electrolysis. (a) Schematic illustration of the combined system integrating direct air capture (DAC) with carbonate electrolysis. DAC was conducted using a membrane contactor with 3 M KOH as the capture solution. The resulting carbonate-rich solution was then used for carbonate electrolysis in a BPM-based electrolyzer to produce syngas. (b) Photograph of the membrane contactor setup. (c) Faradaic efficiency (FE) of H_2 and CO on CoPc/PDA-HP catalysts using the post-capture carbonate-rich solution.

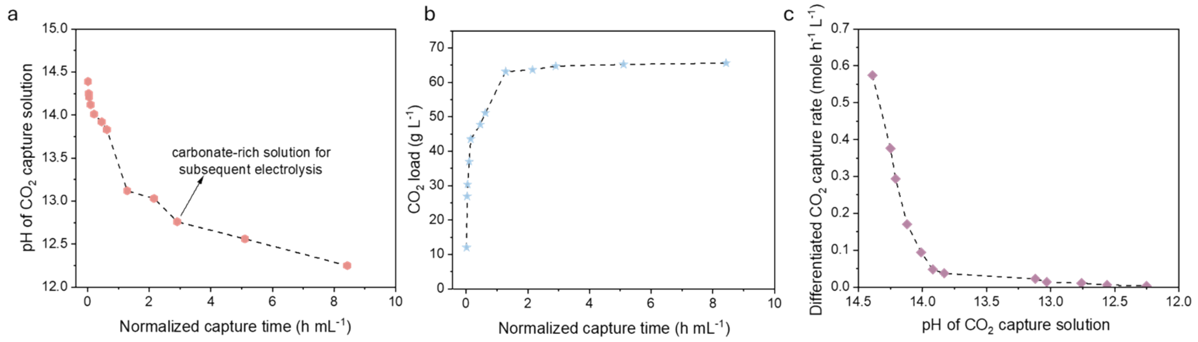

Supplementary Figure 65. Capture kinetic study. (a) pH of the CO_2 capture solution, and (b) CO_2 loading relative to the volumetric normalized capture time. (c) Differentiated CO_2 capture rate as a function of the pH of the CO_2 capture solution.

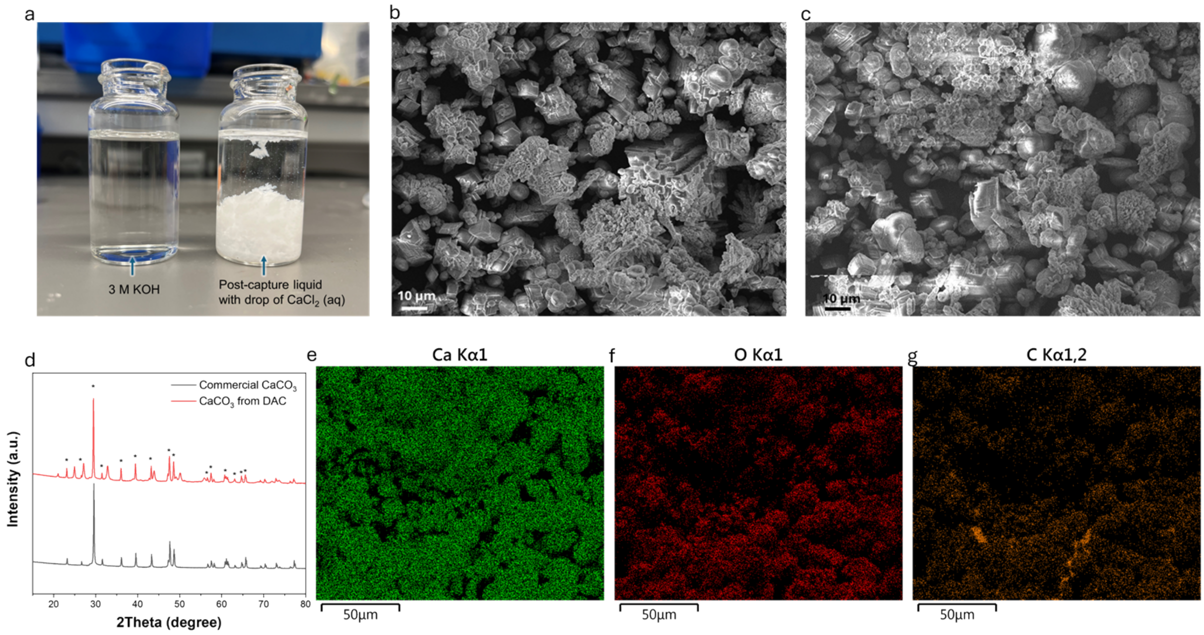

Supplementary Figure 66. Characterization of post-capture liquid. (a) Photo of 3 M KOH capture liquid and carbonate-rich post capture liquid with the addition of $CaCl_2$ solution in the formation of $CaCO_3$ (s) precipitation. (b) SEM images of the solid $CaCO_3$ powder. (c) XRD of $CaCO_3$, showing the crystallization of solid $CaCO_3$. The other peaks correspond to the $Ca(OH)_2$. (d) EDS analysis with Ca, O, and C peaks.

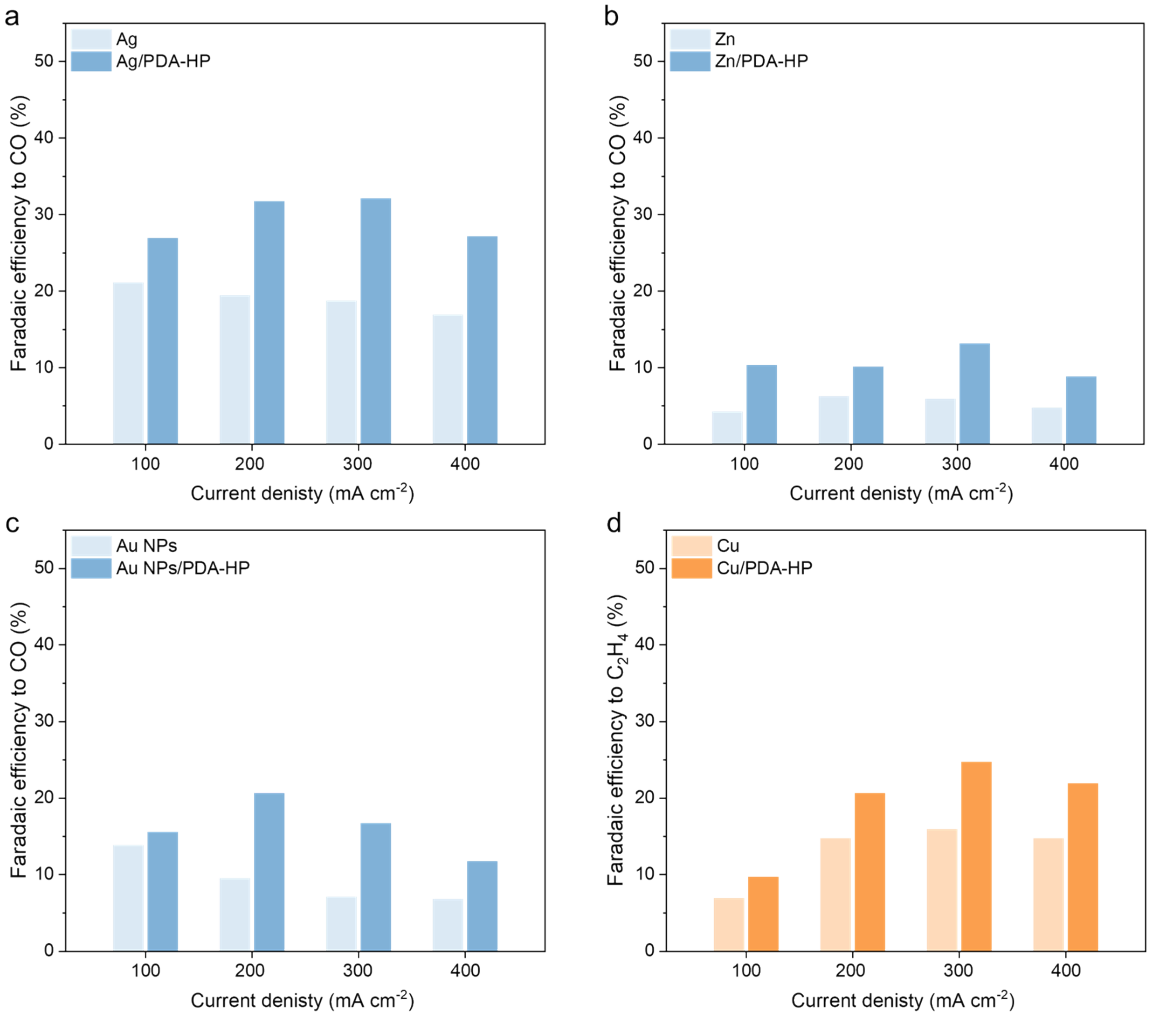

Supplementary Figure 67. Carbon support design strategy applied to metal catalysts for carbonate electrolysis. Faradaic efficiency to CO for (a) Ag, (b) Zn, and (c) Au nanoparticles with and without PDA-HP carbon support. (d) Faradaic efficiency to C_2H_4 for Cu nanoparticles with and without PDA-HP carbon support.

Supplementary Note 12. Energy intensity estimation

The energy consumption is based on the Carbon Engineering DAC process[1], which uses KOH as the CO_2 capture absorbent. The energy required for the air contactor is 0.3 GJ per tonne of CO_2. For a syngas mixture with a 2:1 H_2:CO molar ratio and a total mass of 1 tonne syngas, the mass of CO is 0.875 tonnes. Assuming a 99% conversion efficiency from CO_2 to CO, the energy consumption is calculated as:

$$\left(\frac{0.875}{28} \times \frac{44}{0.99}\right) \times 0.3 = 0.42\ GJ/\text{tonneSyngas}$$

Sequential capture and electrified conversion

CO_2 in the air was captured in an alkali hydroxide solution and then released at high purity through high-temperature operation (*i.e.*, 900 °C). The energy cost estimation was based on a previous study.[1] DAC is followed by feeding the purified CO_2 into a high-temperature solid oxide electrolysis cell (SOEC) for CO_2-to-CO conversion typically at 700−900 °C. Unreacted CO_2 is separated from CO stream and circulated in this device to achieve 99% CO_2-to-CO conversion. Typically, this process costs 16 GJ/tonCO for electrolysis and heat.[43] Green H_2 is produced from water electrolysis with an EE of 65%, for matching the desirable H_2:CO ratio of 2:1.

Sequential capture and reverse water-gas shift (RWGS) using green hydrogen

This approach uses RWGS process to convert high purity CO_2 (from DAC) and green H_2 (from water electrolyzer) to yield 2:1 syngas. We assume that the RWGS operates at 70% energy efficiency for CO_2-to-CO reaction. Unreacted CO_2 is separated and circulated to achieve 90% CO_2-to-CO conversion.

Integrated approach reactive capture

The integrated approach avoids the energy cost, carbon emissions and CAPEX for CO_2 regeneration. Instead, it uses a contactor to capture CO_2 from the air and feed the yielded carbonate solution to a low temperature electrolyzer. The output of the carbonate electrolyzer is complemented by H_2 production from a water electrolyzer to obtain a H_2/CO (65% EE) molar ratio of 2. The energy cost is calculated from the experimental results operating at 100 and 200 mA cm^{-2}.

Supplementary Table 6. Comparison of energy and carbon intensity for sequential vs. integrated processes for syngas [a] production.

Scenarios	**DAC + SOEC for 2:1 H_2:CO**	**RWGS, H_2 from water electrolyzer and CO_2 from DAC**	**Bicarbonate electrolysis** [d]	**Carbonate electrolysis (best prior)** [e]	**Carbonate electrolysis (this work)** [f]
Air contactor (GJ) [b]	0.42	0.42	0.42	0.42	0.42
CO_2 regeneration (GJ) [c]	15.7	15.7	—	—	—
CO_2-to-CO EE (%)	60	100	—	—	—
Green H_2 EE (%)	65	65	65	65	65
pH downshifter	—	—	12.7	—	—
Syngas EE (%)	63	—	40	39	55
Electricity (GJ)	37.7	47.2	46.6	60.9	43.4
CO_2 separation (GJ)	1.7	1.7	0	0	0
Total energy (GJ)	**55**	**65**	**60**	**61**	**44**

a. Syngas: molar ratio of H_2: CO = 2:1

If $FE_{CO} < 33\%$, additional CO was supplied from DAC-SOEC process. When the SOEC is assumed, the EE to CO is set to 80%. The analysis does assume (as in column 1, DAC+SOEC), the need for CO_2 regeneration, circulation, and an air contactor. The resultant effective EE for CO is 25% in this case of "CO-infill", the same as for the CO contributed in column 1.

If $FE_{CO} > 33\%$, additional H_2 from water electrolyzer having EE for H_2 of 65%.

b. 99% of CO_2 from the air is converted into CO.

c. CO_2 regeneration from carbonate is powered by natural gas.

d. For bicarbonate electrolysis at 100 mA/cm^2, the FE_{CO} = 80%, and the cell voltage is 3.5 V. These results are based on the literature: *Energy & Environmental Science* 15.2 (2022): 705-713; *Energy & Environmental Science* 17.10 (2024): 3570-3579.

For pH downshifter energy consumption, the results are based on our experimental analysis as shown in **Supplementary Note 1**. The energy consumption value is similar to the literature: *Industrial & Engineering Chemistry Research* 61.34 (2022): 12668-12679.

e. From literature *ACS Energy Letters* 4.6 (2019): 1427-1431.

f. The experimental results for this scenario are based on the following values: 47% FE_{CO} with a cell voltage of 2.6 V at a current density of 100 mA/cm^2,

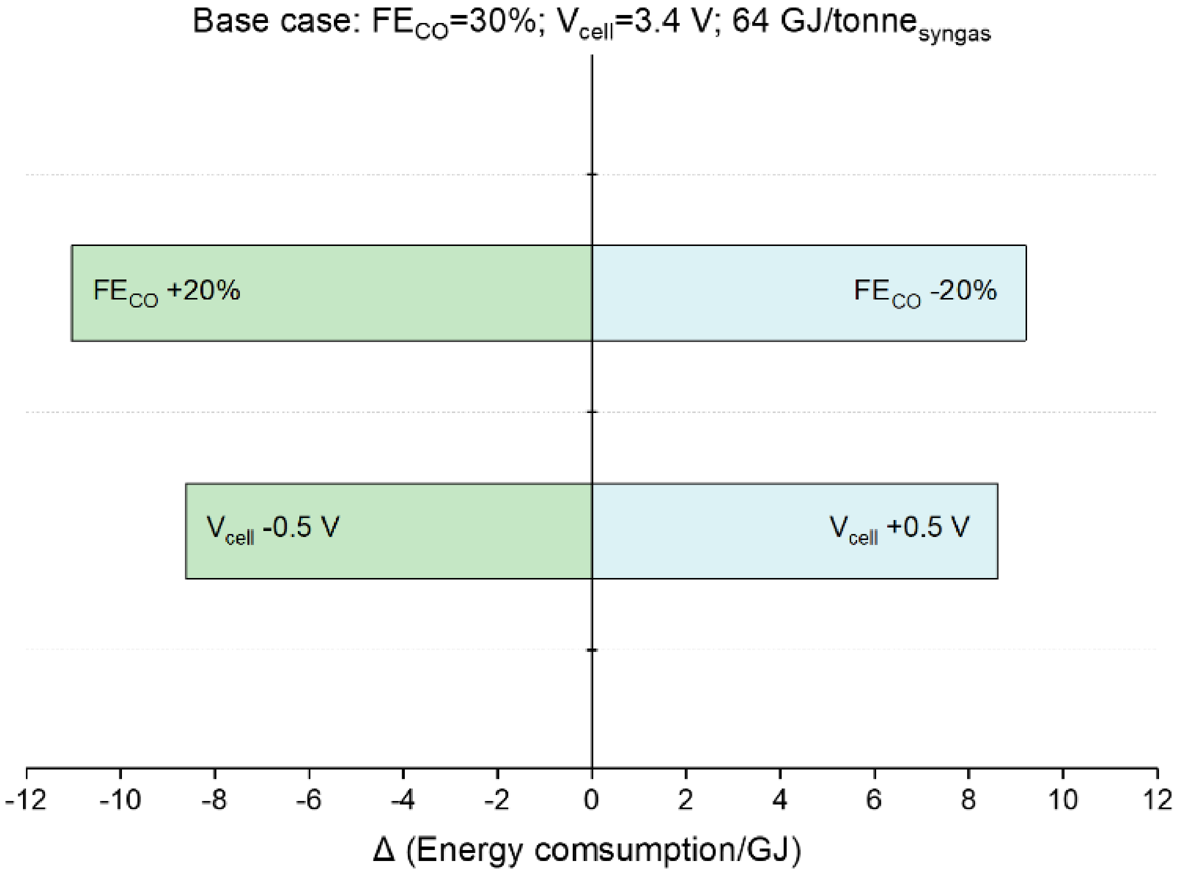

Supplementary Figure 68. Sensitivity analysis of cell voltage and FE_{CO} for carbonate to syngas. Energy consumption variation for FE_{CO} changes of ±20% and cell voltage shifts of ±0.5 V. The base case parameters were FE_{CO} = 30% and V_{cell} = 3.4 V, resulting in an energy consumption of 64 GJ/tonne of syngas.

Supplementary Note 13. Life cycle assessment

This study conducted a cradle-to-gate life cycle assessment (LCA) to estimate the greenhouse gas (GHG) emissions associated with syngas production via carbonate electrolysis, direct air capture with solid oxide electrolysis cells (DAC-SOEC), DAC with reverse water-gas shift (DAC-RWGS), and traditional methods such as steam reforming of natural gas and coal gasification. The functional unit for this assessment was set at 1 t of syngas. The system utilized three distinct electricity sources: the US mix (78% fossil energy), US 2030, and wind (**Supplementary Table 7**). The carbon intensity of US 2030 (162.78 g/kWh) is obtained from International Energy Agency (IEA) report.[44] The LCA data were sourced from the Greenhouse Gases, Regulated Emissions, and Energy Use in Technologies (GREET 2023) model developed by Argonne National Laboratory, IL, USA.[45] **Supplementary Figure 69** illustrates the system boundaries for each scenario. The process workflow for carbonate electrolysis begins with introducing air into a contactor to capture biogenic CO_2, which reacts with KOH to form K_2CO_3. The K_2CO_3 solution is then subjected to an electrochemical process, yielding KOH, CO and H_2. The KOH is recycled back for CO_2 capture. For DAC-SOEC and DAC-RWGS, CO_2 captured by DAC is transferred to SOEC and RWGS units, where it is converted into CO and H_2, subsequently producing syngas with additional hydrogen from water electrolysis. Detailed life cycle inventory (LCI) data are provided in **Supplementary Table 8**. The energy input is presented in **Supplementary Table 7**. The global warming potential (GWP) values for syngas produced from coal gasification and natural gas steam reforming are 2.54 t CO_2e/t syngas and 2.06 t CO_2e/t syngas, as obtained from Greet 2023. Additionally, the GHG emission factor for natural gas combustion is 56.1 kg CO_2e/GJ, based on the Intergovernmental Panel on Climate Change (IPCC) report.[46]

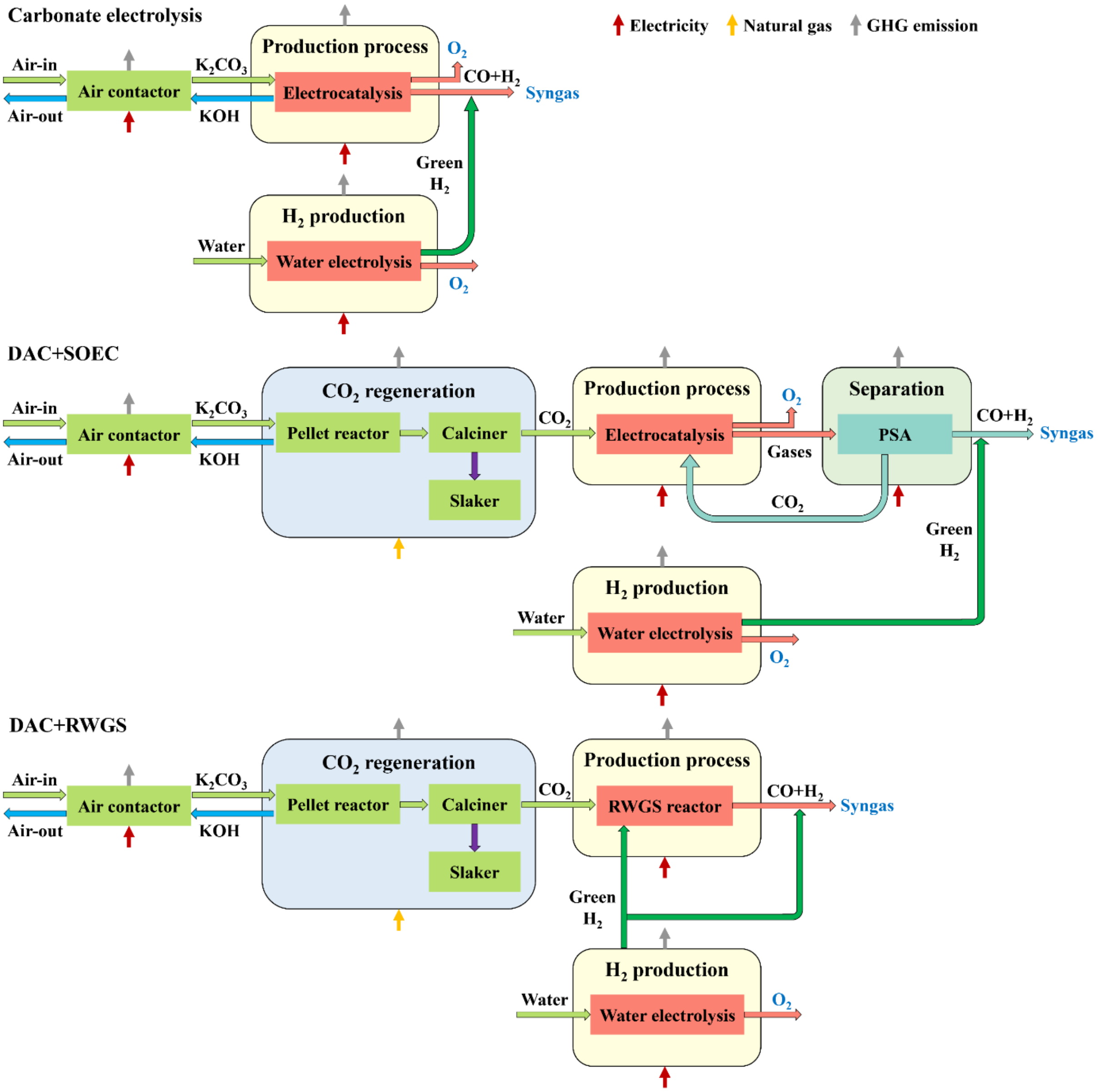

Supplementary Figure 69. System boundary of carbonate electrolysis, DAC+SOEC, and DAC+RWGS.

Supplementary Table 7. Electric generation mixes in 2023.[45]

Item	**US Mix**
Residual oil	0.26%
Natural gas	38.51%
Coal	20.60%
Nuclear power	18.88%
Biomass	0.27%
Hydroelectric	6.75%
Geothermal	0.38%
Wind	10.70%
Solar PV	3.28%
Others	0.37%

Supplementary Table 8. LCI data.

Item	**US mix**	**US 2030**[44]	**Wind**	**Oxygen (ASU) (kg)**	**Syngas from coal (kg)**	**Syngas from natural gas (kg)**
Total energy (kJ/GJ or kg)	1,939,568		1,088,820	432	21,557	16,114
Fossil fuels	1,501,180		34,855	338	0	0
Coal	631,297		13,248	134	20,308	0
Natural gas	859,147		10,254	200	0	16,114
Petroleum	10,735		11,352	4	0	0
Electricity	0		0	0	1,249	0
GHG values (g CO$_2$e/GJ or kg)	122,990	45,217	2,855	28.96	2,318	1,255

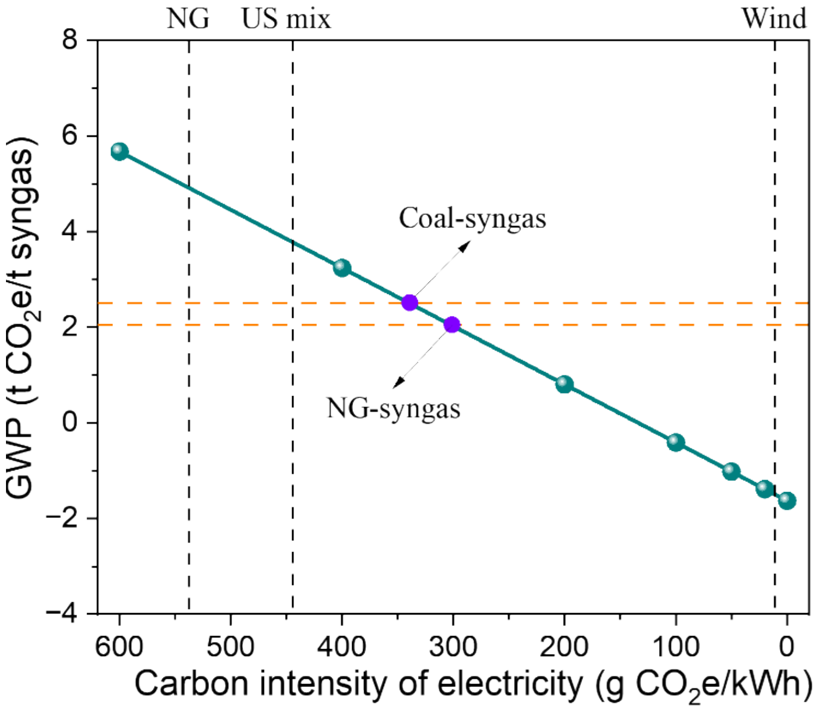

Supplementary Figure 70. GWP-CI relation on the GWP value of the RC system. The purple dot indicates the CI of the electricity, resulting in an RC's GWP value that matches that of coal-syngas and NG-syngas.

Supplementary Note 14. – Techno-economic analysis

In this study, we consider a medium-sized syngas plant with a daily production capacity of 1,000 t, resulting in an annual production capacity of 365,000 t. The techno-economic analysis (TEA) was conducted based on previously established models.[47,48] The assumptions for the syngas plants are detailed in **Supplementary Table 9**.

The TEA primarily comprises three components: total capital cost (TCC), operational costs, and byproduct income. The TCC includes capital expenditures for the direct air capture (DAC) system (air contactor and CO_2 regeneration), electrolyzer, reverse water-gas shift (RWGS) reactor, and pressure swing adsorption (PSA) unit. Operational costs encompass expenses related to electricity, water, and gas product separation. The byproduct generated in this process is oxygen.

The minimum selling price (MSP) per t of syngas was estimated by considering the annualized capital cost (ACC) and the annual operating expenditure (OpEx). The ACC was determined by calculating the capital recovery factor (CRF), as demonstrated by the following equations:

$$MSP = \frac{\text{ACC} + \text{OpEx}}{\text{annual plant capacity}} \quad (1)$$

$$ACC = CapEx \times CRF \quad (2)$$

$$CRF = \frac{i(1+i)^{\text{lifetime}}}{(1+i)^{\text{lifetime}} - 1} \tag{3}$$

A discount rate of 5% and a plant lifetime of 20 years are applied, resulting in a capital recovery factor (CRF) of 0.08.[49] To determine the cost per t of syngas, the TCC of the entire plant is multiplied by the CRF and then divided by the annual yield of syngas.

Supplementary Table 9. Techno-economic assumptions of syngas plants.

Parameters	Unit	Value
Assumptions		
Service life	Year	20
Annual capacity	t/year	365,000
Throughput	t/day	1,000
Discount rate[50]	%	5
Electrolyser cost[49]	US$/kW	550
SOEC Electrolyser cost[51,52]	US$/kW	1,250
DAC		
Air contactor reference capital cost	US$ M	212.20
CO_2 regeneration capital cost (rest of equipment)	US$ M	914.60
Reference CO_2 capacity	t/year	980,000
DAC scaling factor[53]		0.60
RWGS reactor		
RWGS reactor reference capital cost	US$ M	32
Reference capacity	t/h	43
RWGS reactor scaling factor[47]		0.70
Gas product separation[47]		
PSA operational cost	kWh/m^3	0.25
PSA reference capital cost	US$ M	1,989,043
PSA reference capacity	m^3/h	1,000
PSA capacity scaling factor		0.70

Total capital cost

Air contactor CO_2 regeneration

The modularity of the air contactor model enables the multiplication of the flow rate of the captured CO_2 stream by the number of air contactors required to capture the necessary amount of CO_2 for each pathway. The reference annual CO_2 capacity is 0.98 million tonnes (Mt), whereas the annual CO_2 capacity for this project is 0.57 Mt. The TCC for air contactors is estimated at US$124.20 M.

CO_2 regeneration

CO_2 regeneration system includes the pellet reactor, calciner slaker, air separation unit, CO_2 compressor, and other rest DAC equipment. The TCC for this system is estimated at US$663.20 million, with a scaling factor of 0.60.[53]

$$\mathrm{TCC}_{\mathrm{CO2\ reg}}(\mathrm{US\$M}) = 914.6 \times \left(\frac{0.57}{0.98}\right)^{0.6} = \mathrm{US\$663.20M} \tag{4}$$

Electrochemical system

The baseline parameters for the electrochemical process include a current density of 200 mA/cm^2, a total cell voltage of 2.9 V, and a faradaic efficiency (FE) of 47%. It is reported that the electrolyzer cost for the stack component is US$550/kW (400 mA/cm^2).[49] Solid Oxide Electrolyzer Cells (SOECs) have a higher CapEx than normal electrolyzers because they operate at much higher temperatures and require more complex materials and manufacturing processes. This complexity and the need for high-temperature-resistant materials like zirconia and nickel contribute to the increased CapEx.[54] The CapEx for a 5-MW system was about EU€2000/kW in 2020. Projections suggest that this cost will decrease to EU€1000/kW by 2030 and further to EU€530/kW by 2050.[52] These reductions are anticipated to result primarily from economies of scale. According to the report "Solid Oxide Electrolysis: A Technology Status Assessment", SOEC systems, including the balance of plant (BOP), could be installed for as low as US$917/kW.[51] Here, we use a CapEx of US$1250/kW for SOEC electrochemical system.

The power input in the electrochemical system is:

$$\text{Power input [kW]} = \text{Total energy input [GJ]} \times 277.778 \tag{5}$$

The reference cost for the electrolyzer is US$550/kW and US$1250/kW for SOEC, and the reference current density is 400 mA/cm^2. The total electrolyzer cost (TEC) is as follows:

TEC $_{\text{RC - electrolyzer}}$(US$)

$$= \text{Power input (kW)} \times \text{Cost}_{\text{Electrolyzer}}\ (\text{US\$}) \times \frac{\text{base current density}\left(\frac{\text{mA}}{\text{cm}^2}\right)}{\text{input current density}\left(\frac{\text{mA}}{\text{cm}^2}\right)} = 12944.55 \times$$

$$\frac{1000\left(\frac{\text{t}}{\text{day}}\right)}{24(\text{h})} \times 550\,\frac{\text{US\$}}{\text{kW}} \times \frac{400\left(\frac{\text{mA}}{\text{cm}^2}\right)}{200\left(\frac{\text{mA}}{\text{cm}^2}\right)} = \text{US\$}593287512$$

TEC $_{\text{RC prior - electrolyzer}}$(US$)

$$= \text{Power input (kW)} \times \text{Cost}_{\text{SOEC - electrolyzer}}\ (\text{US\$}) \times \frac{\text{base current density}\left(\frac{\text{mA}}{\text{cm}^2}\right)}{\text{input current density}\left(\frac{\text{mA}}{\text{cm}^2}\right)} = 20555.57$$

$$\times \frac{1000\left(\frac{\text{t}}{\text{day}}\right)}{24(\text{h})} \times 550\,\frac{\text{US\$}}{\text{kW}} \times \frac{400\left(\frac{\text{mA}}{\text{cm}^2}\right)}{200\left(\frac{\text{mA}}{\text{cm}^2}\right)} = \text{US\$}942130383$$

TEC $_{\text{SOEC - electrolyzer}}$(US$)

$$= \text{Power input (kW)} \times \text{Cost}_{\text{SOEC - electrolyzer}}\ (\text{US\$}) \times \frac{\text{base current density}\left(\frac{\text{mA}}{\text{cm}^2}\right)}{\text{input current density}\left(\frac{\text{mA}}{\text{cm}^2}\right)} = 10555.56$$

$$\times \frac{1000\left(\frac{\text{t}}{\text{day}}\right)}{24(\text{h})} \times 1250\,\frac{\text{US\$}}{\text{kW}} \times \frac{400\left(\frac{\text{mA}}{\text{cm}^2}\right)}{200\left(\frac{\text{mA}}{\text{cm}^2}\right)} = \text{US\$}1099537917$$

TEC $_{\text{RWGS - electrolyzer}}$(US$)

$$= \text{Power input (kW)} \times \text{Cost}_{\text{Electrolyzer}}\ (\text{US\$}) \times \frac{\text{base current density}\left(\frac{\text{mA}}{\text{cm}^2}\right)}{\text{input current density}\left(\frac{\text{mA}}{\text{cm}^2}\right)} = 10055.56$$

$$\times \frac{1000\left(\frac{\text{t}}{\text{day}}\right)}{24(\text{h})} \times 550\,\frac{\text{US\$}}{\text{kW}} \times \frac{400\left(\frac{\text{mA}}{\text{cm}^2}\right)}{200\left(\frac{\text{mA}}{\text{cm}^2}\right)} = \text{US\$}460879998$$

(6)

The balance of plant (BoP) cost is assumed to be 50% of the total electrolyzer cost, which is

$$\mathrm{BoP}_{\mathrm{Electrolyzer}}(\mathrm{US\$}) = \mathrm{TEC}_{\mathrm{Electrolyzer}}(\mathrm{US\$}) \times 0.5 \tag{7}$$

The total capital cost of the electrochemical plant is the sum of the total electrolyzer cost and the balance of the plant as follows:

$$TCC_{RC-Electrolyzer}(US\$) = TEC_{RC-Electrolyzer}(US\$) + BoP_{RC-Electrolyzer}(US\$) = US\$889931268$$

$$TCC_{RC\,prior-electrolyzer}(US\$) = TEC_{RC-Electrolyzer}(US\$) + BoP_{RC-Electrolyzer}(US\$) = US\$1413195575$$

$$TCC_{SOEC-electrolyzer}(US\$) = TEC_{SOEC-Electrolyzer}(US\$) + BoP_{SOEC-Electrolyzer}(US\$) = US\$1649306875$$

$$TCC_{RWGS-electrolyzer}(US\$) = TEC_{RWGS-electrolyzer}(US\$) + BoP_{RWGS-electrolyzer}(US\$) = US\$691319998$$

(8)

RWGS reactor

The DAC-RWGS system needs an RWGS reactor to process CO_2 and H_2. The reference capacity of RWGS is 43 t/h.[47] In our system, RWGS reactor need to process 1646 t/h (1571 t CO_2 and 75 t of H_2) the We calculate the TCC of plasma as follows:

$$\mathrm{TCC}_{\mathrm{CO2\,reg}}(\mathrm{US\$M}) = 32 \times \left(\frac{1646}{43}\right)^{0.7} = \mathrm{US\$423.35M} \tag{9}$$

PSA system

In DAC-SOEC system, a PSA system is required to separate CO_2 from mixed gases product (CO_2 and CO). We assume the single pass conversion efficiency is 30%, thus, about 3665.7 t of CO_2 needs to be separated from the mixture and recycled back to the SOEC. For the gas products separation equipment, the TCC is based on previous reference.[47] The CO_2 density is 1.98 kg/m^3.[55]

$$\text{Flow rate}\left(\frac{m^3}{\text{hour}}\right) = \frac{Output\ mass\left(\frac{kg}{\text{hour}}\right)}{Stand\ density\left(\frac{kg}{m^3}\right)} = 1851347 \tag{10}$$

$$TCC_{PSA}\,(US\$) = US\$1989043 \times \left(\frac{\text{flow rate}\left(\frac{m^3}{\text{hour}}\right)}{1000\left(\frac{m^3}{\text{hour}}\right)}\right)^{0.7} = US\$385376846 \tag{11}$$

Supplementary Table 10. Total capital cost of various syngas production systems.

TCC	Unit	DAC-SOEC	DAC-RWGS	Prior study	This study
Air contactor	US\$ M	124.20	124.20	124.20	124.20
CO_2 regeneration	US\$ M	663.21	663.21	–	–

PSA	US$ M	385.38	–	–	–
Electrolyser	US$ M	1649.31	691.32	1413.20	889.93
RWGS reactor	US$ M	–	423.35	–	–

Operating cost

Feedstocks cost

In our study, atmospheric air was utilized as feedstock. The commercial price of syngas in U.S. is obtained from previous study.[56]

Supplementary Table 11. Market price of feedstocks and products.

Items	Unit	Value
Feedstocks		
Water [48]	US$/t	5
Products		
Oxygen [57]	US$/t	60
Syngas in U.S. market [56]	US$/t	650

Electricity cost

The utilization of electricity in each process is based on previous references, experimental data, and simulations. The energy input for carbonate electrolysis is derived from our own experimental data. PSA is employed to separate CO_2 from the gas mixture, allowing for the reuse of CO_2 in the DAC-SOEC route. The electricity input for PSA is calculated as follows:

$$\text{PSA operating cost}\left(\frac{US\$}{\text{t } syngas}\right)=\frac{US\$0.25\times\ \text{flow rate}\left(\frac{m^3}{\text{hour}}\right)\times\text{electricity price}\left(\frac{US\$}{kWh}\right)}{\text{production rate}\left(\frac{t\ syngas}{h}\right)}=463\ kW$$

(12)

Electricity constitutes the primary operating cost for the entire process. Recent studies indicate a continuous decline in the cost of photovoltaic electricity, with projections suggesting that prices may soon fall to US$0.03/kWh.[58] Consequently, the base electricity price is conservatively set at US$0.045/kWh, consistent with previous studies.[56] The calculation of electricity costs is as follows:

$$\text{Cost of electricity}\left(\frac{US\$}{\text{t } syngas}\right)=\frac{\text{Power Consumed }(kW)\times\ \text{electricity price}\left(\frac{US\$}{kWh}\right)}{\text{Syngas production}\left(\frac{t\ syngas}{h}\right)} \tag{13}$$

Natural gas cost

About 13.9 GJ of natural gas is used in CO_2 regeneration process in DAC-SOEC and DAC-RWGS routes, and its cost is about US$5.02/GJ.[56]

Water cost

The production of 1 t of syngas from RC, DAC-SOEC, DAC-RWGS needs 2 t, 2 t, and 1 t of water. We calculate the necessary amount of water in electrolysis as follows:

$$\text{Water cost}\left(\frac{\text{t syngas}}{\text{h}}\right) = \text{US\$ } 5 \times \text{ water input}\left(\frac{\text{t syngas}}{\text{h}}\right) \qquad (14)$$

Maintenance

Maintenance encompasses routine upkeep, repairs, preventive maintenance, spare parts, utilities, and downtime costs. The annual maintenance costs for the plant are estimated to be 2.5% of the TCC_{all}.[47]

$$Maintenance\ (US\$) = 0.025 \times TCC_{all}(US\$) \qquad (15)$$

Byproducts

In the process, oxygen is generated at the anode side. The oxygen yield is 2 t, 2 t, and 1 t per t of syngas produced for the RC, DAC-SOEC, and DAC-RWGS systems, respectively.

$$Byproduct\ income(US\$) = 2 \times US\$\ 60 = US\$\ 120 \qquad (16)$$

Social cost of carbon

The social cost of carbon (SCC) represents an estimate of the economic damage associated with the emission of additional carbon dioxide into the atmosphere. This estimate encompasses a range of factors, including diminished agricultural productivity, adverse health effects, property damage due to increased flood risk, and alterations in energy system costs.[59] Policymakers utilize the SCC to assess the benefits of regulatory measures aimed at reducing carbon emissions. By assigning a monetary value to the damages caused by carbon emissions, the SCC facilitates informed decision-making regarding climate policies.[60] Recently, the United States Environmental Protection Agency (EPA) updated its SCC estimate to US$190/t of CO_2 [61]. The Global Warming Potential (GWP) values serve as the basis for the SCC, as the specific composition of greenhouse gases is not determined in the GWP calculation

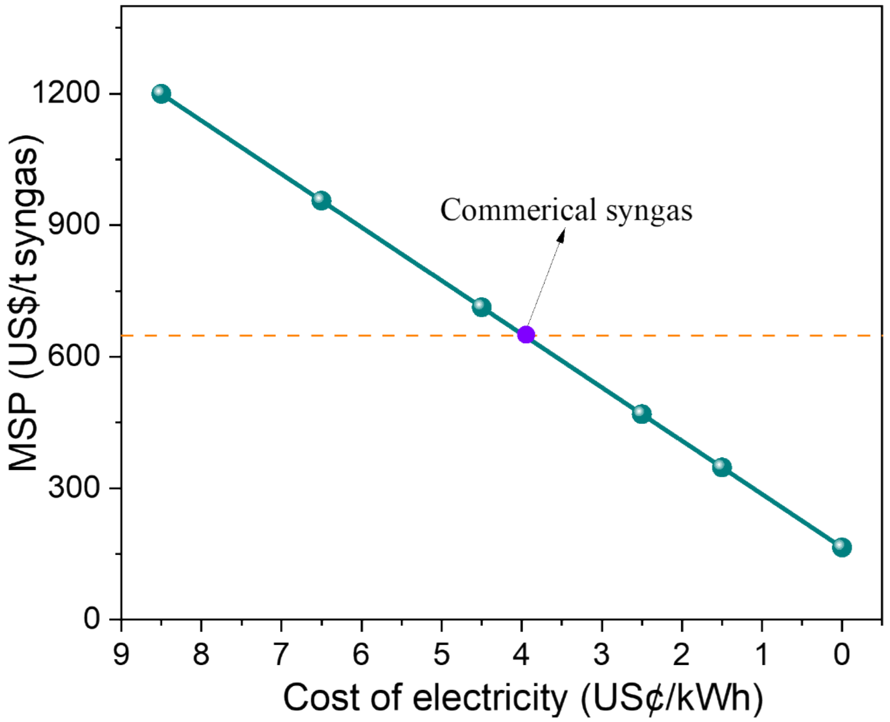

Supplementary Figure 71. Impact of electricity cost on the minimum selling price (MSP) of syngas from the RC system. The purple dot represents the electricity cost at which the syngas price from the RC system equals that of commercial syngas.

References

1 Keith, D. W., Holmes, G., Angelo, D. S. & Heidel, K. A process for capturing CO_2 from the atmosphere. *Joule* **2**, 1573-1594 (2018).

2 Almajed, H. M. *et al.* Closing the Loop: Unexamined Performance Trade-Offs of Integrating Direct Air Capture with (Bi)carbonate Electrolysis. *ACS Energy Lett* **9**, 2472-2483 (2024).

3 Sabatino, F., Gazzani, M., Gallucci, F. & van Sint Annaland, M. Modeling, optimization, and techno-economic analysis of bipolar membrane electrodialysis for direct air capture processes. *Industrial & Engineering Chemistry Research* **61**, 12668-12679 (2022).

4 Digdaya, I. A. *et al.* A direct coupled electrochemical system for capture and conversion of CO_2 from oceanwater. *Nature Communications* **11**, 4412 (2020).

5 Zhang, Z. *et al.* Porous metal electrodes enable efficient electrolysis of carbon capture solutions. *Energy & Environmental Science* **15**, 705-713 (2022).

6 Song, H. *et al.* Integrated carbon capture and CO production from bicarbonates through bipolar membrane electrolysis. *Energy & Environmental Science* **17**, 3570-3579 (2024).

7 Kas, R. *et al.* Modeling the local environment within porous electrode during electrochemical reduction of bicarbonate. *Industrial & Engineering Chemistry Research* **61**, 10461-10473 (2022).

8 Lees, E. W., Bui, J. C., Song, D., Weber, A. Z. & Berlinguette, C. P. Continuum model to define the chemistry and mass transfer in a bicarbonate electrolyzer. *ACS Energy Letters* **7**, 834-842 (2022).

9 Lee, G. *et al.* CO_2 electroreduction to multicarbon products from carbonate capture liquid. *Joule* **7**, 1277-1288 (2023).

10 Debergh, P. *et al.* The Economics of Electrochemical Syngas Production via Direct Air Capture. *ACS Energy Letters* **8**, 3398-3403 (2023).

11 Lee, S. H. *et al.* Design principle of Fe–N–C electrocatalysts: how to optimize multimodal porous structures? *J. Am. Chem. Soc.* **141**, 2035-2045 (2019).

12 Ren, S. *et al.* Catalyst aggregation matters for immobilized molecular CO_2RR electrocatalysts. *J. Am. Chem. Soc.* **145**, 4414-4420 (2023).

13 Masheder, D. & Williams, K. Raman spectro-electrochemistry. II. In situ raman spectroscopic studies of the electrochemical reduction of CO_2 at cobalt (II) phthalocyanine-impregnated PTFE-bonded carbon gas diffusion electrodes. *Journal of Raman spectroscopy* **18**, 391-398 (1987).

14 Tan, Y. C., Lee, K. B., Song, H. & Oh, J. Modulating local CO_2 concentration as a general strategy for enhancing C− C coupling in CO_2 electroreduction. *Joule* **4**, 1104-1120 (2020).

15 Brückner, S. *et al.* Design and Diagnosis of high-performance CO_2-to-CO electrolyzer cells. *Nature Chemical Engineering* **1**, 229-239 (2024).

16 Yarlagadda, V. *et al.* Boosting fuel cell performance with accessible carbon mesopores. *ACS Energy Letters* **3**, 618-621 (2018).

17 Chung, H. T. *et al.* Direct atomic-level insight into the active sites of a high-performance PGM-free ORR catalyst. *Science* **357**, 479-484 (2017).

18 Gabardo, C. M. *et al.* Continuous carbon dioxide electroreduction to concentrated multi-carbon products using a membrane electrode assembly. *Joule* **3**, 2777-2791 (2019).

19 Wen, G. *et al.* Continuous CO_2 electrolysis using a CO_2 exsolution-induced flow cell. *Nature Energy* **7**, 978-988 (2022).

20 Witkowski, A., Majkut, M. & Rulik, S. Analysis of pipeline transportation systems for carbon dioxide sequestration. *Archives of thermodynamics* **35**, 117--140 (2014).

21 Li, Y. C. *et al.* CO_2 electroreduction from carbonate electrolyte. *ACS Energy Letters* **4**, 1427-1431 (2019).

22 Xiao, Y. C. *et al.* Direct carbonate electrolysis into pure syngas. *EES Catalysis* **1**, 54-61 (2023).

23 Lees, E. W. *et al.* Electrodes designed for converting bicarbonate into CO. *ACS Energy Letters* **5**, 2165-2173 (2020).

24 Li, T. *et al.* Electrolytic conversion of bicarbonate into CO in a flow cell. *Joule* **3**, 1487-1497 (2019).

25 Lees, E. W. *et al.* Electrolytic methane production from reactive carbon solutions. *ACS Energy Letters* **7**, 1712-1718 (2022).

26 Li, T., Lees, E. W., Zhang, Z. & Berlinguette, C. P. Conversion of bicarbonate to formate in an electrochemical flow reactor. *ACS Energy Letters* **5**, 2624-2630 (2020).

27 Lee, J., Liu, H. & Li, W. Bicarbonate Electroreduction to Multicarbon Products Enabled by Cu/Ag Bilayer Electrodes and Tailored Microenviroments. *ChemSusChem* **15**, e202201329 (2022).

28 Liu, H., Chen, Y., Lee, J., Gu, S. & Li, W. Ammonia-mediated CO_2 capture and direct electroreduction to formate. *ACS Energy Letters* **7**, 4483-4489 (2022).

29 Gutierrez-Sanchez, O. *et al.* Electrochemical conversion of CO_2 from direct air capture solutions. *Energy & Fuels* **36**, 13115-13123 (2022).

30 Lee, G. *et al.* Electrochemical upgrade of CO_2 from amine capture solution. *Nature Energy* **6**, 46-53 (2021).

31 Kim, J. H. *et al.* The insensitive cation effect on a single atom Ni catalyst allows selective electrochemical conversion of captured CO_2 in universal media. *Energy & Environmental Science* **15**, 4301-4312 (2022).

32 Ren, S. *et al.* Molecular electrocatalysts can mediate fast, selective CO_2 reduction in a flow cell. *Science* **365**, 367-369 (2019).

33 Ma, S. *et al.* One-step electrosynthesis of ethylene and ethanol from CO_2 in an alkaline electrolyzer. *Journal of Power Sources* **301**, 219-228 (2016).

34 Endrődi, B. *et al.* High carbonate ion conductance of a robust PiperION membrane allows industrial current density and conversion in a zero-gap carbon dioxide electrolyzer cell. *Energy & Environmental Science* **13**, 4098-4105 (2020).

35 Ma, M. *et al.* Insights into the carbon balance for CO_2 electroreduction on Cu using gas diffusion electrode reactor designs. *Energy & Environmental Science* **13**, 977-985 (2020).

36 Xie, K. *et al.* Bipolar membrane electrolyzers enable high single-pass CO_2 electroreduction to multicarbon products. *Nature communications* **13**, 3609 (2022).

37 Wang, X. *et al.* Efficient CO and acrolein co-production via paired electrolysis. *Nature Sustainability*, 1-7 (2024).

38 Monteiro, M. C., Philips, M. F., Schouten, K. J. P. & Koper, M. T. Efficiency and selectivity of CO2 reduction to CO on gold gas diffusion electrodes in acidic media. *Nature communications* **12**, 4943 (2021).

39 Zhao, Y. *et al.* Conversion of CO_2 to multicarbon products in strong acid by controlling the catalyst microenvironment. *Nature Synthesis* **2**, 403-412 (2023).

40 Fan, M. *et al.* Single-site decorated copper enables energy-and carbon-efficient CO_2 methanation in acidic conditions. *Nature communications* **14**, 3314 (2023).

41 Almajed, H. M. *et al.* Closing the Loop: Unexamined Performance Trade-Offs of Integrating Direct Air Capture with (Bi) carbonate Electrolysis. *ACS Energy Letters* **9**, 2472-2483 (2024).

42 Sharifian, R., Wagterveld, R., Digdaya, I., Xiang, C.-x. & Vermaas, D. Electrochemical carbon dioxide capture to close the carbon cycle. *Energy & Environmental Science* **14**, 781-814 (2021).

43 Ozden, A. *et al.* Cascade CO_2 electroreduction enables efficient carbonate-free production of ethylene. *Joule* **5**, 706-719 (2021).

44 IEA. Carbon intensity of electricity generation in selected regions in the Sustainable Development Scenario, 2000-2040. (2020).

45 Laboratory, A. N. (2023).

46 Annex, I. Metrics and Methodology. *Climate Change* (2014).

47 Jouny, M., Luc, W. & Jiao, F. General Techno-Economic Analysis of CO_2 Electrolysis Systems. *Industrial & Engineering Chemistry Research* **57**, 2165-2177 (2018).

48 Jin, J. *et al.* Constrained C2 adsorbate orientation enables CO-to-acetate electroreduction. *Nature* **617**, 724-729 (2023).

49 Chen, F.-Y. *et al.* Electrochemical nitrate reduction to ammonia with cation shuttling in a solid electrolyte reactor. *Nature Catalysis* (2024).

50 YCHARTS. US Discount Rate. (2024).

51 Flis, G. & Wakim, G. Solid oxide electrolysis: a technology status assessment. *Clean Air Task Force* (2023).

52 Hauch, A. *et al.* Recent advances in solid oxide cell technology for electrolysis. *Science* **370**, eaba6118 (2020).

53 Weber, R. S., Askander, J. A. & Barclay, J. A. The scaling economics of small unit operations. *Journal of Advanced Manufacturing and Processing* **3**, e10074 (2021).

54 Energy, U. S. D. o. Hydrogen production: Electrolysis. Office of Energy Efficiency & Renewable Energy. (2023).

55 Li, X. *et al.* CO_2 point emission and geological storage capacity in China. *Energy Procedia* **1**, 2793-2800 (2009).

56 Almajed, H. M., Guerra, O. J., Smith, W. A., Hodge, B.-M. & Somoza-Tornos, A. Evaluating the techno-economic potential of defossilized air-to-syngas pathways. *Energy & Environmental Science* **16**, 6127-6146 (2023).

57 Atsonios, K., Panopoulos, K. D. & Kakaras, E. Investigation of technical and economic aspects for methanol production through CO_2 hydrogenation. *International Journal of Hydrogen Energy* **41**, 2202-2214 (2016).

58 Haegel, N. M. *et al.* Terawatt-scale photovoltaics: Trajectories and challenges. *Science* **356**, 141-143 (2017).

59 Ricke, K., Drouet, L., Caldeira, K. & Tavoni, M. Country-level social cost of carbon. *Nature Climate Change* **8**, 895-900 (2018).

60 Fleurbaey, M. *et al.* The Social Cost of Carbon: Valuing Inequality, Risk, and Population for Climate Policy. *The Monist* **102**, 84-109 (2019).

61 EPA. Report on the Social Cost of Greenhouse Gases: Estimates Incorporating Recent Scientific Advances. (2023).